

# **Combinatorial Optimisation for Arterial Image Segmentation**

Ehab Mohamed Mahmoud Essa

Submitted to Swansea University in fulfilment  
of the requirements for the Degree of Doctor of Philosophy



**Swansea University**  
**Prifysgol Abertawe**

Department of Computer Science  
Swansea University

2014



# Declaration

This work has not been previously accepted in substance for any degree and is not being concurrently submitted in candidature for any degree.

Signed ..... (candidate)

Date .....

# Statement 1

This thesis is the result of my own investigations, except where otherwise stated. Other sources are acknowledged by footnotes giving explicit references. A bibliography is appended.

Signed ..... (candidate)

Date .....

# Statement 2

I hereby give my consent for my thesis, if accepted, to be available for photocopying and for inter-library loan, and for the title and summary to be made available to outside organisations.

Signed ..... (candidate)

Date .....



# Abstract

Cardiovascular disease is one of the leading causes of the mortality in the western world. Many imaging modalities have been used to diagnose cardiovascular diseases. However, each has different forms of noise and artifacts that make the medical image analysis field important and challenging. This thesis is concerned with developing fully automatic segmentation methods for cross-sectional coronary arterial imaging in particular, intra-vascular ultrasound and optical coherence tomography, by incorporating prior and tracking information without any user intervention, to effectively overcome various image artifacts and occlusions.

Combinatorial optimisation methods are proposed to solve the segmentation problem in polynomial time. A node-weighted directed graph is constructed so that the vessel border delineation is considered as computing a minimum closed set. A set of complementary edge and texture features is extracted. Single and double interface segmentation methods are introduced. Novel optimisation of the boundary energy function is proposed based on a supervised classification method. Shape prior model is incorporated into the segmentation framework based on global and local information through the energy function design and graph construction.

A combination of cross-sectional segmentation and longitudinal tracking is proposed using the Kalman filter and the hidden Markov model. The border is parameterised using the radial basis functions. The Kalman filter is used to adapt the inter-frame constraints between every two consecutive frames to obtain coherent temporal segmentation. An HMM-based border tracking method is also proposed in which the emission probability is derived from both the classification-based cost function and the shape prior model. The optimal sequence of the hidden states is computed using the Viterbi algorithm.

Both qualitative and quantitative results on thousands of images show superior performance of the proposed methods compared to a number of state-of-the-art segmentation methods.



# Acknowledgements

I would like to express my special appreciation and thanks to my supervisor Dr. Xianghua Xie, for his priceless support, inspiration, and guidance during my research. This thesis would not have been possible without his encouragement and guidance. I would like to thank my second supervisor Dr. Igor Sazonov and also Prof. Perumal Nithiarasu for their support and useful feedback.

I am so grateful to the College of Engineering and the Department of Computer Science at the University of Swansea for the joint scholarship which I received, Zienkiewicz and Departmental scholarships, that made it possible for me to study here.

I would like to express my gratitude to Dr. Dave Smith and Dr. James Cotton for providing the clinical data and their valuable help in preparing the manual labelling.

I am also thankful to all of my colleagues in the lab: Dr. Huaizhong Zhang, Jingjing Deng, Jonathan Lee Jones, Robert Palmer, Dr. Hui Fang, Dr. Ben Daubney, Dr. Feng Zhao, Ren Liu, and Dr. Cyril Charron.

A special thanks to my family. Words cannot express how grateful I am to my parents, and my two brothers, Ashraf and Ahmed, who gave me the incentive to strive towards my goal. I am heartily thankful to my friend, Islam Reda, who has helped me to sort out my issues in my home country.

While I was completing my doctoral research, I lost my mother. It was with a heavy heart that I continued. I would like to dedicate my thesis to the memory of my beloved mother.

# Table of Contents

|   |             |
|---|-------------|
| <b>List of Tables</b>                                     | <b>xiii</b> |
| <b>List of Figures</b>                                    | <b>xv</b>   |
| <b>1 Introduction</b>                                     | <b>1</b>    |
| 1.1 Motivation . . . . .                                  | 2           |
| 1.2 Overview . . . . .                                    | 5           |
| 1.2.1 Bottom-up segmentation . . . . .                    | 6           |
| 1.2.2 Segmentation with prior information . . . . .       | 6           |
| 1.2.3 Spatio-temporal tracking and segmentation . . . . . | 7           |
| 1.3 Contribution . . . . .                                | 7           |
| 1.4 Thesis outline . . . . .                              | 8           |
| <b>2 Background</b>                                       | <b>11</b>   |
| 2.1 Introduction . . . . .                                | 11          |
| 2.2 Coronary arterial imaging . . . . .                   | 12          |
| 2.2.1 Invasive Imaging . . . . .                          | 12          |
| 2.2.2 Non-Invasive Imaging . . . . .                      | 16          |
| 2.3 Coronary arterial imaging analysis . . . . .          | 19          |
| 2.3.1 Vessel Segmentation . . . . .                       | 19          |
| 2.3.2 Tissue Characterisation . . . . .                   | 30          |
| 2.3.3 3D Vessel Reconstruction . . . . .                  | 31          |
| 2.3.4 Image Registration . . . . .                        | 33          |
| 2.4 Summary . . . . .                                     | 38          |
| <b>3 Graph Cut Segmentation: A Bottom-Up Approach</b>     | <b>39</b>   |

|          |  |           |
|----------|--|-----------|
| 3.1      | Introduction . . . . .                             | 39        |
| 3.2      | Preprocessing . . . . .                            | 41        |
| 3.3      | Feature Extraction . . . . .                       | 42        |
| 3.3.1    | Steerable filter . . . . .                         | 42        |
| 3.3.2    | Log Gabor filter . . . . .                         | 42        |
| 3.3.3    | Local phase . . . . .                              | 43        |
| 3.3.4    | Circulation density features . . . . .             | 44        |
| 3.4      | Single and Double Interface Segmentation . . . . . | 46        |
| 3.4.1    | Graph construction . . . . .                       | 46        |
| 3.4.2    | Cost function . . . . .                            | 48        |
| 3.4.3    | Compute the minimum closed set . . . . .           | 50        |
| 3.4.4    | Post-processing . . . . .                          | 50        |
| 3.5      | Results: IVUS . . . . .                            | 51        |
| 3.6      | Results: OCT . . . . .                             | 56        |
| 3.7      | Summary . . . . .                                  | 60        |
| <b>4</b> | <b>Segmentation with Shape Prior</b>               | <b>63</b> |
| 4.1      | Introduction . . . . .                             | 63        |
| 4.2      | Tissue and Artifact Classification . . . . .       | 66        |
| 4.3      | Cost Function Optimisation . . . . .               | 68        |
| 4.3.1    | IVUS cost function . . . . .                       | 69        |
| 4.3.2    | OCT cost function . . . . .                        | 70        |
| 4.4      | Shape Prior Model . . . . .                        | 70        |
| 4.4.1    | Graph construction: shape prior . . . . .          | 71        |
| 4.4.2    | Cost function: shape prior . . . . .               | 73        |
| 4.5      | Graph Cut . . . . .                                | 74        |
| 4.6      | Experimental Results . . . . .                     | 75        |
| 4.6.1    | IVUS segmentation . . . . .                        | 76        |
| 4.6.2    | OCT segmentation . . . . .                         | 81        |
| 4.7      | Summary . . . . .                                  | 82        |
| <b>5</b> | <b>Longitudinal Tracking and Segmentation</b>      | <b>83</b> |
| 5.1      | Introduction . . . . .                             | 83        |
| 5.2      | Border Parameterisation . . . . .                  | 86        |

|          |  |            |
|----------|--|------------|
| 5.3      | Spatio-Temporal Segmentation Using the Kalman filter . . . . . | 87         |
| 5.3.1    | Kalman filter . . . . .  | 87         |
| 5.3.2    | Temporal graph construction . . . . .                          | 88         |
| 5.3.3    | Cost function and graph cut . . . . .                          | 89         |
| 5.3.4    | Experimental results . . . . .                                 | 90         |
| 5.4      | Tracking Through HMM Modelling . . . . .                       | 91         |
| 5.4.1    | Transition probability . . . . .                               | 96         |
| 5.4.2    | Emission probability . . . . .                                 | 97         |
| 5.4.3    | Cost function . . . . .  | 98         |
| 5.4.4    | Viterbi algorithm . . . . .                                    | 99         |
| 5.4.5    | Experimental results . . . . .                                 | 100        |
| 5.5      | Summary . . . . .  | 102        |
| <b>6</b> | <b>Conclusions and Future Work</b>                             | <b>109</b> |
| 6.1      | Conclusions . . . . .  | 109        |
| 6.2      | Contributions . . . . .  | 112        |
| 6.3      | Future Work . . . . .  | 113        |
| <b>A</b> | <b>List Of Publications</b>                                    | <b>117</b> |
|          | <b>Bibliography</b>  | <b>119</b> |



# List of Tables

|     |   |    |
|-----|---|----|
| 3.1 | Comparison between <i>s-t</i> cut, single-interface and double-interface segmentation results. AD: area difference in percentage; AMD: absolute mean difference in pixel compared to ground-truth. . . . .                            | 53 |
| 3.2 | Quantitative results with 2283 images for star graph cut [1] and the proposed method. AMD: Absolute Mean Difference(pixel); HD: Hausdorff Distance(pixel); AO: Area Overlap(%); Sens.: Sensitivity(%); Spec.: Specificity(%). . . . . | 56 |
| 3.3 | Quantitative results with 226 images for the methods in [2], [3] and [4]. AMD: absolute mean difference(pixel); HD: Hausdorff distance(pixel); AO: area overlap(%); Sens.: sensitivity(%); Spec.: specificity(%). . . . .             | 59 |
| 4.1 | IVUS column-wise tissue classification. . . . .   | 76 |
| 4.2 | IVUS quantitative comparison. AMD: absolute mean difference(pixel); HD: Hausdorff distance(pixel); AO: area overlap(%); Sens.: sensitivity(%); Spec.: specificity(%). . . . .   | 79 |
| 4.3 | OCT column-wise tissue classification. . . . .  | 81 |
| 4.4 | OCT quantitative comparison. AMD: absolute mean difference(pixel); HD: Hausdorff distance(pixel); AO: area overlap(%); Sens.: sensitivity(%); Spec.: specificity(%). . . . .  | 82 |
| 5.1 | IVUS quantitative results of the proposed spatio-temporal method. AMD: Absolute Mean Difference(pixel); HD: Hausdorff Distance(pixel); AO: Area Overlap(%); Sens.: Sensitivity(%); Spec.: Specificity(%). . . . .                     | 91 |
| 5.2 | OCT quantitative results of the proposed spatio-temporal method. AMD: Absolute Mean Difference(pixel); HD: Hausdorff Distance(pixel); AO: Area Overlap(%); Sens.: Sensitivity(%); Spec.: Specificity(%). . . . .                      | 91 |

|     |   |     |
|-----|---|-----|
| 5.3 | OCT quantitative comparison. HD: Hausdorff distance (pixel). . . . .  | 100 |
| 5.4 | OCT quantitative comparison. AMD: absolute mean difference(pixel); HD: Hausdorff distance(pixel); AO: area overlap(%); Sens.: sensitivity(%); Spec.: specificity(%). . . . .  | 101 |
| 5.5 | OCT quantitative comparison. AMD: absolute mean difference(pixel); HD: Hausdorff distance(pixel); AO: area overlap(%); Sens.: sensitivity(%); Spec.: specificity(%). . . . .  | 101 |
| 5.6 | IVUS quantitative comparison. AMD: absolute mean difference(pixel); HD: Hausdorff distance(pixel); AO: area overlap(%); Sens.: sensitivity(%); Spec.: specificity(%). . . . . | 107 |

# List of Figures

|     |  |    |
|-----|--|----|
| 1.1 | Coronary arteries (adapted from [5]): right and left coronary arteries are the main supply vessels for the heart that come from the aortic sinus, each one of them is split into many branches. . . . .  | 2  |
| 1.2 | Coronary artery disease (adapted from [6]): the left image is a healthy normal artery. The artery consists of three layers; intima, media, and adventitia. The right image is a disease artery, lipid and other fatty materials deposited inside the artery. | 3  |
| 1.3 | IVUS and OCT: IVUS acquired by 40MHz transducer Boston Scientific ultrasound machine and OCT acquired by C7-XR LightLab Imaging system. . . . .  | 4  |
| 2.1 | Example IVUS and OCT imaging artifacts: (a) Calcium shadowing. (b) Stent artifact. (c) Non-uniform rotational distortion. (d) Residual Blood. (e) Fold-over artifact. (f) Saturation artifact. . . . .   | 15 |
| 3.1 | (a) An original IVUS image. (b) Polar transformed image. (c) After removing the catheter region (green curve shows the ground-truth of media-adventitia border). . .   | 40 |
| 3.2 | Graph construction. (a) intra-column and inter-column arcs when $\Delta_{p,q} = 1$ . (b) inter-interface constraints when $\delta_{min} = 1$ and $\delta_{max} = 3$ . . . . .  | 47 |
| 3.3 | The minimum closed set graph highlighted by red colour for, (a) the auxiliary interface, and (b) the media-adventitia border. (c) The media-adventitia border after the RBF smoothness. . . . .  | 51 |
| 3.4 | The effect of $\Delta_{p,q}$ constraints on single interface segmentation. These hard constraints globally set to 10, 5, and 1 pixel distance shown in a, b and c rows respectively. . . . .   | 52 |
| 3.5 | (a): initialisation for s-t cut, and its result shown in (b); (c): result by single interface segmentation; (d): proposed double-interface method. . . . .   | 53 |

|      |  |    |
|------|--|----|
| 3.6  | Comparison between ground-truth (green) and segmentation results (red): (a) $s-t$ graph cut result. (b) Single-interface result. (c) Double-interface result. . . . .  | 54 |
| 3.7  | (a) Ground-truth. (b) Single-interface. (c) Double-interface. . . . .  | 55 |
| 3.8  | Comparison with star graph cut. (a) Original image. (b) Ground-truth. (c) Star graph cut. (d) Proposed Method. . . . .   | 57 |
| 3.9  | Cases with the inferior performance of the proposed method. (a) Original image. (b) Ground-truth. (c) Star graph cut. (d) Proposed method. . . . .   | 59 |
| 3.10 | Results of the traditional methods in OCT. Column (a): Original image, Column (b): Ground-truth, Column (c): Improved Chan-Vese, Column (d): DRLSE, Column (e): VFC and Column (f): Proposed . . . . .   | 61 |
| 4.1  | Example IVUS and OCT images. First row: original images. Second row: polar transformed images. Last row: segmented media-adventitia border in IVUS and lumen border in OCT using the proposed method (red); the groundtruth is shown in green. The bottom of each segmented image visualises our column-wise tissue and artifact classification results. . . . .   | 65 |
| 4.2  | Haar-like Features. . . . .  | 68 |
| 4.3  | Example graph construction. (a) inter-columns arcs connecting two neighbouring columns and, where $\underline{\Delta}_{p,q} = -2$ and $\bar{\Delta}_{p,q} = 3$ in this example, shown as brown arcs. (b) smoothness arcs, in orange, for the same columns when $f'_{p,q}(0) = 0$ . . . . .   | 72 |
| 4.4  | Comparison between ground-truth (green) and segmentation results (red): (a) Original image; (b) $s - t$ cut [7] (foreground: yellow, background: blue); (c) Optimal surface [8] with 1st order GD; (d) Optimal surface [8] with 2nd order GD; (e) Proposed method: bottom of each image also visualises the RF classification result: calcified plaque (blue), fibrotic plaque (dark green), stent (dark red), guide-wire shadowing (cyan), and soft plaque/normal tissue (light green). . . . . | 75 |
| 4.5  | Comparison between ground-truth (green) and segmentation results (red): (a) Original image; (b) Optimal surface [8] with 1st order DoG; (c) Optimal surface [8] with local phase asymmetry; (d) Proposed method: bottom of each image also visualises the RF classification result: stent (dark red), guide-wire shadowing (cyan), and plaque/normal tissue (yellow). . . . .  | 76 |

|     |   |    |
|-----|---|----|
| 4.6 | Comparison between ground-truth (green) and segmentation results (red): (a) original image. (b) $s-t$ cut (foreground user strokes: yellow, background user strokes: blue). (c) optimal surface [8] with first order GD. (d) Texture-RBF method. (e) star graph cut (foreground user points: yellow, background user points: blue). (f) proposed method. . . . .  | 78 |
| 4.7 | Comparison between ground-truth (green) and segmentation results (red): (a) original image. (b) $s-t$ cut (foreground user strokes: yellow, background user strokes: blue). (c) optimal surface [8] with first order GD. (d) Texture-RBF method. (e) star graph cut (foreground user points: yellow, background user points: blue). (f) proposed method. . . . .  | 79 |
| 4.8 | Comparison between ground-truth (green) and segmentation results (red): (a) original image. (b) optimal surface [8] with first order GD. (c) star graph cut (star point: yellow). (d) proposed method. . . . .  | 80 |
| 5.1 | Example temporal graph construction between two frames $k-1$ and $k$ for the corresponding columns $p$ and $q$ . (a) inter-frame arcs (brown) for the initial segmentation, where $\Delta_{p_{k-1},p_k} = 1$ , and $\Delta_{q_{k-1},q_k} = 2$ . (b) inter-frame arcs (brown) adapted by the Kalman predicted border, assuming that $\bar{\Delta}_{p_{k-1},p_k} = 1$ , $\underline{\Delta}_{p_{k-1},p_k} = -1$ , and $\bar{\Delta}_{q_{k-1},q_k} = 2$ , $\underline{\Delta}_{q_{k-1},q_k} = -1$ . (b) smoothness arcs (orange) for the same columns when $f'_{t_{p_{k-1},p_k}}(0) = 0$ and $f'_{t_{q_{k-1},q_k}}(0) = 1$ . . . . . | 89 |
| 5.2 | Longitudinal view for five different pullbacks, the proposed spatio-temporal (red), the classification-based method (yellow) and groundtruth (green). . . . .   | 92 |
| 5.3 | Longitudinal view for three different pullbacks, the proposed spatio-temporal (red), the classification-based method (yellow) and groundtruth (green). . . . .  | 93 |
| 5.4 | Longitudinal view for five different OCT pullbacks, the proposed spatio-temporal (red), the classification-based method (yellow) and groundtruth (green). . . . .   | 94 |
| 5.5 | An example of border segmentation $S_t$ based on the border $S_{t-1}$ obtained in the previous frame using the proposed HMM Model. The border is divided into $M$ points and at each point a normal line is drawn with length $K$ . The final border is interpolated using RBF. . . . .   | 95 |
| 5.6 | HMM construction. The state-emission is illustrated in the upper part, whilst the arc-emission in the lower part. The arcs between the states are carrying the transition probabilities. . . . .  | 96 |

|      |   |     |
|------|---|-----|
| 5.7  | Longitudinal view for four different OCT pullbacks, the proposed state-emission HMM (red), the classification-based method (yellow) and groundtruth (green). . . .  | 103 |
| 5.8  | Longitudinal view for four different OCT pullbacks, the proposed arc-emission HMM (red), the classification-based method (yellow) and groundtruth (green). . . .    | 104 |
| 5.9  | Longitudinal view for four different IVUS pullbacks, the proposed state-emission HMM (red), the classification-based method (yellow) and groundtruth (green). . . . | 105 |
| 5.10 | Longitudinal view for four different IVUS pullbacks, the proposed arc-emission HMM (red), the classification-based method (yellow) and groundtruth (green). . . .   | 106 |
| 6.1  | Preliminary results using circulation density features. (a) Original image. (b) Star graph cut. (c) Proposed method. . . . .  | 115 |

# Chapter 1

## Introduction

### Contents

---

|     |                          |   |
|-----|--------------------------|---|
| 1.1 | Motivation . . . . .     | 2 |
| 1.2 | Overview . . . . .       | 5 |
| 1.3 | Contribution . . . . .   | 7 |
| 1.4 | Thesis outline . . . . . | 8 |

---

Image processing is a popular topic across many disciplines such as computer vision, pattern recognition, and medical imaging, where the understanding and analysis of image components is necessary. Medical image analysis has emerged as a result of the continuous development of medical image modalities for the diagnosis, prognosis and treatment of human diseases. One of these diseases is cardiovascular disease (CVD), which is one of the main causes of mortality nowadays in the western world [9, 10, 11]; cardiologists can use many image modalities in the diagnosis or during the treatment based on different techniques such as X-ray, magnetic resonance, and ultrasound. However, these modalities usually suffer from different degrees of noise, and image artifacts. Hence, medical image analysis has a vital role in enhancing the image quality [12, 13], image segmentation [14, 13, 15], image registration [16, 17], and image reconstruction [18, 19]. In this thesis, we investigate and develop automatic segmentation methods for cross-sectional coronary arterial imaging.

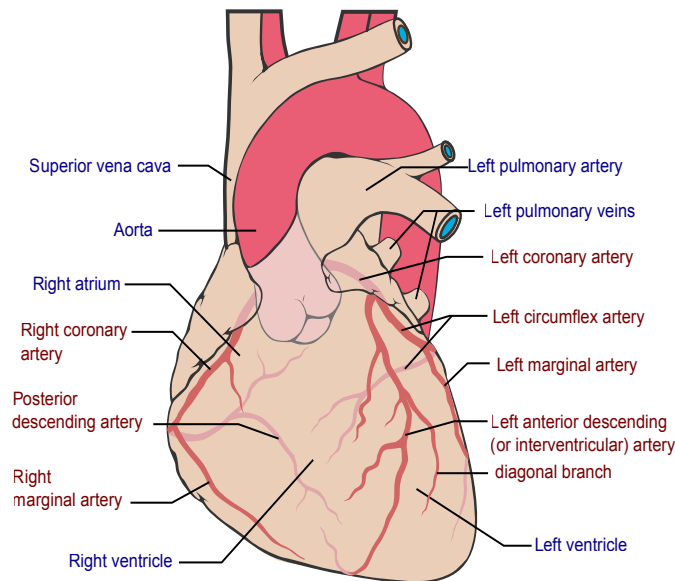


Figure 1.1: Coronary arteries (adapted from [5]): right and left coronary arteries are the main supply vessels for the heart that come from the aortic sinus, each one of them is split into many branches.

## 1.1 Motivation

The heart is the muscle that pumps the blood around the human body through the blood vessels. The heart remains healthy and sustainable by a set of vessels that regularly supply the muscle with oxygen and nutrients. These vessels are called coronary arteries. There are two major arteries that come from the ascending part of the aorta (see Figure 1.1): the right coronary artery and the left coronary artery. The right coronary artery [20] supplies blood to the right atrium and the right ventricle, a small area of left atrium and left ventricle, and the atrioventricular septum. It has two branches: the posterior descending artery and the right marginal artery. The left coronary artery supplies most of the left atrium and the left ventricle, and the ventricular septum. It also splits into two branches: the left anterior descending and the left circumflex.

A normal coronary artery consists of three regions: the lumen where the blood flows, the vessel that includes the intima and media layers, and the adventitia around the vessel wall. The diameter of each layer varies depending on the vessel type [21]. The intima is the most inner layer of the vessel; it consists of endothelial cells that prevent blood coagulation followed by elastic tissue. The internal elastic lamina separates the intima from the media layer. The

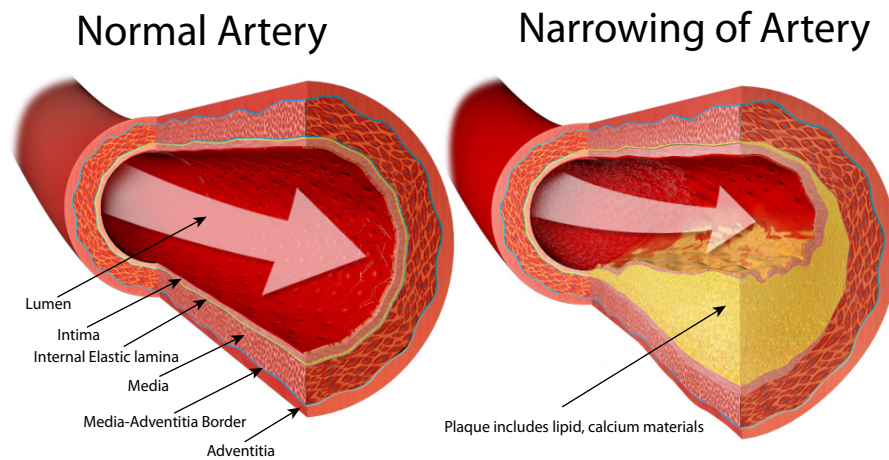


Figure 1.2: Coronary artery disease (adapted from [6]): the left image is a healthy normal artery. The artery consists of three layers; intima, media, and adventitia. The right image is a disease artery, lipid and other fatty materials deposited inside the artery.

media layer is usually a thick layer of smooth muscle cells intermixed with elastic fibres and it has a thinner layer that separates it from the adventitia called external elastic lamina (media-adventitia border). The adventitia is a collagen connective tissue located in the outermost layer of the vessel.

One of the main causes of CVD is coronary artery disease, also known as atherosclerosis, which is an inflammatory disorder that involves the deposition of cholesterol and other fatty substances within the arterial wall. The condition can lead to progressive narrowing of coronary arteries as shown in the right side of Figure 1.2 leading to clinical angina, or sudden blockage of the coronary arteries following atherosclerotic plaque rupture and thrombus formation leading to acute myocardial infarction.

Cardiac imaging can be classified into two categories: invasive and non-invasive imaging. Invasive imaging is catheterisation based where a catheter tube is inserted through the coronary artery by using a thin flexible guided wire, this imaging such as X-ray angiography, Intra-Vascular Ultrasound (IVUS), and Optical Coherence Tomography (OCT). X-ray angiography is the standard modality that shows the tree structure of the vessels, in which the stenosis location can be located. However, it does not give accurate information regarding surface pathologies within the arteries, such as plaque erosion, rupture and clot formation. IVUS and OCT

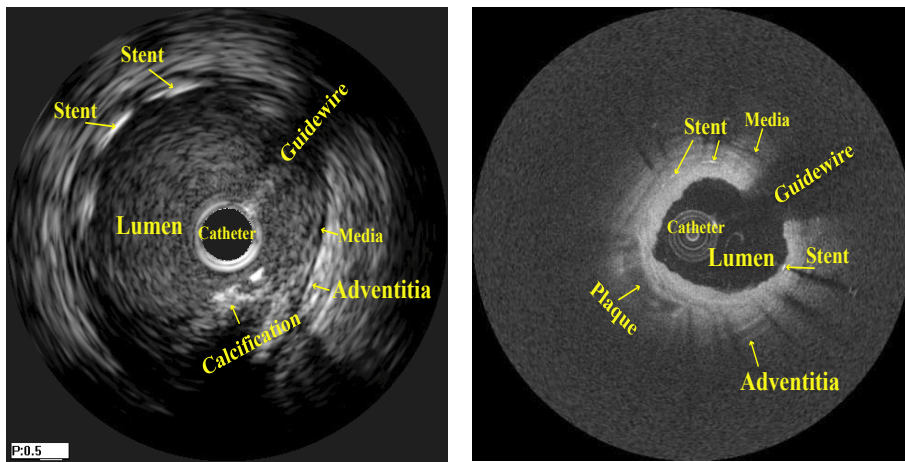


Figure 1.3: IVUS and OCT: IVUS acquired by 40MHz transducer Boston Scientific ultrasound machine and OCT acquired by C7-XR LightLab Imaging system.

produce two-dimensional cross-sectional images of the arteries where the catheter has a probe that measures the back-scattered signal from the surrounding vessel structure after sending sound waves in IVUS or light in OCT. These modalities provide a very detailed visualisation of lumen, stent strut location, and plaque morphology as shown in Figure 1.3.

Non-Invasive imaging can also produce good visualisation details of the stenosis location and plaque types for diagnostic purpose. Computed Tomography angiography (CTA) and Magnetic Resonance angiography (MRA) are the common imaging models. However the advantage of invasive imaging is the ability to acquire images during the treatment procedures.

There are two types of borders of clinical interest: the lumen-intima border that corresponds to the inner coronary arterial wall and the media-adventitia border that represents the outer coronary arterial wall located between the media and adventitia. Hence, image segmentation is the process of delineating the inner and/or the outer vessel wall, which is important for clinicians in order to assess the stenosis size and plaque morphology, and can also be later used to reconstruct the 3D vessel and fuse IVUS/OCT with other image modalities. IVUS Segmentation is still a challenge despite the improvement in the imaging quality over the past decades. The IVUS imaging has many artifacts that come from the mechanism of obtaining the image or the nature of ultrasound. These artifacts could interfere with the border of interest, shield subjacent structure of the vessel or distort its appearance. The most common artifacts are guide-wire, catheter ring-down artifacts, stents and calcification shadowing. OCT has a

higher resolution than IVUS, but it still has some image artifacts similar to the IVUS such as guide-wire artifact and residual blood that make the segmentation problem non-trivial.

Manually segmenting of IVUS and OCT is a time-consuming, tedious process, particularly each pullback may contain thousands of images and can suffer from high inter- and intra-operator variability. Semi-automatic segmentation methods combine user interaction with the automated process, where typically the user has to identify the region of interest [14] or the initialisation of the contour [22] or place some seed points on the object boundary [23, 24, 25]. However, these methods assume that the user has enough experience with the arterial wall location but this can be tricky for medical images like IVUS and is still time-consuming. Many automatic segmentation methods try to solve the segmentation problem by using visual cues such as edge [8], texture [26, 27], or statistical information [28]. However, together with prior and temporal knowledge, the delineation of the boundaries will be significantly meaningful.

The main objective of this work is to propose fully automatic segmentation methods to delineate the arterial wall in IVUS and OCT. Graph cut based methods that effectively solve the segmentation problem in polynomial time are proposed. Novel optimisation of the energy function based on a supervised classification method is presented to overcome various image artifacts. Shape prior model is proposed and incorporated into the segmentation framework to tackle irregular shape structures without the need of any user intervention. Temporal information is integrated to achieve consistent segmentation over consecutive frames through the novel adaption of well-known methods, i.e., the Kalman filter and the hidden Markov model (HMM). The proposed framework is able to reliably highlight the media-adventitia border in IVUS and lumen-intima border in OCT.

## **1.2 Overview**

Energy minimisation is a popular approach to segment the medical imaging, where the segmentation problem is defined as assigning one of the labels to each pixel in the image by minimising a combination of energy functions. The energy function, also known as cost function, could be defined based on the boundary, region and/or shape of the target object.

Graph cut, among many other energy minimisation methods, is a combinatorial optimisation technique that can be used to find the global minimisation of the energy function; it has been successfully used in many applications in computer vision and medical image analysis [29, 7].

Graph cut is a discrete optimisation in which the image is represented by a graph where each node corresponds to one pixel. The relationship between these nodes is defined by weighted arcs. The  $s$ - $t$  algorithms are commonly used to solve the segmentation problem in polynomial time. A notable variation to conventional graph cut is the optimal surface segmentation [8], which converts the segmentation problem into computing the minimum closed set graph without the need of any user intervention. In this work, the optimal surface graph cut method is used as the basis for our approaches to image segmentation.

### 1.2.1 Bottom-up segmentation

Bottom-up segmentation is a data-driven method that segments the image based on extracting some low-level features. Existing bottom-up segmentation methods for IVUS and OCT include fuzzy clustering [26], wavelet analysis combined with a thresholding method [27], Markov random field [30], and snake model [31].

The first part of the thesis is concerned with developing low-level bottom-up segmentation methods for IVUS and OCT. A combination of complementary texture features is used, instead of image intensity, to form the the cost functions. A novel image feature derived from global interactions of gradient vectors over the whole image domain is proposed. A diffusion scheme is also used to refine image feature and improve segmentation. A double-interface graph cut segmentation is proposed for IVUS, where an auxiliary interface is simultaneously segmented with the media-adventitia border to prevent undesirable image features from interfering with the segmentation of the border of interest in IVUS. A comparative study with experimental results on IVUS and OCT images is presented.

### 1.2.2 Segmentation with prior information

High-level information is usually combined with a bottom-up segmentation for better segmentation result. This high-level information may include shape, colour, or statistical quantities. A variety of high-level techniques have been investigated to perform segmentation on IVUS and OCT such as elliptic shape prior [32], statistical shape prior [33], including wall thickness information [14], and machine learning [15].

The second part of the thesis focuses on incorporating *a priori* information into our bottom-up segmentation. Although there are many cost function based methods, but finding the optimal formulation is still problematic due to the presence of image artifacts. In this work, a cost

function optimisation is proposed. Instead of using a uniform cost function, the proposed system learns the artifacts and the vessel tissues in each column in a polar-coordinated image and automatically optimises the feature selection to formulate the cost function.

Incorporating shape prior into a graph-based segmentation attracted much attention recently, e.g., [34, 35, 36, 1, 37]. However some of them use a single template [34, 35], depend on the user interaction [1, 37], or require a special number of iterations to converge [36]. In this thesis, a non-parametric shape prior is proposed without any user intervention. The shape prior model is adapted globally and locally in both cost function and the graph construction respectively. Experimental results show comparisons between the proposed method and other shape prior based graph cut methods.

### **1.2.3 Spatio-temporal tracking and segmentation**

The segmentation methods that are carried out on an individual frame basis, are commonly used in IVUS segmentation, e.g., [27], [14],[33]. However, it ignores the temporal information which could help to refine the boundary estimation, particularly when there is large uncertainty due to image artifacts or noise.

The third part of the thesis aims to incorporate the temporal information into the segmentation framework. The border is represented by radial basis functions (RBF). The Kalman filter, a recursive optimal estimator of the system state over time, is used to estimate the border location in the next frame. The incorporation of the predicated Kalman border is achieved by defining a new set of arcs between every two consecutive frames and the final border is obtained by minimising three energy functions based on the boundary cost function, the shape prior model and the temporal constraints. We also propose using the HMM to carry out segmentation and tracking as a faster alternative to the Kalman-based method in terms of finding the final border. The method starts from the border position in the previous frame and searches for the new border along normal lines. The transition probability is learned by using the Baum-Welch algorithm and the emission probability is derived directly from the proposed boundary-based cost function and the shape prior without the need for any training.

## **1.3 Contribution**

The main contributions of this thesis are summarised as follows:

1. Cost function optimisation. A novel column-wise supervised classification is proposed to dynamically formulate the cost function. Haar-like features are extracted from both horizontal and vertical windows and Random Forest is used as a classifier.
2. Shape prior model. A non-parametric estimation method is proposed based on the similarity between an initial segmentation and a set of shape templates to incorporate global shape prior. Graph construction also adapts by defining smoothness arcs between every two neighbouring columns to allow learning-based transition of the border.
3. Spatio-temporal segmentation using the Kalman filter. The Kalman filter is used to provide the temporal information about the border across frames. The measurement of the Kalman filter is defined based on the proposed temporal segmentation of the current frame. The Kalman predicated border is integrated into the system by adding a new set of arcs between every two consecutive frames.
4. HMM tracking and segmentation. HMM is segmenting and tracking the border by searching for the optimal sequence of the hidden states along a set of normal lines to find the corresponding RBF centres of the desired border. These normal lines are evenly sampled over the border in the polar coordinated images. The emission probability of the HMM is directly derived from the proposed cost function and shape prior. The final border is interpolated by using radial basis functions.

Additionally, this thesis includes the following minor contributions: (a) double-interface segmentation method with an auxiliary interface to overcome IVUS imaging artifacts is proposed. (b) circulation density feature is proposed for segmenting OCT images.

## 1.4 Thesis outline

The rest of the thesis is organised as follows.

**Chapter 2 - Literature Review:** provides an overview of the coronary artery imaging modalities and describes the image analysis applications that include segmentation, registration, classification, and reconstruction.

**Chapter 3** - Graph Cut Segmentation: a bottom-up approach: describes feature extraction methods and introduces novel features based on the circulation density. Single and double segmentation methods are proposed. Experimental results for both IVUS and OCT are presented.

**Chapter 4** - Shape Prior Model: presents a novel cost function optimisation based on a supervised classification method to deal with different image artifacts. The proposed shape prior model is introduced to refine the cost function and the graph construction. A comparative study is also presented.

**Chapter 5** - Longitudinal Tracking and Segmentation: describes the border parametrisation, and the proposed tracking method through the Kalman filter and HMM. The results are shown on the longitudinal view of the IVUS and OCT pullbacks.

**Chapter 7** - Conclusions and Future Work: concludes the thesis with discussions of the proposed methods and possible extensions.



## Chapter 2

# Background

### Contents

---

|     |  |    |
|-----|--|----|
| 2.1 | Introduction . . . . .                       | 11 |
| 2.2 | Coronary arterial imaging . . . . .          | 12 |
| 2.3 | Coronary arterial imaging analysis . . . . . | 19 |
| 2.4 | Summary . . . . .                            | 38 |

---

### 2.1 Introduction

There are many imaging modalities for coronary arteries based on different technologies such as ultrasound, near-infrared light, X-ray, and magnetic resonance. The analysis of these imaging modalities is a vital topic due to the increasing interest in reducing the cardiac mortality and morbidity rate by enhancing the diagnosis and treatment of the coronary artery disease. The aim of this chapter is to review both kinds of coronary arterial imaging: invasive and non-invasive. This includes the acquisition procedure, the possible artifacts, and the image analysis techniques.

The common medical image analysis of arterial images includes: image segmentation, including the identification of the arterial walls, image registration, including matching between sequence of images in the same or different modalities, image classification that is the categorisation of the tissues that appear in the image, and image reconstruction that is concerned with reconstructing a 3D image of the artery. Different imaging techniques have their own characteristics that often require different treatment in image analysis.

## 2.2 Coronary arterial imaging

### 2.2.1 Invasive Imaging

Invasive imaging involves insertion of a catheter into the coronary artery of interest in which it reaches its place through a guide-wire. The catheter can be used to flush a contrast dye, balloon inflation, stent implantation, or to be attached to a transducer probe for transmitting and receiving the reflected signals. Invasive imaging can be used to detect stenosis and plaque in the vessel not only in the diagnosis phase but also during the procedures of angioplasty to assess the functionality of coronary arteries and stent deployment. These modalities include X-ray angiography, Intra-Vascular ultrasound (IVUS) and Optical Coherence tomography (OCT).

#### 2.2.1.1 X-ray Angiography

X-ray angiography is the gold standard catheterisation modality for the diagnosis and treatment of coronary arteries disease by showing a silhouette of the vessel lumen but without any information about the wall thickness.

X-rays are an electromagnetic wave like visible light but with much higher energy and very short wavelength. X-rays can be produced in a tube evacuated of air, that has a hot cathode, and anode usually made from a high atomic material, i.e., tungsten, that is connected with a high voltage source. Electrons are emitted by the cathode and travel toward the anode accelerated by a high potential difference, then hit a rotating tungsten disc of the anode and produce directed focus X-ray. The detector of X-ray has evolved from using photographic plates and photographic film to a digital form by using image intensifiers and more recently flat panel detectors.

X-ray imaging is formed by measuring the attenuation which describes the loss of intensity of the X-ray radiation as it penetrates different materials. Medium density, e.g., bones, have more attenuation than soft medium, e.g., body tissues. Since blood and the surrounding soft tissue have similar attenuation, using a contrast agent is essential to visualise the coronary arteries. The injection of the contrast agent, e.g., iodinated contrast, is achieved by inserting a catheter into the coronary circulation through the femoral artery or brachial artery. Digital subtraction angiography is a computerised modification of images to show only the blood vessels without intervention of the background structures, in which images taken before and after the contrast injection are aligned and then digitally subtracted.

An X-ray angiography can be obtained by using a monoplane or biplane system. Monoplane angiography is running separate acquisition steps by moving a C-arm mounting both X-ray emitter and image intensifier detector around the patient to obtain several two dimensional images at different orientations. Whilst the biplane angiography has a pair of emitter and detector working together to simultaneously acquire the projection images in different planes. Recently, rotational X-ray angiography has been introduced, in which it replaces the image intensifier with a flat plane detector and acquires various projections in single rotation of the gantry arm. Rotational angiography [38, 39] gives better diagnosis of lumen stenosis in severe cases than the conventional angiography projections with lower doses of radiation and contrast agent.

#### **2.2.1.2 Intra-Vascular Ultrasound (IVUS)**

Ultrasound image is generated by transmitting ultrasound waves in frequencies higher than human hearing range and receiving the reflected signal from the tissues. Ultrasound has a long penetration depth (10mm in IVUS) and can be transmitted through blood and soft tissue. IVUS is a catheter-based technology that shows 2D cross-sectional images of the coronary. IVUS has been widely used since the early of 1990s as a complementary tool of angiography for better diagnosis of coronary disease in which it provides characterisation of the atherosclerotic plaques, detects plaque rupture, ensures the stent position.

IVUS is acquired by pulling back a catheter through the artery with a constant speed (0.5mm per second). This catheter has an ultrasound transducer that receives the backscatter signal after it transmits the ultrasound waves. Frequencies of the transducers from 20-45 MHz. In general, there are two types of IVUS catheters [40]: single element rotated devices and phased array catheter. A single element catheter consists of one transducer that is rotated at approximately 1800 revolutions per minute. The catheter can be made very thin and vibrates at high frequency up to 45 MHz, thus produces high quality images. A phased array catheter is a non-rotated catheter that has a multi-element transducer in a specific number and order. However it usually has a lower frequency than single element.

An IVUS image is made by taking number of steps: the backscatter signals called radiofrequency singles, can be seen as echo response signals along radii lines (i.e., A-line) at 360 degrees. Radiofrequency signals are a continuous signal that is first sampled to convert it to a digital form. Then time gain compensation is applied to correct the attenuation of the backscat-

## 2. Background

---

ter signals. After that, a band-pass filter is computed to reduce noise effect and remove spectral frequency component. The gray level IVUS image known as B-mode is finally obtained by taking the log transformation of the envelop detected signals.

IVUS imaging artifacts are a common problem for the interpretation of the image and correctly highlight the border of interest. Figures 1.3, 2.1 (a, b, and c) illustrate some examples of IVUS artifacts. These artifacts include:

**Ring-down artifact:** The catheter region appears as a blank circle in the centre of IVUS image. The ring-down artifact is a thick bright band surrounding the catheter.

**Guide-wire artifact:** The guide-wire is attached outside the catheter and causes an artifact by shielding the ultrasound wave in a narrow angle or causing signal reverberation.

**Non-uniform rotational distortion:** This artifact comes from an oscillation in the transducer rotation.

**Calcium shadowing:** Calcium is one of the atherosclerotic plaques that causes a bright echo and drop-out signal behind it.

**Stent artifact:** A stent is a metallic strut that used to reopen the stenosis artery, It causes a bright echo response.

**Blood speckle:** In 40 Mhz or higher frequency IVUS image, the blood speckle has an echo response and it increases exponentially when blood flow velocity reduced, which makes the lumen difficult to differentiate.

### 2.2.1.3 Optical Coherence Tomography (OCT)

OCT is an optical counterpart of IVUS that measures the backscatter signals of near-infrared light rather than ultrasound which enables higher resolution (15-20  $\mu m$ ) than IVUS (100-200  $\mu m$ ). OCT first appeared in 1991 and has been tested on retinal and coronary artery [41]. OCT has clearer visualisation of arterial wall structure, whilst it has much lower penetration depth (1 to 2.5  $mm$ ) compared to 10  $mm$  in IVUS which limits its ability to assess large plaque burden [42].

There are two techniques based on interferometry for the acquisition of OCT: time-domain and Fourier-domain. In the time-domain OCT, the light beam splits into two paths: one directed to

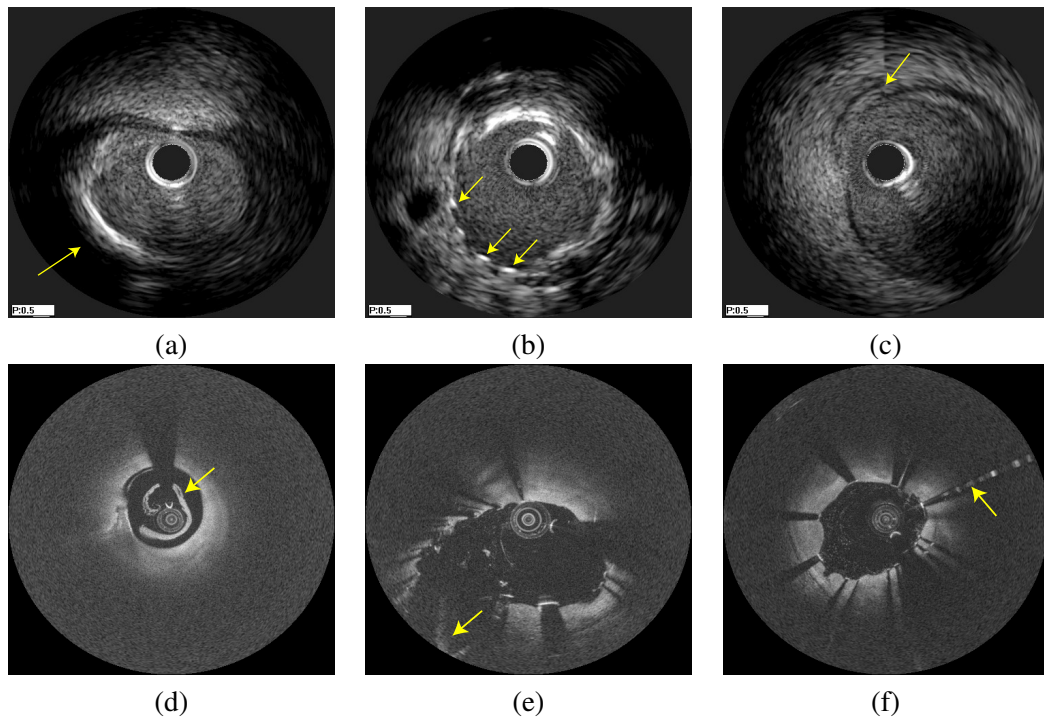


Figure 2.1: Example IVUS and OCT imaging artifacts: (a) Calcium shadowing. (b) Stent artifact. (c) Non-uniform rotational distortion. (d) Residual Blood. (e) Fold-over artifact. (f) Saturation artifact.

the sample arm and is reflected by the tissue and the other to the reference arm. The reference arm is mechanically moving a scanning mirror to reflect echo delays. The detector then captures the interference of the combined light reflected from both arms. When the path length of both arms is matched, the peak intensity of the constructive interference is noted. Time-domain OCT has low imaging speeds and it requires completely clearing the vessel of blood by using an occlusion balloon with continuous flushing during the pullback of the OCT catheter. This may cause myocardial ischemia [43].

Fourier-domain OCT is the next generation of OCT [44, 45]. It works by replacing the mechanical scanning reference arm by a fixed arm and by detecting the spectral interference pattern either through spatially dissolving the spectrum component across an array detector or encoding the spectral component as a function of time using a swept laser source, and thus correspond to two configurations of Fourier-domain systems, spectral domain and swept source respectively. Fourier-domain systems allow very fast pullback with high sensitivity and can use only a contrast agent [46] to temporarily displace the blood without the need of a transient

## 2. Background

---

occlusion balloon.

OCT imaging has a number of imaging artifacts, some of them are similar to the IVUS due to the catheterisation mechanism as shown in Figures 1.3, 2.1 (d, e, and f). These artifacts include:

**Stent shadowing:** The OCT light is unable to break through the metallic stent causing a shadowing behind the stent.

**Saturation artifact:** The stent could reflect a bright beam along the A-line, when the beam comes perpendicular to the stent.

**Residual blood:** The uncleaned blood inside the lumen reflects the light and may cause misinterpretation of the vessel wall or it might be mislabelled as thrombus.

**Guide-wire artifact:** The appearance of the guide-wire artifact is similar to the stent but the brightness of reflection is usually close to the catheter.

**Sew up artifact:** The rapid movement of artery or imaging wire could cause misalignment and distortion.

**Fold-over artifact:** The vessel looks folded when the reflected light occurs outside the system penetration. This may happen with bifurcation or a large vessel.

### 2.2.2 Non-Invasive Imaging

Non-invasive imaging has increasingly been used to examine patients with high risk factors of coronary disease, complaining of chest pain, or after bypass coronary surgery. Non-invasive imaging has many different applications such as depiction of coronary arteries, characterising plaque type, measuring calcium scoring, assessing heart muscle and blood pumping function. Each one of these applications can be accomplished by using one or more image modalities such as computed tomography (CT), magnetic resonance (MR), echocardiography and myocardial perfusion imaging by means of single photon emission computed tomography (SPECT) or positron emission tomography (PET).

### 2.2.2.1 Computed Tomographic Angiography (CTA)

CTA is non-invasive X-ray imaging that provides a three-dimensional detailed structure of the blood vessels and their surrounding tissue. Two CT techniques have been used to retrieve coronary artery imaging: Electron beam CT (EBCT) and Multi-detector CT (MDCT). EBCT is a non-rotated technique that uses an electron gun instead of the traditional X-ray tube to produce a fast electron beam that is focused and deflected along semi-circular rings of tungsten to emit X-rays. The detector is stationary in the upper half of the ring above the patient table. Because of the design of EBCT, it is dedicated only for cardiac imaging. However, EBCT has high temporal resolution but low spatial resolution in longitudinal axis. This reduces its accuracy in severely diseased cardiac cases. EBCT has been largely replaced by MDCT [47].

MDCT is a recent development of spiral (also called helical) CT scanner [48, 49] to overcome the difficulties of volume acquisition in a single patient breath-hold and artifacts introduced by the collimated slice wide which causes some mismatch between longitudinal resolution of slices. MDCT consists of three components: X-ray tube, multi-slice detector, and rotational stage. The X-ray source and its detectors are fully rotated around the patient, while the patient lies on a table that is continuously moved forward in order to obtain cross-sectional images at all orientations. A 3D volume is reconstructed from these images. A contrast agent is intravenously injected before taking CTA images. MDCT has been rapidly developed [50] starting from using 4, 16, to 64 slices and nowadays the number of slices is reaching 320 slices where it significantly improves the isotropic resolution and reduces acquisition time and artifacts. More recently, multi-source multi-slice detector CT has been introduced, and dual source of X-rays [51] has been used to improve the temporal resolution and reduce motion artifacts caused by irregular heartbeat.

CTA has been used in assessment of lumen narrowing and identifying atherosclerotic plaques [52, 53]. However the differentiation of non-calcium plaque components is still intractable. Many radiation dose-saving schemes can be used to make the radiation dose comparable to the level of the invasive X-ray angiography or even less [47].

### 2.2.2.2 Magnetic Resonance Imaging (MRI)

MRI is a non-ionising radiation modality that takes advantage of the intrinsic magnetic properties of body tissues and blood under the influence of an external magnetic field to produce

## 2. Background

---

an image. MRI utilises the fact of the human body consists of 75% water which contains hydrogen nuclei (protons). Protons are spinning in place forming a small magnetic field but in different orientations that neglect each other. When a person goes inside a high-powered magnetic field, these protons are aligned in orientation with the direction of the field. Turning on a radio-frequency pulse at the resonant frequency causing an excitation of the protons. When it is turned off the relaxation process happens in variable time depending on the tissue and a measurable signal is emitted. An additional magnetic field gradient is also used in which it varies the main magnetic field linearly across the longitudinal axis, in order to spatially localise the tissue that emitted the signal to reconstruct the images. A contrast agent, e.g., gadolinium, could be used to alter the relaxation time for better visualisation of the human anatomy.

MRI has been used to evaluate arterial wall thickness and to monitor the progression and regression of vulnerable plaques and its component in large arteries such as carotid [54, 55] and aorta [56, 57]. However, for coronary arteries, MRI imaging is still a challenge because of the relatively small size and the position of the coronary arteries and the cardiac and respiratory motion artifacts. Many initial studies [58, 59] for assessing lumen area and identifying plaque presence in vessel wall are based on (breath-holding or 2D navigator for respiratory motion compensation) black-blood MRI that maximise the signal from static tissue and superseded the blood signal. However it has low spatial resolution and artifacts, e.g., partial-volume effect may cause an overestimation of wall thickness. Multi-contrast weighted MRI [60, 61] has been recently used for coronary arteries. It provides a better resolution and more accurate assessment of plaque components. However, multi-contrast weighted MRI is still a time-consuming acquisition technique.

Magnetic resonance angiography (MRA) is a technique based on MRI imaging modality to show blood vessels and detect stenosis. Many MRA techniques [62] are based on exploiting the circulation of the blood compared to the stationary tissue such as time-of-flight and phase contrast, while some other techniques are blood flow independent, such as steady-state free-precession (SSFP) and contrast-enhanced methods. A magnetic field of MRA scanner at 1.5 Tesla was used for coronary arteries in [63, 64]. However it has a low signal-to-noise ratio, and poor visualisation of small distal branches. SSFP technique [65, 66] showed some improvement on visible vessel length and sharpness. Scanners at 3.0 Tesla are used to increase the image quality, acquisition speed and visualisation of the coronary arteries. Contrast-enhanced methods [67, 68] show superior results than SSFP and contain fewer artifacts. Metallic stent

causes susceptibility and radiofrequency artifacts [69] which may limit the assessment of vessel lumen.

## 2.3 Coronary arterial imaging analysis

### 2.3.1 Vessel Segmentation

Image segmentation is the process of partitioning any given image into distinct, meaningful objects by delineating each object boundary based on a set of extracted features. The vessel segmentation in 2D/3D angiogram images like in X-ray angiography, CTA and MRA is defined by segmenting tubular tree structures of the vessel from the background. The vessel can be just the luminal area as in X-ray angiography or with plaque burden as in CTA and MRA. The vessel segmentation of 2D cross-sectional images of IVUS and OCT means the delineation of vessel arterial walls (i.e., lumen and/or media-adventitia borders).

Many reviews have been published on vessel segmentation [70, 71, 40]. The majority of these vessel segmentation methods can be categorised into three classes: simple region-based approaches, e.g., thresholding, region growing, and morphological operations; energy minimisation approaches, including combinatorial optimisation and deformable models; and machine learning based approaches.

#### 2.3.1.1 Thresholding, Region Growing, and Morphological Operations

Thresholding is a simple image segmentation method in which predefined criteria split a given image into two regions: object of interest and background, so that each region has a distinct feature. Image features in the simplest form are defined by the pixel intensity. However these features might not be suitable for all cases of object separation. Other feature extractions could be used, such as Hessian matrix [12], steerable filter [72] and wavelet features [27, 73]. The selection of the optimal threshold value is a challenging process. Many methods have been used to determine the threshold value, such as a heuristic approach or an adaptive threshold including Otsu's method [74]. However, thresholding is very sensitive to the background noise and feature variation.

Region growing [75, 76] is a more progressive region segmentation method than the thresholding method. It iteratively grows regions starting from an initial set of seed points and joins the neighbouring pixels that satisfy predefined homogeneity criteria. The method may require

user initialisation for the seed points and often causes over or under segmentation of the image that requires further processing [77]. Morphological operations [78] are a set of mathematical operations, e.g., dilation and erosion, applied on binary images that often be used as pre or post-processing step of other segmentation methods, such as thresholding [73] and region growing [79, 80] to improve the segmentation performance.

Several works have been reported using thresholding, region growing and morphological operations to segment coronary arteries, such as [81, 80, 82, 27, 73, 83]. For example, in [27], Papadogiorgaki *et al.* proposed to use discrete wavelet frames to construct decomposition trees to identify vessel wall borders. An initial contour is obtained by applying a threshold to those texture features and then refining by radial basis functions.

### 2.3.1.2 Combinatorial Optimisation

Combinatorial optimisation is a discrete optimisation technique, in which finding the optimum solution from a finite set of feasible solutions by minimising a mapping function called cost function that assigns a cost for each feasible solution subject to a set of constraints. Many combinatorial optimisation problems are represented by a graph or network and can be minimised in polynomial time such as shortest path, max-flow/min-cut, and minimum spanning tree. Typically, a 2D image is represented by a graph  $G(V, E)$ , where  $V$  is a set of vertices that corresponds to image pixels, and  $E$  is the edge set in which each edge is connecting a pair of vertices and associated with a weight or cost. The graph is called directed when the edges are defined with specific directions. Conversely in the undirected graph, the edges have no direction defined. Here, we focus on two main approaches: shortest path and graph cut.

#### A. Shortest Path

Shortest path algorithms solve the problem of finding the optimal path between two vertices in a graph where the total edge costs associated with that path are minimised. The most popular shortest path algorithm is Dijkstra's algorithm [84]. In addition, a heuristic technique [85] and dynamic programming [86] are often used to improve the efficiency and the speed of shortest path search. Dijkstra's algorithm is a single-source algorithm that locates the shortest path from the source vertex to all other vertices in the graph with non-negative edge weights. The algorithm creates a shortest path tree from the source vertex by iteratively adding the vertex that has the lowest distance to the source. Shortest path can be adapted in image segmentation

to delineate the object boundaries but it usually requires some user interaction.

Intelligent Scissors [87], and Live Wire [88, 89] are among early methods to perform on-the-fly segmentation based on Dijkstra's method by allowing the user to follow the object boundary through a few mouse clicks. Gradient magnitudes and orientation are used along with intensity-based features to define the edge weights. However these methods are computationally expensive in segmenting high resolution images due to the repeated search for the shortest paths over the whole image. Live lane [89] improves the computation speed by limiting the search space for shortest paths, at the expense of more user interaction. Falcão *et al.* [90] proposed fast Live Wire method, avoiding the restriction of utilising the previous computation of shortest paths to avoid unnecessary computation following the new input from the user. 3D extension of shortest path segmentation methods have been also introduced in [91, 92, 93].

Several shortest path based methods are used to detect vessel centerlines [94, 95, 96, 97] in angiography images. In IVUS imaging, Sonka *et al.* proposed a semi-automatic method for segmenting the IVUS arterial walls by using a heuristic technique to minimise a cost function based on prior knowledge of the wall thickness and edge features. Similarly, authors in [98] and [99] interactively compute the minimal path on longitudinal images of two perpendicular planes across the IVUS pullback and combine the outcome resulting in the cost function of every individual cross-sectional image in order to identify the optimal paths for the lumen and media-adventitia borders. Recently, authors in [24] proposed a multi-layer shortest path method for segmenting the media-adventitia border. The user can not only input a set of attraction points near the boundary but also can draw region-based strokes, working as soft constraints. The user points are assumed to be placed in a sequential order, which reduces the computational complexity to polynomial time.

## **B. Graph Cut**

Graph cut has been successfully used in many computer vision applications such as image segmentation, restoration, registration, and stereo matching. Greig *et al.* [100] were the first reported using max-flow/min-cut algorithm to estimate maximum a posteriori (MAP) of the Markov Random Field (MRF) model for binary image restoration. The work is then extended for multi-labels [101, 102, 103] and higher-order MRF [104, 105, 106]. The solution of the MRF can be also approximated by using belief propagation [107, 108], tree-reweighted message passing [109], and iterated conditional mode [110].

## 2. Background

---

Boykov *et al.* [29, 111] introduced a general framework [100] for 2D/3D binary image segmentation. The aim is to associate with each pixel  $p \in \mathcal{P}$  in the image, a consistent piecewise smooth label  $f_p \in \mathcal{L}$  where  $\mathcal{L} = \{0, 1\}$ . The cost function  $E(f)$  consists of two terms: data term and smooth term. The data term  $E_{data}$  is the total unary cost of assigning high cost  $D_p(f_p)$  for each pixel  $p$  that is not likely to agree with the labelling  $f_p$  and low cost otherwise. The smooth term  $E_{smooth}$  measures the total pairwise smoothness cost between every two neighbouring pixels  $p$  and  $q$ . It assigns high cost if the two pixels  $p$  and  $q$  have different labelling.

$$E(f) = E_{data}(f) + \lambda E_{smooth}(f), \quad (2.1)$$

where  $\lambda$  is a weight term,  $E_{data}$  and  $E_{smooth}$  are defined as:

$$\begin{aligned} E_{data}(f) &= \sum_{p \in \mathcal{P}} D_p(f_p), \\ E_{smooth}(f) &= \sum_{\{p,q\} \in \mathcal{N}} V_{\{p,q\}}(f_p, f_q). \end{aligned} \quad (2.2)$$

where  $\mathcal{N}$  is the set of all pairs of neighbouring pixels, and  $V_{\{p,q\}}$  is the pairwise interaction potential that penalises the discontinuity between two neighbouring pixels  $p$  and  $q$ . The graph cut can find the global optimal solution of  $E(f)$ , on condition of  $V_{\{p,q\}}$  satisfies the regularity condition:

$$V_{\{p,q\}}(0,0) + V_{\{p,q\}}(1,1) \leq V_{\{p,q\}}(1,0) + V_{\{p,q\}}(0,1) \quad (2.3)$$

Graph cut minimises the energy function  $E(f)$  by finding the optimal cut on a defined graph  $G_{st} = (V \cup \{s, t\}, E)$ , in which two terminal nodes called source ( $s$ ) and sink ( $t$ ) are added to the vertices set  $V$  of the image pixels. Every node in  $V$  is connected to the terminal nodes  $s$  and  $t$  with edges called t-links. In addition, each node is locally connected to its neighbours in a grid-like format (e.g., 4 or 8 neighbourhood system) with edges called n-links. The cost of t-links and n-links edges are derived from the data term  $E_{data}$  and the smoothness term  $E_{smooth}$  respectively and have to be non-negative values. The s-t cut is a subset of edges that partitions the graph into two disjoint sets: the one connected to the terminal  $s$  represents object and the other set connected to the terminal  $t$  stands for the background. The cost of the s-t cut is the sum of edges cost serves on the cut that separates the graph into object and background. The problem of finding the optimal s-t cut is efficiently solved by max-flow/min-cut algorithms [112, 113, 114] in polynomial running time.

Max-flow/min-cut algorithms can be categorised into augmenting path and push-relabel methods. Augmenting path-based methods, such as the Ford-Fulkerson algorithm and Dinic algorithm, work by sending flow along non-saturated paths from the source to the sink until no more paths are available and the maximum flow is reached. Push-relabel algorithms work differently by pushing excess flows toward vertices with a smaller estimated distance to the sink and maintaining a distance labelling of vertices from the sink. The running time complexity of max-flow/min-cut algorithms depends on a number of factors: the number of vertices  $n$ , the number of edges  $m$ , and the maximum edge weight  $u$ . For example, the worst-case running time complexity for the Ford-Fulkerson algorithm is  $O(m^2u)$  and for the Dinic algorithm is  $O(mn^2)$ . Boykov and Kolmogorov [114] proposed augmenting path-based algorithm that empirically outperforms all the previous max-flow/min-cut algorithms despite its worst-case complexity is  $O(mn^2|c|)$  where  $|c|$  is the cost of the minimum cut. This algorithm is used to minimise the proposed energy functions as discussed in the following chapters.

Many methods have been developed to define the data term and smoothness term of the graph cut. In [29, 7], the unary cost is defined by building two histograms for object and background derived from some user strokes. In the Grab Cut [115], the authors proposed to use a Gaussian mixture model to build a local colour model to improve the unary term. It reduces the user intervention by allowing the user to define a rectangular window surrounding the object. Lazy Snapping [116] is applying the graph cut over a pre-segmented image using a watershed algorithm. K-means is used to cluster the foreground/background colours and assign each pixel to the nearest cluster to define the data term. The method also has a boundary editing tool to refine the result. The smoothness term is usually defined based on the edge features, e.g., gradient magnitudes. However, these methods usually need multiple user interventions to correctly cut out the object, due to the simplicity in cost function and ambiguities in images.

Many variations of the conventional graph cut have been introduced to solve different segmentation problems, such as incorporating shape prior [35, 36, 37, 117, 1], approximating continuous Riemannian metric space [118, 119], clustering [120, 121, 122], dynamic graph cut [123, 124], and finding the optimal surface in N-D graph [8]. Li *et al.* [8] proposed a method for simultaneously detecting multiple optimal surfaces in N-D graph. The method constructs a weight directed graph for each surface to impose geometric constraints, e.g., defining surfaces smoothness and interrelation. The method finds the optimal surface by converting the problem into computing the minimum closed set graph that eliminates the need for any user interac-

tion. It can be efficiently solved by the max-flow/min-cut algorithms. We extend this graph cut method to segment IVUS and OCT images, by optimising cost function, incorporating shape prior, and imposing temporal constraints.

Graph cut methods have been used in vessel segmentation, e.g. [15, 125, 126, 127, 128, 129]. For example, in [15], authors adopted the optimal surface method [8] to segment the IVUS arterial walls, its cost function consists of three terms: Rayleigh distribution, Chan-Vese function, and learned border patterns. However the method ignores the IVUS artifacts which inevitably exist in any IVUS pullback. K. Tung *et al.* [128] used a combination of expectation maximisation and graph cut to initially segment the lumen border in OCT imaging, then corrected the segmentation by computing a convex hull to remove the guide-wire artifact. In Chapter 3, the proposed double interface segmentation is compared to the conventional graph cut method.

### 2.3.1.3 Deformable Model

Deformable models are elastic curves or surfaces which react according to applied forces and constraints. They have been increasingly used in medical image analysis [130, 131, 132] as a result of its ability to cope with the variability of the human anatomical structures. Curves or surfaces are deformed by undergoing two kinds of forces: internal and external. Internal forces maintains the shape smoothness of the model. External forces are derived from the image features in order to guide the model to the desired location or configuration. Deformable models can be categorised as: parametric model and geometric model, based on the representation of the shape. Parametric models, also known as active contours or snakes, use explicit parametric representations for curves or surfaces in image domain. On the other hand, geometric models are implicitly representing the model by using distance transform function in higher dimensional space and deforming the model according to the curve evolution theory [130] and the level set method [133, 134].

#### A. Parametric Models

The formulation of parametric models can be written as an energy function so that the curve evolution is realised by minimising a combination of internal and external forces. Let the deformed curve is defined as  $V(s) = (x(s), y(s)), s \in [0, 1]$ , where  $x(s), y(s)$  are x,y coordinates

and the contour length  $s$  is normalised. The energy function can be described as:

$$E(V) = E_{int}(V) + E_{ext}(V). \quad (2.4)$$

The internal energy functional is defined as:

$$E_{int}(V) = \frac{1}{2} \int_0^1 \alpha(s) \left| \frac{\partial V}{\partial s} \right|^2 + \beta(s) \left| \frac{\partial^2 V}{\partial s^2} \right|^2 ds, \quad (2.5)$$

where  $\alpha(s), \beta(s)$  determine the elasticity and rigidity of the model by controlling the first-order and the second-order derivatives. The external force  $E_{ext}(V)$  is derived from the image data over which the curve evolves. For example, given a gray-level image  $I(x, y)$ , the edge-based functional can be defined as:

$$E_{ext}(V) = - \int_0^1 |\nabla[G_\sigma * I]|^2 ds, \quad (2.6)$$

where  $G_\sigma$  is a Gaussian kernel of standard deviation  $\sigma$ ,  $\nabla$  is the gradient operator, and  $*$  is the convolution operator. The energy function  $E(V)$  can be written as an Euler-Lagrange equation so that the energy minimisation is achieved by finding the solution of this equation starting from initial contour parameters. Many energy function minimisation methods have been introduced such as gradient descent [135], and dynamic programming [136].

Parametric models suffer from a number of shortcomings: the models often depend on a good initialisation of the contour in terms of their location and the number of control points to achieve meaningful results and can generally only capture one region of interest per model. Parametric models have difficulties to handle topological changes, such as splitting or merging, and this motivates alternative representations.

The external force that relies on the image gradient is generally sensitive to noise and prone to local minima. Defining the external force has been extensively studied in the literature. In [135, 137], the external force extended to a multi-scale Gaussian kernel to highlight edges more accurately. Cohen [138] proposed a balloon force that could be inflated or deflated to allow more flexibility of the initial contour position. Cohen and Cohen [139] used a distance map between each pixel and the nearest boundary, however the deformation is intractable when the boundary has concavity. Xu and Prince [140] improved its performance by using gradient vector flow in which it diffuses the edge map gradient far from the boundary. Region-based external force methods [141, 142, 143] were proposed where the curve or surface is assumed

to split the image into object and background regions each of which has its own statistical characteristics. User interaction could also be incorporated into the external force, e.g., [135].

For IVUS segmentation, authors in [144, 145] proposed to apply nonlinear diffusion to enhance edges, then to use a statistical classification [145] to define vessel map and finally to apply a snake model to detect the media-adventitia border. In [146], preprocessing operations including edge detection and hough circle transform are carried out to convert the IVUS image to binary. Then gradient vector flow is employed to highlight the two vessel walls sequentially. In [147], the authors proposed an automatic initialisation of an active contour method based on a heuristic thresholding of extracted wavelet features. In [148], a Hopfield neural network is used to minimise the energy function of a snake model, in which an operator initialises the contour in the first frame and the resultant border is used as an initialisation for segmenting the next frame. In [149], the authors introduced a semi-automatic 3D active contour method where the external force is defined on the gradient information. However, the user intervention is necessary at several intermediate frames, including the first and the last one. Brusseau *et al.* [28] proposed an automatic active contour method by fitting Rayleigh distributions to segment the lumen border. In [150], an active contour method is used to segment OCT images, after applying Otsu's thresholding and morphological operations to convert the image to binary. The method requires user intervention when the difference between the vessel wall contour and a fitted ellipse shape is greater than a threshold value, in order to reduce the irregularity of the contour.

### B. Geometric Models

Geometric models are based on the level set method or geodesic active contours, which are introduced to tackle some of the problems of the parametric model by evolving curves or surfaces using a geometric estimation which is independent of any explicit parametrisation. Let  $X(s, t) = [x(s, t), y(s, t)]$  be a moving curve with  $s$  parameters,  $\kappa$  its curvature, and time  $t$ , and its inward normal  $N$ . The curve is propagating along its normal direction in accordance with a partial differential equation:

$$\frac{\partial X}{\partial t} = F(\kappa)N, \quad (2.7)$$

where the speed of curve evolution is determined by function  $F(\kappa)$  called the speed function. In curve evolution theory [130], the curve deformation can be accomplished by using curvature

deformation. Comparing to parametric models, curvature deformation has a similar influence as internal force, while constant speed deformation is equivalent to the balloon force. The geometric model combines the curve deformation methods with the data derived from the image, in order to evolve the curve until reaching the object boundaries.

The level set method is connected to the curve evolution theory by defining the curve at zero level of a signed distance function in a higher dimensional space, in which replacing the curve parametrisation by a level set function evolved over time. Given the curve  $X(s, t)$ , the embedding level set function  $\phi(x, y, t)$  is defined as:

$$\phi[X(s, t), t] = 0. \quad (2.8)$$

By differentiating the equation (2.8) with respect to  $t$  and using the chain rule, we have:

$$\frac{\partial \phi}{\partial t} + \nabla \phi \cdot \frac{\partial X}{\partial t} = 0. \quad (2.9)$$

Considering equation (2.7), and assuming that  $\phi$  is negative inside the zero level set and positive outside, and that the inward normal is defined as  $N = -\nabla \phi / |\nabla \phi|$ , equation (2.9) is rewritten as:

$$\frac{\partial \phi}{\partial t} = F(\kappa) |\nabla \phi|. \quad (2.10)$$

The original speed function proposed in [151, 152] is described by adding together curvature and constant deformations which are then weighted by stopping term  $c$ , which is defined based on the gradient of Gaussian smoothed image:

$$\frac{\partial \phi}{\partial t} = c(\kappa + V_0) |\nabla \phi|, \quad (2.11)$$

where

$$c = \frac{1}{1 + |\nabla(G_\sigma * I)|}. \quad (2.12)$$

$\phi$  represents the evolving level set function and  $V_0$  is the constant deformation term where positive value shrinks the curve and negative value expands it. However, weak edges or gaps cause the curve to continuously evolve without stopping. Many works [153, 154, 155] have been proposed to solve the problem by introducing an extra stopping term. Region-based methods, such as [156, 157, 158], usually suffer less from this problem. For example, Chan and Vese proposed a piecewise constant approximation of the Mumford-Shah functional for

two regions in which the delineation of the object region is based on the average intensities inside and outside the contour. Later, authors in [157] extended the method to deal with multi-regions (phase). In [158], authors proposed multiple level set functions, one for each region, and combining region statistics from Gaussian Mixture model with edge information. Xie and Mirmehdi [159] combined the gradient flow forces with diffused region constraints for dealing with image noise and weak edges.

Shape prior model has been integrated into the deformable model by using different schemes such as principal component analysis (PCA) [160, 161], kernel PCA [162], statistical model [163] and nonparametric density estimation [164, 165]. Recently, many other techniques apply some physics principles on the deformable models such as [166, 167, 168]. Notably, Xie and Mirmehdi [168] proposed applying a magnetic force as an external force to attract the active contour towards object boundaries which would improve the model convergence to deep concavities and in dealing with weak edges. Xie in [169] extended this method into an initialisation-invariant edge-based active contour, which provides more freedom in contour initialisation. Yeo *et al.* [170] introduced a 3D extension of this method, and provided a more general framework by reformulating the external force and applying the analogy of geometric interactions between the deformable model and the image objects. The bidirectionality of the force permits this method to handle arbitrary cross-boundary initialisations and weak edges.

For IVUS segmentation, in [22], Cardinal *et al.* assumed that each region consists of uniform scattering tissue and has its own distinctive Rayleigh distribution. However, it is expected that arteries captured in IVUS contain various forms of diseased tissue which greatly compromise their assumption. Unal *et al.* [33] used signed distance function to implicitly represent prior shapes and applied principal component analysis (PCA) to generalise the shape variation. Its automated initialisation of the media-adventitia border, however, is based on the maximum gradient information which is susceptible to imaging artifacts.

### 2.3.1.4 Machine Learning Based Model

Machine learning is one of the major branches of the artificial intelligent which aims to develop systems that can learn to do tasks. Machine learning has been used in many medical applications such as computer-aided diagnosis [171, 167], prognosis [172, 173], image retrieval [174], and image segmentation [175]. Different machine learning approaches have been introduced which can be categorised based on the learning strategy. Clustering methods are unsupervised

learning approaches where the input data is given without association with the target labelling, hence the clustering methods learn the intrinsic structures that partition these data. On the other hand, supervised learning approaches assume that the training data are provided with the associate labelling so that it can recognise the unseen data pattern based on this knowledge.

Clustering is used in region-based segmentation where the data set is partitioned such that each cluster has the same homogeneous attributes such as intensity, colour or texture. The clustering has many different schemes and has been used in vessel segmentation, such as K-means [176], expectation maximisation [128] and fuzzy C-mean clustering [177, 26]. K-means is hard unsupervised clustering in which each pixel can only join one cluster. The idea of K-means is defining a centroid at the initial centre for each cluster and assigning each sample in the data set to the nearest centroid by measuring the distance between them, then update the centroid in an iterative manner. In Chapter 4, K-means clustering is incorporated into the proposed shape prior model.

Supervised learning methods include, among many others, supervised neural network, support vector machine (SVM), random forest, and boosting. SVM was proposed by Cortes and Vapnik [178, 179]. It finds a hyperplane with the maximal margin that separates the feature space into two sample groups. The input data is often transformed into higher dimensional space using a kernel function, so that SVM can separate nonlinear cases. SVM was originally designed for binary classification, but it can be extended to be a multi-class classifier [180] by using, for example, one-versus-all or one-versus-one techniques. Boosting is an ensemble-based method that combines a set of weak classifiers to create a strong classifier. Since Freund and Schapire [181] introduced the AdaBoost algorithm, many variations have been proposed, such as Realboost, GentleBoost, LogitBoost, and so on [182]. Viola and Jones [183] proposed a cascade classifier based on AdaBoost which has been successfully used in object recognition and in real time application. The decision of ensemble-based methods is usually computed by carrying out majority voting. Random forest (RF) is another popular ensemble classifier of a refined bagged trees. Random forest injects the randomness not only by training each tree on different training sets using a bootstrap sampling but also with a random set of features that is drawn at each node to determine the best tree splitting. In Chapter 4, random forest classifier is used to optimise the definition of the cost function.

Nekovei and Sun [184] segmented the blood vessel in X-ray angiography using a backpropagation neural network. The neural network is trained on pixel intensities extracted from small

subwindows across the image which it uses to classify the pixels as vessel and non-vessel. Authors in [185] used a multi-stage random forest classifier to detect seed points of the vessel location in X-ray angiography, in which three standalone RFs are sequentially applied based on vesselness, eigenvalue, and effective margin features in order to reduce the false negative rate. In CTA imaging, Kelm *et al.* [186] extracted the vessel centerlines by computing the minimum cost path and proposed using the regression RF based on rotational invariant features [187] to identify the cross-sectional area of the vessel lumen along the centerlines. Zheng *et al.* [188] introduced a machine-learning vesselness method using a probabilistic boosting tree. The method segments the whole heart and detects the two coronary ostia as a preprocessing step so that the probabilistic boosting tree method is implemented on the heart surface by assigning high score for each voxel inside the vessel and low score otherwise based on a set of extracted geometric and image features.

In IVUS imaging, authors in [189, 190] proposed delineating the lumen border using AdaBoost and using SVM respectively. In [189], the IVUS image is converted to a longitudinal view and the AdaBoost algorithm is trained by selecting the most relevant features from a pool of texture features. Morphological operations and then a snake model are run on the resultant labelling map to define the border. In [190], the lumen border is specified by minimising a probabilistic cost function obtained by using the SVM classifier, where SVM is trained on texture features to give a likelihood of each pixel belonging to blood and non-blood regions. The training data is supplied by the user through highlighting some positive and negative regions on the first frame of the IVUS sequence.

### 2.3.2 Tissue Characterisation

Tissue characterisation is the process of evaluating a medical image to identify the type of tissue component. Tissue classification of coronary arteries is not only used to segment the vessel as aforementioned but also in many clinical applications that include plaque characterisation, stenosis detection [186], assessment of stent strut apposition [191], or measurement of in-stent neointimal hyperplasia [192]. Atherosclerotic plaques are the most interesting tissues to be classified that can be measured using different image modalities, e.g., IVUS, OCT and CTA. Atherosclerotic lesions are commonly recognised as responsible for acute vascular events [193]. The type of plaques include fibrotic, lipid-rich, and calcific plaques, each of which has distinct features that change from one image modality to another. For example, In IVUS,

lipid-rich plaque has low backscatter signals that appear as dark regions, fibrous tissue has a homogeneous collagen region with a medium echo reflection, and calcium has a high echo reflection followed by shadowing. In OCT, calcium has low reflection and is surrounded by sharp edges, poor-signal regions that are caused by lipid-rich regions with diffused edges, and fibrotic plaque is shown as a homogeneous highly reflective region.

There are two main approaches to tissue characterisation: radiofrequency-based and image-based. Radiofrequency-based approaches [194, 195] are spectral analysis of the backscattered radiofrequency signals into four different plaque components: calcium, necrotic core, fibrous and fibrolipidic, where necrotic core is a mixture of cholesterol clefts, foam cells and micro-calcifications. Some IVUS machines come with a plaque characterisation system known as IVUS-Virtual Histology (VH) that colour-codes each plaque type reconstructed from radiofrequency signals. However, IVUS-VH requires the electrocardiogram (ECG)-gated acquisition that unavoidably removes IVUS frames at the intermediate of cardiac cycle.

Image-based approaches [196, 197, 198, 199, 200] consist of the extraction and selection of a set of features from the gray-level image and applying a classification scheme to detect the tissue components. Many kinds of image features have been extracted based on pixel intensities, texture, and geometric features. Texture features include a co-occurrence matrix, local binary patterns, wavelet features and Gabor filters. Geometric features include, for example, the relative position to the vessel border. The classification scheme is usually accomplished using one of the machine learning methods, such as SVM, random forest and neural network.

#### 2.3.3 3D Vessel Reconstruction

X-ray angiography remains the gold standard diagnosis modality for coronary arterial diseases, although many aforementioned modalities have been developed. The diagnosis is based on a set of views selected by cardiologist from several two-dimensional angiographic images acquired on different perspectives to subjectively minimise foreshortening and vessel overlap. However, this is associated with high intra-observer and inter-observer variability. The quantitative coronary analysis of these two-dimensional views often suffers from a magnification factor and superimposition effects. Thus, 3D reconstruction of vessels can compensate for the X-ray angiography limitations. Green *et al.* [201] showed that the selective views still have a lot of vessel foreshortening that may affect the assessment of stenosis and the placement of stents compared to 3D reconstructed vessels. 3D reconstruction of vessels [202] allows esti-

## 2. Background

---

mation of vessel diameter, length, volume, and angles at vessel branching points and tortuosity.

Many 3D vessel reconstruction methods have been proposed over the last two decades using various types of acquisition systems: monoplane [203, 204, 205, 206], biplane [207], and rotational systems [18, 208]. 3D reconstruction of vessels is based on calibrated or uncalibrated data models. In calibrated models [209, 204, 205], projection data is obtained independently prior to or during the acquisition of angiogram data by using a calibration phantom. Uncalibrated models [210, 207, 203] require a minimum number of matching points in two images usually manually identified at bifurcation points and end points to implement an optimisation algorithm for calculating the projection geometry.

The 3D reconstruction method of vessels can be categorised as low-level approaches and energy minimisation models. Most low-level methods [210, 207, 203, 211, 205, 18, 206] include four steps: 1) finding the projection geometry and correcting image intensifier distortions; 2) segmenting the angiogram images to extract the vessel centreline, diameter, and bifurcation points; 3) identifying the correspondence of vessel centerlines based on the well-known epipolar constraint; 4) calculating 3D coordinates for each corresponding pair of vascular points to construct the 3D coronary tree.

In [207], the authors proposed a 3D reconstruction method of biplane images to assess coronary artery disease. The method uses an iterative method to estimate the geometric parameters by statistical analysis of reconstruction error. An operator interactively determines the correspondence points in two projections and these points are also used as a guide to segment the vessel in each image. The vessel is reconstructed based on an elliptic cross-sectional contour derived from the vessel centreline and edges. In [203], Chen and Carroll used a semiautomatic deformation model to segment the vessel tree and proposed a nonlinear optimisation method to define the transformation parameters between two views taken from a monoplane system. The 3D reconstructed vessel is used to calculate the percentage of vessel foreshortening and overlap, and select the optimal views in terms of the gantry angles that minimise vessel overlap. In [205], Movassaghi *et al.* introduced a 3D reconstruction method from two or more projection views. An automatic detection method of vessel centreline and width was proposed. The geometry data is predetermined by using calibrated phantom data. In [206], the authors proposed a nonlinear optimisation method of two angiographic views which takes into account the influence of table movement to refine the 3D structure of the vessel tree. Blondel *et al.* [18] proposed a vessel reconstruction method using a rotational X-ray sequence. The method first

selects a set of reference images at the same cardiac phase but from different angles to remove the effect of cardiac motion. Then the vessel centreline is extracted using a thresholding based method. A matching algorithm is proposed to find the correspondence between the reference centerlines, taking into account the amount of respiratory motion compensation. The method uses the 3D vessel model to estimate the cardiac motion, and also produces a 3D tomographic reconstruction of coronary arteries.

Energy minimisation models include the deformable model [209, 204, 212] and graph cut methods [208]. Radeva *et al.* introduced the 3D reconstruction problem as a minimisation of the snake model, in which the vessel segmentation and reconstruction steps are combined and directly obtain the 3D vessel positions, without the need for using epipolar constraints to find matching points. Canero *et al.* incorporated the geometrical distortion estimation into the snake model to improve the image quality and the extraction of vessel centerlines. The external force of the snake model is based on generalised gradient vector flow. In [212], the authors proposed the external force of the snake model based on image gradient and prior knowledge. User interaction is required to define the geometry transformation and the initialisation of the snake model. Liao *et al.* [208] formulated the 3D reconstruction of vessels from multiple views as a minimisation of the graph cut problem. Vessel centerlines are segmented using hysteresis thresholding and then refined by an interactive method based on fast marching. The graph cut is used to solve the multi-view matching problem by incorporating a soft epipolar constraint and a smoothness term in 3D space. However, the method does not take into account compensation for the breathing motion.

#### 2.3.4 Image Registration

Image registration is the process of determining the anatomical or functional correspondence between two or more images. The images are acquired of the same object at different times, from different perspectives and/or by multiple image modalities. The problem is to geometrically align two images by deforming one image to closely match the other reference image so that the pair can be fused, compared or analysed. Image registration has a vital role in many medical applications, such as monitoring disease progression or structural changes [213, 214] via multi-temporal image registration, atlas-based image segmentation [215, 216, 217], multi-modal image fusion by registering images from different modalities, and motion analysis [218] and correction [219] through measuring the dynamic of stack images acquired across time.

Many reviews of image registration approaches have been published [220, 221, 222, 223]. These approaches include the following components: 1) Transformation model: it specifies a geometric transformation between the images. Several types of transformation can be used such as rigid, affine, projective, and deformable transformations; 2) Similarity metric: it measures the similarity between the target and reference images and can be categorised into features-based and intensity-based measurements; 3) Optimisation method: it is usually an iterative method that finds the maximum (or minimum) similarity (or dissimilarity). Let  $I_r$  denote the reference image and  $I_t$  the target image. The aim of registration is to find the geometric transformation parameters  $\mathcal{T}(\cdot)$  that maximise the similarity measures  $\mathcal{D}(\cdot)$  between the two images:

$$\mathcal{T}^*(\cdot) = \underset{\mathcal{T}(\cdot)}{\operatorname{arg\,max}} \mathcal{D}(I_r, \mathcal{T}(I_t)). \quad (2.13)$$

Transformation models are classified as rigid and nonrigid models. The rigid model uses an explicit regularisation to restrict the degrees of freedom in the transformation. The simplest rigid transformation only involves rotation and translation. Affine transformation has additional scaling and shearing parameters to the rigid transformation. Projection transformation is a more general transformation that preserves collinearity and addresses the situation when the image plane is different from the object plane, which can be used to achieve 2D-3D registration [224]. More complex objects can be handled with non-rigid transformation such as soft tissue deformation [225]. Non-rigid transformation allows more degrees of freedom and local deformation, whilst keeping a large number of controlling parameters, which can be modelled parametrically and nonparametrically. Parametric transformation is deforming the model using a combination of basis functions. The model is derived using function interpolation and approximation theory. Splines and Radial basis functions are widely used as basis functions. Free-Form deformation [226] is another form of non-rigid modelling in which the image to be deformed is enclosed within meshes of control points. B-spline is often used as an interpolation function between control points to produce smooth and continuous transformation.

Nonparametric models provide a great flexibility in the transformation and can be used to model nonlinear soft tissue deformations. However, these models are often computationally expensive. Nonparametric models are based on physical models such as elasticity, fluid flow, and optical flow. Elastic models manipulate the deformation process as a stretching of an elastic medium using two forces, internal and external, until the forces reach equilibrium. However, an elasticity assumption is only applicable to small deformations. The fluid flow model allows

large and highly localised deformations. The viscous fluid model [227] uses a velocity field to describe pixel motion rather than the displacement field as in the elastic model to allow the restoring forces to relax over time. Christensen *et al.* [228] proposed a hierarchical sequence of transformations using affine, linear elasticity and a fluid flow algorithm respectively that evolves velocity fields over time. Later authors in [229] proposed a faster version. Thirion [230] modelled the registration process by using a diffusing model and incorporated the optical flow concept of intensity conservation between images to a nonrigid matching algorithm. Nevertheless, the algorithm may not maintain the topology. Fluid and elastic model can be formulated as partial differential equation (PDE) problems [222].

Similarity measures can be categorised as features-based and intensity-based. Feature-based registration approaches include manually or automatically extracting a set of features, e.g., points, lines, or surfaces from the reference and target images, in order to minimise the disparity between the corresponding features, and therefore the registration problem is moved to the geometrical domain rather than the intensity domain. For point-based registration, if the correspondence between features is known beforehand, the substantial purpose of the registration is to find a transformation that aligns these points. Points can be detected by automatic segmentation or they can be interactively based on anatomical landmarks that are discernible in both registered images, e.g., papillary muscles and the inferior junction of the right ventricle in the heart are highlighted to accomplish Echo-PET registration [231]. Alternatively, a marker attached to the patient extrinsically can be used for more accurate registration. For rigid transformation, the alignment of two sets of corresponding points is achieved by minimising the square distance between the points by using a singular value decomposition [232]. If the correspondence between feature points is unknown, an iterative closest point algorithm [233] can be used. Features-based similarity measures can be used in both mono- and multi-modality registration, however the reliability of the registration is related to how accurate the extracted landmarks are.

Intensity-based registration is based on the relationship between image intensity values, in order to find a spatial transformation that maximises the similarity between registered images. The simplest similarity measure is defined as the sum of the square difference (or the sum of the absolute difference) of intensities in the two images. Other measures may use a correlation coefficient, assuming a linear relationship between images. However, these similarity measures are limited to mono-modal registration. For multi-modal registration, the correlation ratio is

proposed to measure the functional relationship between the two images. Information theory is another popular approach, e.g. mutual information, utilises the marginal and joint entropies of two images to measure the amount of shared information. Various optimisation methods [234, 235] can be used, such as gradient descent, quasi-Newton, LevenbergMarquardt and so on.

The registration of coronary artery images is to substantially reduce motion artifacts. One of the applications of the registration in X-ray angiography is digital image subtraction [236, 237, 238, 239], which aims to improve the visibility of the coronary arterial tree and remove the background noise by aligning and subtracting both mask and live images. Moreover, image registration has been applied between 2D cross-sectional images, e.g., IVUS [240, 241, 17, 16] to improve the longitudinal view by decreasing the catheter displacement as a result of the heart motion or the tortuosity of vessel. In [241], authors proposed a rigid registration method by changing the origin of the reference coordinates to the centre of mass of the image and then estimating the rotation amounts between the two images using spectral correlation analysis. In [17], a set of salient points on the vessel wall is detected using a neural network to compute an elliptical approximation of the vessel, then the rotational parameters are estimated between every two consecutive ellipses. Similarly, authors in [16] approximated the vessel as a circle and adapted a method of fast radial symmetry transformation to estimate the centre and radius of the vessel and then used a spectral correlation analysis to find the rotation between two subsequent IVUS images. In [240], a nonrigid transformation method using thin-plate spline is proposed to find the optimal matching between landmarks defined on a feature space of two IVUS images. The method detects the vessel by using an active contour applied on anisotropic diffused image to extract a set of landmarks on the vessel border, and then describes each landmark by contextual features based on a generalised correlograms. The method is also used as an image retrieval tool.

### 2.3.4.1 Multimodality Image Fusion

Image fusion is the integration of different image modalities acquired independently of the same object into a single display, allowing a more robust scheme in diagnosis, e.g., cardiovascular diseases and risk assessment by collecting complementary information on the underlying anatomy and physiology to overcome the limitation of using single image modalities. Image fusion has been successfully applied in medical applications [242], usually by superimposing

anatomical and functional modalities. For example, fusion of cardiac PET/CT or SPECT/CT [243, 244] takes the advantage of both modalities, in which high calcium scoring detected by CTA is associated with a higher likelihood of myocardial ischemia although there is normal perfusion in SPECT or PET, whilst the stress myocardial perfusion provides valuable hemodynamic information about the physiological significance of coronary artery stenoses to enhance the detection sensitivity and specificity of using the standalone CTA. Moreover, new hybrid scanners have been introduced to obtain the images from multimodality in a single setting and produce an attenuation correction of myocardial perfusion images in PET/CT or SPECT/CT Modelling.

To analyse the coronary arterial disease, several extensive works have been proposed to fuse X-ray angiography/IVUS [245, 246, 247, 19, 248, 249, 250] and X-ray angiography/OCT [251, 252]. Most of these works follow similar steps: 1) segmenting IVUS (or OCT) images to obtain the borders of interest; 2) extracting the catheter trajectory from the angiography; 3) assigning IVUS (or OCT) images on the catheter path and calculating their axial rotation and orientation.

The extraction of the catheter path from a biplane angiography is done basically to estimate a 3D path in similar ways as in 3D vessel reconstruction [246, 248, 19]. However, the assumption that the vessel centreline coincides with IVUS transducer tip as in [245] is not always satisfied. In [246, 248], a calibration of the transducer position is accomplished before taking the IVUS images. In [247], several X-ray images for the transducer path is captured through testing in vitro data. A semi-automated detection is adapted in many other works using a dynamic programming method [19] or a B-spline approximation [249]. Assigning the IVUS frames to the catheter path is based on utilising the physical properties of the motorised pullback which has a constant pullback speed [19, 249] or can be supervised manually [246, 247, 248]. The axial twist of IVUS frames is estimated for example by solving the best matching problem between IVUS luminal contour and the correspondence in angiography [246, 247, 248], or based on an approximation of Frenet-Serret formulas [245, 19, 249]. The final output is usually displayed as a 3D reconstructed IVUS stack fused on an angiographic vessel. Very recently, Wang *et al.* [250] proposed a co-registration method that synchronises the time between the IVUS and angiography without the need to do a 3D reconstruction. An interactive method is used to segment the vessel branch in angiography images, then the catheter tip and the IVUS transducer in the fluoroscopy images are learning based detected and tracked, and finally the

mapping stage between the IVUS transducer and the vessel is carried out based on the geodesic distances. Other attempts to fuse IVUS/OCT [253, 254] and IVUS/CTA [255, 256, 257, 258] have been also introduced, most of which are based on the registration of the corresponding anatomical landmarks between the two different modalities.

### 2.4 Summary

In this chapter, the necessary background is presented in preparation for describing the proposed methods in this thesis. The review was divided into two main sections. One was concerned with the different image modalities, and the other with the possible image analysis techniques for coronary arteries. IVUS and OCT are seen as an essential complementary tool to assess the pathology of coronary arteries. Vessel segmentation is important not just for the detection of stenosis but also to allow a lot of further computational processing, e.g., wall shear stress computation. Vessel segmentation plays a vital role in many different medical image analysis applications such as tissue characterisation, vessel reconstruction, intra-model image registration, and multi-model image fusion.

Graph cut and deformable models are widely used techniques to perform segmentation. However, many deformable models depend on the user initialisation and may be prone to local minima. Moreover, weak edges or gaps that are commonly existed in medical images may cause the deformable models to evolve without converging properly. Graph cut is a discrete optimisation that performs global minimisation of the energy function. Each image pixel is represented by a node and the relationship between pixels is expressed by a set of edges, that give an advantage to impose geometric constraints and globally or locally adapt the graph for robust segmentation. In the following chapters, we propose graph cut based methods to segment IVUS and OCT images, that involves optimisation of the cost function, incorporation of shape prior, and the use of temporal constraints.

## Chapter 3

# Graph Cut Segmentation: A Bottom-Up Approach

### Contents

---

|     |  |    |
|-----|--|----|
| 3.1 | Introduction . . . . .                             | 39 |
| 3.2 | Preprocessing . . . . .                            | 41 |
| 3.3 | Feature Extraction . . . . .                       | 42 |
| 3.4 | Single and Double Interface Segmentation . . . . . | 46 |
| 3.5 | Results: IVUS . . . . .                            | 51 |
| 3.6 | Results: OCT . . . . .                             | 56 |
| 3.7 | Summary . . . . .                                  | 60 |

---

### 3.1 Introduction

Both IVUS and OCT imaging are catheter-based technologies, which show two-dimensional cross-sectional images of the coronary structure. There are two types of borders of interest: the lumen-intima border, which corresponds to the inner arterial wall, and the media-adventitia border, which represents the outer coronary arterial wall. The appearance of both borders in IVUS or OCT images is affected by various forms of imaging artifacts, such as acoustic shadow caused by the catheter guide-wire, calcium in IVUS, or stents in OCT.

### 3. Graph Cut Segmentation: A Bottom-Up Approach

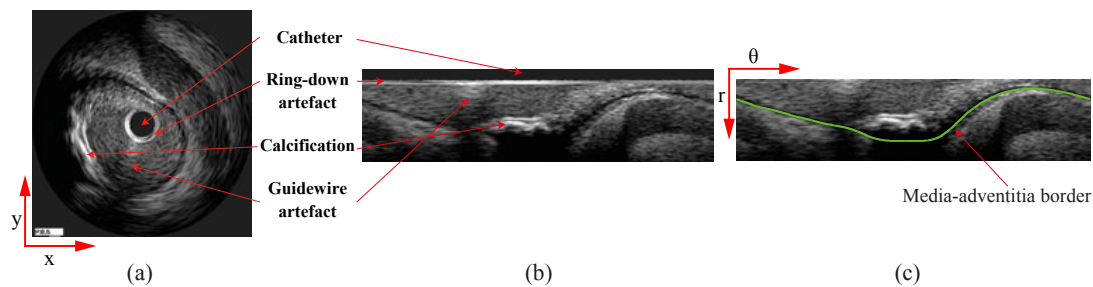


Figure 3.1: (a) An original IVUS image. (b) Polar transformed image. (c) After removing the catheter region (green curve shows the ground-truth of media-adventitia border).

Among many other techniques as reviewed in Chapter 2, formulating the IVUS and OCT segmentation as a combinatorial optimisation of a cost function based on local image features has been a popular approach. In [14], dynamic programming is used to search a minimum path based on a cost function that incorporates edge information with a simplistic prior relying on assumed echo pattern and border thickness. Manual initialisation is generally necessary. In [13], the border detection is carried out on the envelope data before the scan conversion. The authors applied spatio-temporal filters to highlight the lumen, based on the assumption that the blood speckles have higher spatial and temporal variations than the arterial wall, followed by a graph-searching method similar to [14]. However, image features introduced by acoustic shadow or a metallic stent would seriously undermine the assumption. Catheter movement can also cause spatial and temporal fluctuations, which leads to ambiguities. The  $s-t$  cut method [8] is employed in [15] to segment 3D IVUS data. Vertical intensity pattern along the borders, Rayleigh distribution and Chan-Vese minimum variance criterion are used in designing the cost functions. These intensity-based features are susceptible to image variations that commonly exist in IVUS, such as calcification and acoustic shadow.

One of the limitations of the conventional Graph cut [29, 7] is its reliance on user interaction to infer the unary cost for each pixel, which can be time consuming and impractical with a large image size and/or a large number of images. In addition, the definition of smoothness cost is mainly derived from edge features which becomes less useful in the blank region of the image. Li *et al.* [8] proposed a terrain-like multiple surfaces segmentation method by constructing a weighted directed graph that allows imposing some geometrical constraints to define the elasticity of each surface and the inter-relation with other surfaces, and to search for the minimum closed, subgraph set containing the surface on its envelope by utilising the  $s-t$  cut

method to minimise the cost function and without the need for user intervention. This method is well suited to IVUS/OCT segmentation, however dealing with image artifacts, defining the optimal cost function, and adapting the graph construction are the major challenges.

In this chapter, a bottom-up data-driven approach is presented to segment IVUS and OCT images. For IVUS segmentation, a double-interface graph cut segmentation is proposed to delineate the media-adventitia border, in order to achieve reliable results automatically. The impediments, such as stents or fibrotic and calcium plaque, appear inside the media-adventitia border, and the acoustic signal decays rapidly in the adventitia so that there are largely no strong features beyond the media-adventitia border. This observation inspired us to apply an additional interface searching inside the media-adventitia border which links those undesired image features, including partial lumen border, and hence preserves the border of interest. A combination of complementary texture features is used to form the basis of the boundary-based cost functions. For OCT segmentation, a single-interface graph cut segmentation is proposed to delineate the lumen border. Moreover, a novel image feature is incorporated into the cost function, instead of merely using image intensity or the local gradient magnitude. The image feature is derived from the gradient vector interaction across the image domain and possesses the characteristics of regional features.

## 3.2 Preprocessing

The preprocessing serves to transform images from Cartesian coordinates to polar coordinates and to remove the catheter region from the transformed images. Representing the images in polar coordinates is important to facilitate feature extraction in terms of radial and tangential characteristics. It also facilitates the automated graph cut in searching for minimum closed sets, where an open-ended height field is preferred. Moreover, the post-processing can then be carried out more efficiently since it becomes a one-dimensional interpolation instead of two-dimensional.

The catheter generates a blank region which contains no information and is surrounded by a ring-down artifact which may hamper the search process for finding the minimum cost path for the desired border. The ring-down artifact is located in the first rows of the transformed image, and it is approximately a constant. Therefore, a simple thresholding method is used to remove that region as shown in Figure 3.1c.

### 3.3 Feature Extraction

In IVUS imaging, the media layer consists largely of homogeneous smooth muscle, which exhibits as a dark layer in ultrasound images, and the adventitia layer tends to be brighter, see Figure 3.1 as an example. Hence, edge-based features are appropriate to extract the media-adventitia border. In OCT imaging, the lumen appears to be much darker because blood is flushed out before imaging. The intima and other tissues, including plaque, surrounding the lumen have a bright appearance. Hence, the lumen-intima border has a good contrast, i.e., image gradient features may be adopted to highlight the border. However, a guide-wire artifact and other interfering image features commonly exist inside the artery and they cast shadows over the border of interest, disrupting its continuity. Those imaging artifacts generally have large responses to image gradient based feature extraction.

#### 3.3.1 Steerable filter

A steerable filter is a linear combination of differently oriented instances of the base filter. A set of  $n$  order derivatives of Gaussian (GD) filters  $G_n(x, y)$  in different orientations can be used to highlight the edge features along the border. The steerable filters can be defined as a linear combination of a set of derivatives of Gaussian [72]:

$$G_n^\theta(x, y) = \sum_{j=1}^M k_j(\theta) G_n^{\theta_j}(x, y), \quad (3.1)$$

where  $G_n^\theta(x, y)$  is the rotated version of  $G_n(x, y)$  at  $\theta$  orientation and  $k_j(\theta), 1 \leq j \leq M$  are interpolation functions.

Steering derivatives in the direction of the gradient make them invariant to rotation. These steerable filters are more effective in highlighting oriented structure, e.g., edges, than isotropic band-pass filters, particularly when there is noise interference [72].

#### 3.3.2 Log Gabor filter

The Gabor filter acts as a bandpass filter that has been used in texture analysis to exploit its similarity with the human visual system [259, 260] and performs multi-channel, frequency and orientation analysis on the visual image. Gabor filter can achieve optimal joint localisation in the spatial and frequency domains. The Gabor filters have two components: a real part and an imaginary part, where the Gabor function is a multiplication of a Gaussian function and a

complex sinusoid function in the spatial domain, corresponding to a Gaussian shift from the centre of frequency in the Fourier domain. Here, the Log-Gabor filter [261] is used in different scales to enhance the border and to reduce speckles and other image artifacts. The Log-Gabor function,  $LG(f)$ , has a frequency response defined as a symmetric Gaussian on a log frequency axis:

$$LG(f) = \exp\left(-\frac{[\log(f/f_0)]^2}{2[\log(\sigma/f_0)]^2}\right), \quad (3.2)$$

where  $f_0$  is the centre frequency of the filter, and  $\sigma$  is the filter bandwidth. The Log-Gabor function has no DC component for any bandwidth filter compared to the Gabor function.

### 3.3.3 Local phase

Local phase features have been shown to be an effective alternative to intensity derived features to deal with inhomogeneity, low image quality, and imaging shadow which are common in IVUS and OCT images. For example, in [262] local phase features were used to highlight acoustic boundaries in echocardiographic images.

Local phase features are considered as extrema in Fourier phase components, which can be located as peaks in the local energy function obtained by convolving odd and even symmetric Log Gabor filters,  $(o_m(x, y), e_m(x, y))$ , to remove the DC component and preserve the phase in a localised frequency. Two types of features can be extracted from phase congruency: feature asymmetry and feature symmetry. Feature symmetry favours bar-like image patterns and exists in the frequency components at either the minimum or maximum symmetric points in their cycles, which is useful in extracting the thin media layer in IVUS. Its dark polarity symmetry is used here [263]:

$$\phi_s(x, y) = \max_{\theta} \frac{\sum_m [ [-e_m(x, y) - |o_m(x, y)|] - T_m ]}{\sum_m A_m(x, y) + \varepsilon}, \quad (3.3)$$

where  $\theta$  and  $m$  denote filter orientation and scale,  $\varepsilon$  is a small constant,  $T_m$  is an orientation-dependent noise threshold,  $A_m(x, y) = \sqrt{e_m^2(x, y) + o_m^2(x, y)}$  and  $[\cdot]$  denotes zeroing negative values. In contrast, feature asymmetry highlights step-like image patterns and corresponds to the point where all the frequency components are at the most asymmetric points in their cycles. It can be defined as:

$$\phi_a(x, y) = \max_{\theta} \frac{\sum_m [ [|o_m(x, y)| - |e_m(x, y)|] - T_m ]}{\sum_m A_m(x, y) + \varepsilon}. \quad (3.4)$$

Phase asymmetry is useful to highlight the lumen border in OCT, where edge features can be seen from darker lumen layer to brighter intima layer.

#### 3.3.4 Circulation density features

In graph cut, the cost function can be generally categorised as edge based and region based. Edge-based cost functions assume that the object boundary is largely collocated with image intensity discontinuity, and typically use derivatives of the image intensity function as a local estimation of likelihood of an object boundary. Region-based ones are usually non-edge based, e.g., piecewise constant assumption. Quite often, image intensity values are directly used in general image segmentation. Although graph cut algorithms provide global optimality in two-level segmentation, a reliable but also generic image feature that does not assume strong image prior is desirable for general segmentation that is useful for, for instance, object recognition.

We consider intensity discontinuity is perhaps the least constrained and most widely applicable object boundary estimation. Its performance can be easily compromised by image noise, smooth varying intensity at object boundary, and so on. These shortcomings are essentially because it is a local measurement and it does not take into account interactions among image gradient vectors. As an example, a region with relatively a large image gradient magnitude by varying gradient directions suggests that it is unlikely a location of object boundary, despite their large magnitude. On the contrary, weak gradient vectors that are aligned with each other suggest a greater likelihood of object boundary than what the magnitude itself suggests.

Hence, we present a gradient vector field that is a result of global interactions among original image gradient vectors, in which its circulation density can be used as a reliable image feature for graph cut. The zero-crossings of this circulation density provide a better indication of the location of object boundary, and the magnitude of oscillation at zero-crossings indicates the strength of object boundary presence. The signs (positive and negative) of circulation density actually indicate the foreground and background. The derived gradient vector can also be diffused to produce a more coherent circulation density. The image feature is directly derived from edge-based assumption, but closely resembles region-based methods.

Let  $\nabla_i I = f\hat{I}_x$  and  $\nabla_j I = f\hat{I}_y$  denote the two components of the image gradient  $\nabla I$  in the image coordinates  $(i, j)$ , respectively, i.e.,  $\nabla I = (\nabla_i I, \nabla_j I)^T$  where  $f$  is the edge map (magnitude). A convolution computation is carried out on both components with the kernel  $k(\mathbf{x}) = m(\mathbf{x})$ .

Moreover, the magnitude function  $m$  is chosen as an inverse of distance from the origin, i.e.,  $m(r) = 1/r^\zeta$ . Thus, the result of this convolution process can be expressed as:

$$\begin{cases} G_i(\mathbf{x}) = \nabla_i I * k(\mathbf{x}) = \sum_{\mathbf{s} \neq \mathbf{x}} \frac{\nabla_i I(\mathbf{s})}{R_{\mathbf{x}\mathbf{s}}} = \sum_{\mathbf{s} \neq \mathbf{x}} f(\mathbf{s}) \frac{\hat{I}_i(\mathbf{s})}{R_{\mathbf{x}\mathbf{s}}}, \\ G_j(\mathbf{x}) = \nabla_j I * k(\mathbf{x}) = \sum_{\mathbf{s} \neq \mathbf{x}} \frac{\nabla_j I(\mathbf{s})}{R_{\mathbf{x}\mathbf{s}}} = \sum_{\mathbf{s} \neq \mathbf{x}} f(\mathbf{s}) \frac{\hat{I}_j(\mathbf{s})}{R_{\mathbf{x}\mathbf{s}}}, \end{cases} \quad (3.5)$$

where  $R_{\mathbf{x}\mathbf{s}}$  is the distance between  $\mathbf{x}$  and  $\mathbf{s}$ , and  $\mathbf{G} = (G_i, G_j)$  denotes the resultant gradient convolution field. Due to the smoothing effect when applying the kernel function, the original image gradient vectors have extended their influence from the immediate vicinity of edge pixels to a much larger neighbourhood. In fact, the computation in (3.5) is across the whole image domain.

The circulation density of this extended gradient vector field is then computed as:

$$B = \nabla \cdot \mathbf{G}(\mathbf{x}) = \nabla \cdot (G_i, G_j) = \nabla \times (-G_j, G_i), \quad (3.6)$$

where  $\nabla \cdot$  is the divergence operator, and  $\nabla \times$  is the curl operator. This circulation density has an intrinsic link to the magnetic field used in the MAC model [168] in a variational framework. Specifically, when  $\zeta = 1$ ,  $B$  is equivalent to the third and the only effective component of the magnetic field in the MAC model. Hence, the positive and negative values of this circulation density indicate foreground/background or background/foreground. The zero crossings of the vector circulation density would indicate the location of object boundaries. Obviously, this proposed circulation density method is a generalisation of the effective component used in MAC. Moreover, we can refine the computation of this vector circulation density by performing efficient Laplacian diffusion in the extended gradient vector field to overcome, for instance, noise interference.

Note that the gradient vector field is actually along the edge direction so substantial diffusion in the components can result in significantly improved boundary description. There are various diffusion strategies for this smoothing task. For implementation convenience and less parameter intervention, an isotropic/Laplacian diffusion scheme is used here, which is carried out by solving the following Euler equations:

$$\begin{cases} \frac{\partial}{\partial t} \mathcal{G}_i(\mathbf{t}, \mathbf{x}) = p(G_i) \nabla^2 \mathcal{G}_i(\mathbf{t}, \mathbf{x}) - q(G_i)(\mathcal{G}_i(\mathbf{t}, \mathbf{x}) - G_i), \\ \frac{\partial}{\partial t} \mathcal{G}_j(\mathbf{t}, \mathbf{x}) = p(G_j) \nabla^2 \mathcal{G}_j(\mathbf{t}, \mathbf{x}) - q(G_j)(\mathcal{G}_j(\mathbf{t}, \mathbf{x}) - G_j), \end{cases} \quad (3.7)$$

where  $\nabla^2$  is the Laplacian operator,  $\mathcal{G}_i(0, \mathbf{x}) = G_i(\mathbf{x})$ ,  $\mathcal{G}_j(0, \mathbf{x}) = G_j(\mathbf{x})$ , and  $p(y)$  and  $q(y)$  are weighting functions allowing very little smoothing at strong edges and varying smoothing elsewhere. It is given as:

$$p(y) = \exp(-|y|f/K), q(y) = 1 - p(y), \quad (3.8)$$

where  $f = |\nabla I|$  and  $K$  is a constant. The first term on the right side of equation 3.7 is the smoothness term which creates a smoothly varying vector field, while the second term is the data term that encourages the vector field  $\mathcal{G}$  to be closed to the gradient of edge map in  $\mathbf{G}$ .

## 3.4 Single and Double Interface Segmentation

Briefly, a node-weighted directed graph is constructed so that the border extraction is considered as computing a minimum closed set. The search for this minimum closed set is solved by computing a minimum  $s$ - $t$  cut in a derived arc-weighted directed graph. For the double-interface segmentation, an additional set of arcs is constructed, taking into account the topological interrelation between the two interfaces. The associated cost functions for each image modalities are defined based on extracted image features. Finally, the desired border, located on the envelope of the minimum closed graph, is smoothed using radial basis function (RBF) interpolation.

### 3.4.1 Graph construction

Conventional graph cut, such as [7], generally requires user initialisation, and more importantly only deals with one interface, i.e., foreground and background separation. Alternative methods, such as active contour and level set techniques, e.g., [264], can track multiple interfaces. However, they often require user initialisation and do not guarantee a global minimum. Furthermore, since one of the interfaces is attracted by image features, such as calcification, which varies from image to image, it does not have consistent shape characteristics. Hence, a deformable model with multiple interfaces, such as [265], may not be suitable.

In [8], the authors proposed a novel graph construction method, which transforms the surface segmentation in 3D into computing a minimum closed set in a directed graph. We adapt this method to a 2D segmentation, which can carry out double-interface segmentation simultaneously in low order polynomial time complexity and does not require user initialisation. This

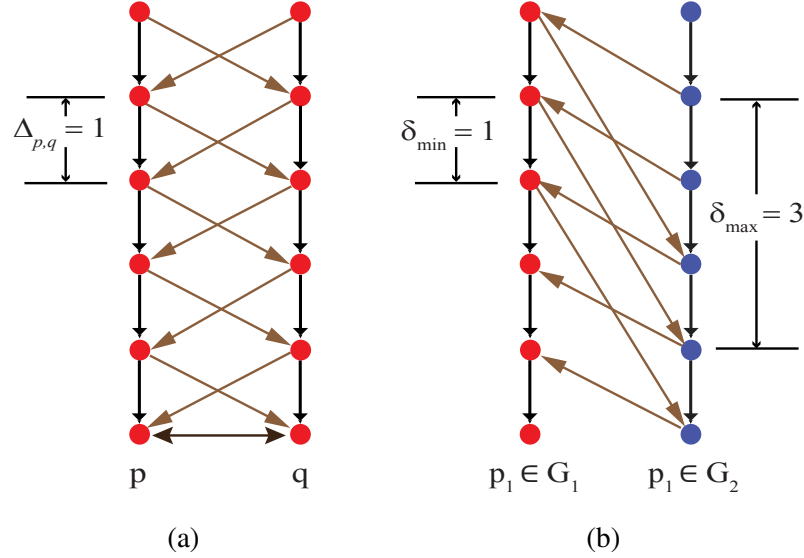


Figure 3.2: Graph construction. (a) intra-column and inter-column arcs when  $\Delta_{p,q} = 1$ . (b) inter-interface constraints when  $\delta_{min} = 1$  and  $\delta_{max} = 3$ .

approach also allows us to impose topological constraint, i.e., the two interfaces in our case can not intersect or overlap and the media-adventitia border is the outer interface (or lower interface when the IVUS image is transformed to polar coordinates).

For each desired interface, construct a graph  $G = \langle V, E \rangle$ , where each node  $V(x, y)$ ,  $0 \leq x < X$  and  $0 \leq y < Y$ , corresponds to a pixel in 2D image  $I(x, y)$  with size  $X \times Y$ . The graph  $G$  consists of two arc types: intra-column arcs and inter-column arcs see Figure 3.2. For intra-column, along each column, every node  $V(x, y)$  where  $y > 0$  has a directed arc with  $+\infty$  weight to the node  $V(x, y - 1)$ . In the case of inter-column, for each node  $V(x, y)$  a directed arc with  $+\infty$  weight is established to link with node  $V(x + 1, y')$ , where  $y' = y - \Delta_{p,q}$ , and  $y \geq \Delta_{p,q}$ . Similarly, node  $V(x + 1, y)$  is connected to  $V(x, y')$ , where  $\Delta_{p,q}$  controls the maximum distance allowed to change between two neighbouring columns  $p, q$  in the  $y$ -coordinate of the interface  $|y - y'| \leq \Delta_{p,q}$ .

Since the vessel has a cylindrical-like shape, the first and last columns in the polar transformed images are closely connected. Thus, inter-column arcs are added between them in which each node  $V(0, y)$  (and also  $V(X - 1, y)$ ) is connected to  $V(X - 1, y')$  (and  $V(0, y')$  respectively). The nodes in the last row of the graph are connected to each other with  $+\infty$  weight to maintain a closed graph.

### 3. Graph Cut Segmentation: A Bottom-Up Approach

---

For double-interface segmentation and after constructing the graph for each of the two interfaces to simultaneously segment them, taking into account interrelations between them is necessary and this is achieved by setting up another set of arcs to connect them as shown in Fig 3.2b. Geometrical and topological constraints can be imposed by setting minimum  $\delta_{min}$  and maximum  $\delta_{max}$  separation distances. The two interfaces thus will not intersect or overlap. This set of arcs,  $\mathcal{E}^s$ , is defined as:

$$\mathcal{E}^s = \begin{cases} \{V_1(x, y), V_2(x, y - \delta_{max}) | y \geq \delta_{max}\} \cup \\ \{V_2(x, y), V_1(x, y + \delta_{min}) | y < Y - \delta_{min}\} \cup \\ \{V_1(0, \delta_{min}), V_2(0, 0)\} \end{cases} \quad (3.9)$$

This graph construction requires the desired interfaces to be open-ended height fields, which in this case means that this will be carried out in polar coordinates.

#### 3.4.2 Cost function

The cost function is defined on the image domain, in which it is inversely proportional with the likelihood of each pixel belonging to the desired border. The cost function can be expressed as  $E = \sum_{V \in S} \hat{C}(x, y)$ , where  $\hat{C}$  denotes the normalised cost function ( $\hat{C}(x, y) \in [0, 1]$ ) and  $S$  is a path in the directed graph. The formulation of the pre-normalisation cost function,  $C$ , is determined as presented below.

##### 3.4.2.1 IVUS

Due to large variations in image features and the correlation between edge information and media-adventitia border, boundary-based cost functions are used. The cost function indicates the likelihood of each node in the graph belonging to the minimum cost path that represents the desired interface. Two separate cost functions are used to capture the media-adventitia border and an auxiliary interface that is above the media-adventitia, since these two interfaces have different characteristics in image feature and formation.

For the media-adventitia border, three types of features described in Sect. 3.3 are used. It takes the following form:

$$C_1(x, y) = C_d(x, y) + \alpha_1 C_G(x, y) + \alpha_2 (1 - \phi_s(x, y)), \quad (3.10)$$

where  $C_d$  denotes the term for derivative of Gaussian features,  $C_G$  is for log-Gabor, and  $\alpha_1$  and  $\alpha_2$  are constants. The derivatives of Gaussian responses from six different orientations are summed together to form  $C_d$ . Similarly,  $C_G$  can be obtained by cascading the filtering responses across scales. In addition, more weight can be assigned to coarser scale features so that it presents the connectivity of the media-adventitia border at the existence of acoustic shadow, e.g.,  $C_G = G^{(3)} + G^{(4)} + 1.5G^{(5)}$  as used here and  $G^{(i)}$  denotes  $i$ th scale. Feature symmetry  $\phi_s$  is useful in enhancing the thin layer of media. It is normalised beforehand, and since the middle of the layer has larger values  $1 - \phi_s$  is used in the cost function so that the interface between media and adventitia is highlighted. Note that each of the term in the cost function is normalised.

For the auxiliary interface that is above media-adventitia, we use a combination of the log-Gabor feature and feature asymmetry:

$$C_2(x, y) = C_G(x, y) + \alpha_3 (1 - \phi_a(x, y)), \quad (3.11)$$

where  $\alpha_3$  is a constant. Since the derivative of Gaussian filter has a relatively stronger response to local intensity variation, it is not included in this cost function. The combination of those two types of features leads the cost function to favour linking globally dominant image features, which very often is distractive for media-adventitia border segmentation.

### 3.4.2.2 OCT

The zero-crossings of the circulation density feature computed from gradient vector interaction indicate the location of the object boundary. The degree of circulation density oscillation at the zero-crossing suggests the strength of the object boundary. A direct assignment of circulation density to the graph as a nodal cost would be inappropriate, since the minimum or maximum of the circulation density is not an indication of either location or strength of the object boundary. However, a simple transformation, for instance computing its gradient magnitude, can be applied. Since the decay of circulation density from the object boundary is exponential, a log transformation can be added in order to avoid extreme values to be assigned to the graph, i.e.  $C = -\log|\nabla B|$ .

### 3.4.3 Compute the minimum closed set

Each graph node is weighted by a value  $w(x,y)$  representing its rank to be selected in the minimum closed set graph where the arc costs between graph nodes are infinitive. The weight assignment is carried out according to:

$$w(x,y) = \begin{cases} C(x,y) & \text{if } y = 0, \\ C(x,y) - C(x,y-1) & \text{otherwise.} \end{cases} \quad (3.12)$$

where  $C$  denotes any cost function. For a feasible path  $\mathcal{S}$  in the graph, the subset of nodes on or below  $\mathcal{S}$  form a closed set and it can be shown that the cost of the  $s$ - $t$  cut in the graph is equivalent to the cost of nodes in the corresponding subset differ by a constant [8]. Hence, segmenting the border of interest is equivalent to finding the minimum closed set in the directed graph. The  $s$ - $t$  cut algorithm proposed by Boykov and Kolmogorov [114] is used to find the minimum closed set, based on the fact that the weight can be used as the base for dividing the nodes into nonnegative and negative sets. The source  $s$  is connected to each negative node and every nonnegative node is connected to the sink  $t$ , both through a directed arc that carries the absolute value of the cost node itself. The optimal interfaces correspond to the upper envelope of each minimum closed set graph as shown in Figure 3.3. Since the graph has  $O(kn)$  nodes and  $O(km)$  edges, where  $k$  is an integer constant that represents the number of interfaces  $1 \leq k \leq 2$ , the minimum closed set can be computed in  $T(kn, km)$  time that depends on the choice of the  $s$ - $t$  cut algorithm as discussed in Chapter 2.

### 3.4.4 Post-processing

The smoothing parameter in graph construction prevents sudden drastic changes in the extracted interfaces. However, the segmented interface may still contain local oscillations. Smoothing based post-processing can be adopted to eliminate such oscillations. Here, RBF interpolation using a thin plate base function is used to effectively obtain the final interface. Note, due to that fact that the images have been transformed into polar coordinates, the RBF processing only needs to be carried out in 1D. Figure 3.3c shows the media-adventitia border after applying the RBF smoothness.

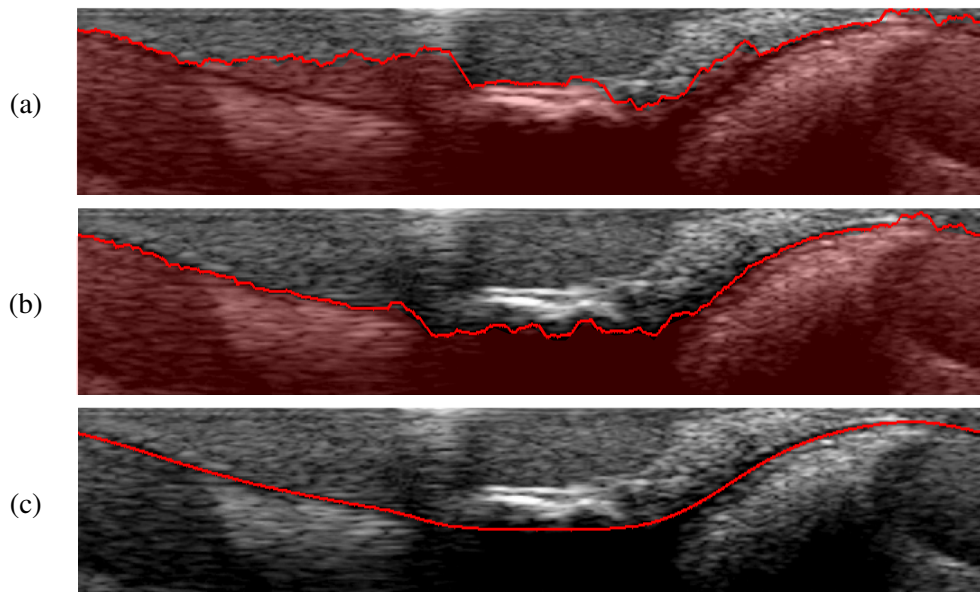


Figure 3.3: The minimum closed set graph highlighted by red colour for, (a) the auxiliary interface, and (b) the media-adventitia border. (c) The media-adventitia border after the RBF smoothness.

### 3.5 Results: IVUS

The IVUS images are acquired using a 40 MHz transducer Boston Scientific ultrasound machine with Atlantis SR Pro Catheter. These images contain various forms of soft and fibrous plaque, calcification, stents, and acoustic shadow. In most of the images, the blood speckle is so prominent that the lumen border is very difficult to see. For all the tested images, ground-truth via manual labelling is available for quantitative analysis. The ground-truth was prepared at the beginning time of the project and validated by two clinical consultants. All the parameters are fixed: the minimum and maximum distance between two interfaces,  $\delta_{min}$  and  $\delta_{max}$ , are set to be 5 and 140 respectively, and cost function weightings are set as  $\alpha_1 = 0.7$ ,  $\alpha_2 = 0.5$ , and  $\alpha_3 = 0.5$ .

#### Single interface segmentation

A single graph is constructed where the value of  $\Delta_{p,q}$  is set as a global constant for each pair of neighbouring columns  $p, q$  to act as a hard constraint that prevents drastic changes in the border shape. Figure 3.4 shows the effect of the hard geometric constraints  $\Delta_{p,q}$  to produce

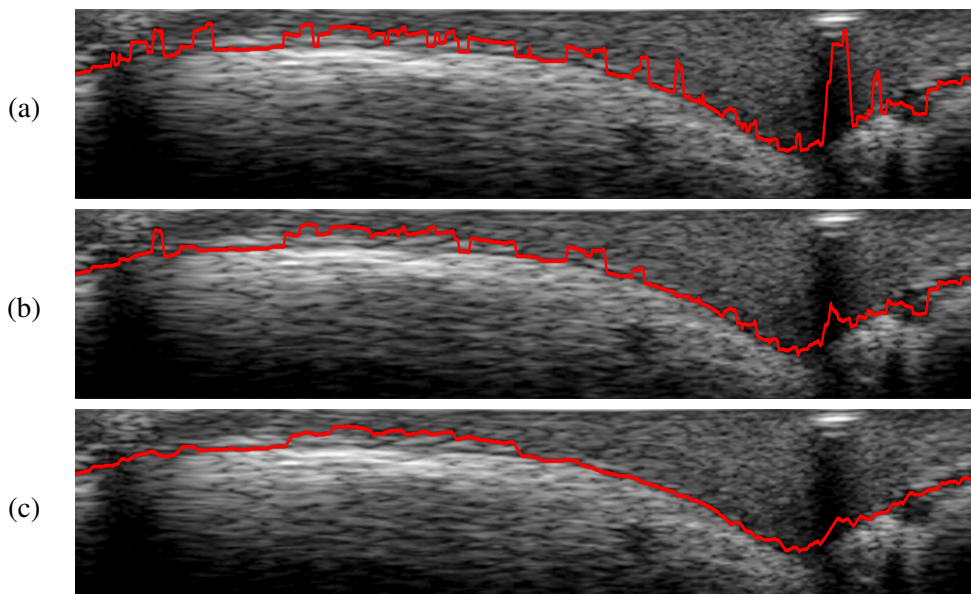


Figure 3.4: The effect of  $\Delta_{p,q}$  constraints on single interface segmentation. These hard constraints globally set to 10, 5, and 1 pixel distance shown in a, b and c rows respectively.

more reasonable results. The cost function is based on the three types of features as defined in equation (3.10). Calcification, stents or any highly bright patterns in fibrous tissue have strong edge features compared to the surrounding regions and that is the main reason of the jumbled result of single interface segmentation to highlight the media-adventitia border, as shown in Figure 3.5 (c) and Figure 3.6 (b). However, the single interface segmentation can work properly in ideal images when the artefact that distorted the IVUS image is less as shown in the first row of Figure 3.7.

### Double interface segmentation

The proposed method was compared against the  $s-t$  cut [7] and single-interface segmentation with the cost function in equation (3.10). The cost function for the media-adventitia was kept the same. The  $s-t$  cut method requires manual initialisation, and its result is highly initialisation dependent. Figure 3.5 (a)-(b) shows a typical result achieved using  $s-t$  cut. Even with reasonable care in initialisation, the result was not satisfactory. The single-interface segmentation gives a partial media-adventitia border, as shown in row (c). However, its performance degraded when there were interfering image structures. The proposed double-interface method achieved better results even without any user interaction, as seen in row (d). More compara-

Table 3.1: Comparison between  $s-t$  cut, single-interface and double-interface segmentation results. AD: area difference in percentage; AMD: absolute mean difference in pixel compared to ground-truth.

|      | $s-t$ cut |       | Single interface |       | Double-interface |      |
|------|-----------|-------|------------------|-------|------------------|------|
|      | AD        | AMD   | AD               | AMD   | AD               | AMD  |
| Mean | 21.24     | 22.61 | 9.99             | 12.55 | 5.84             | 6.99 |

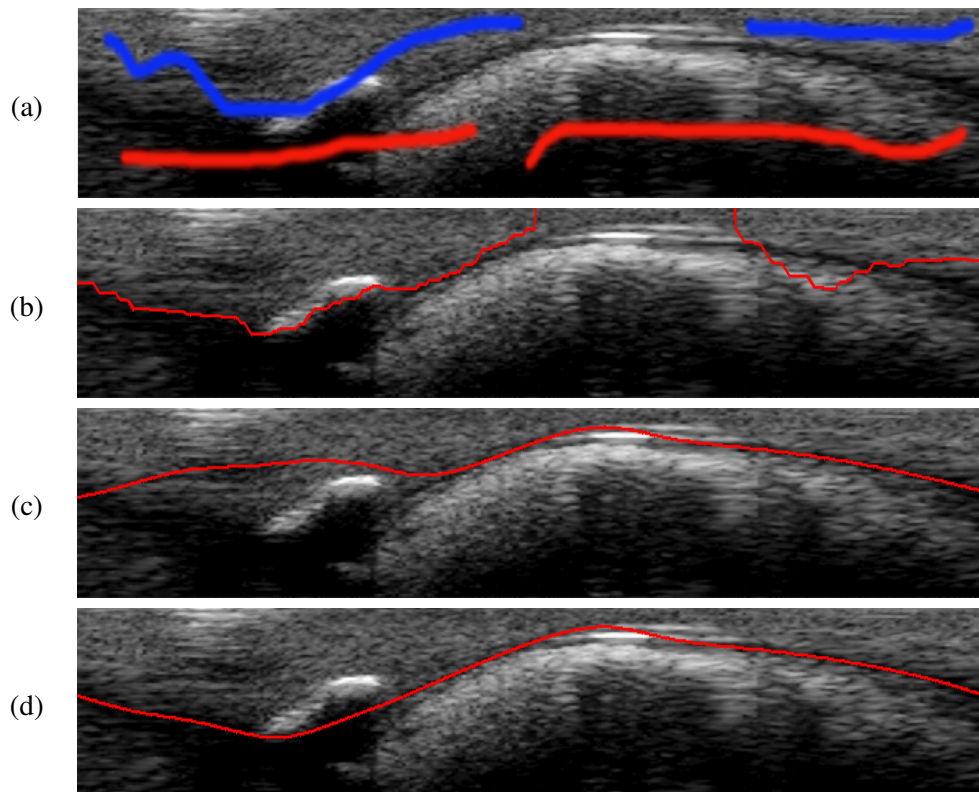


Figure 3.5: (a): initialisation for  $s-t$  cut, and its result shown in (b); (c): result by single interface segmentation; (d): proposed double-interface method.

tive results are given in Figure 3.6, which shows typical performance for each method. Table 3.1 provides the quantitative comparison between the  $s-t$  cut, the single-interface approach and the proposed method and was carried out on a randomly selected subset of 95 images, since manual initialisation is too labour intensive. The proposed method achieved better accuracy and consistency. A qualitative comparison between manual labelling of the media-adventitia border and the proposed method is shown in Figure 3.7.

3. Graph Cut Segmentation: A Bottom-Up Approach

---

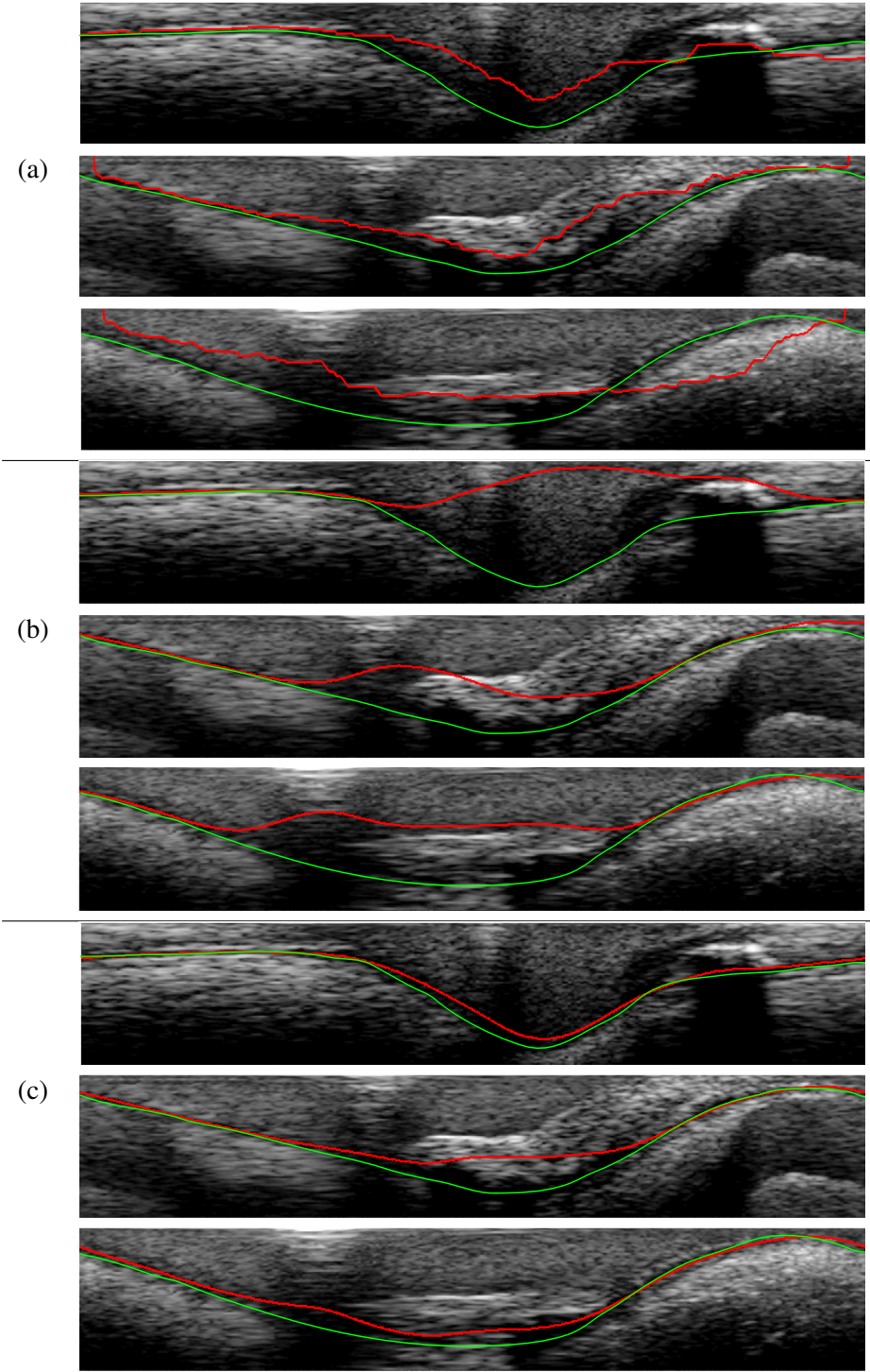


Figure 3.6: Comparison between ground-truth (green) and segmentation results (red): (a)  $s-t$  graph cut result. (b) Single-interface result. (c) Double-interface result.

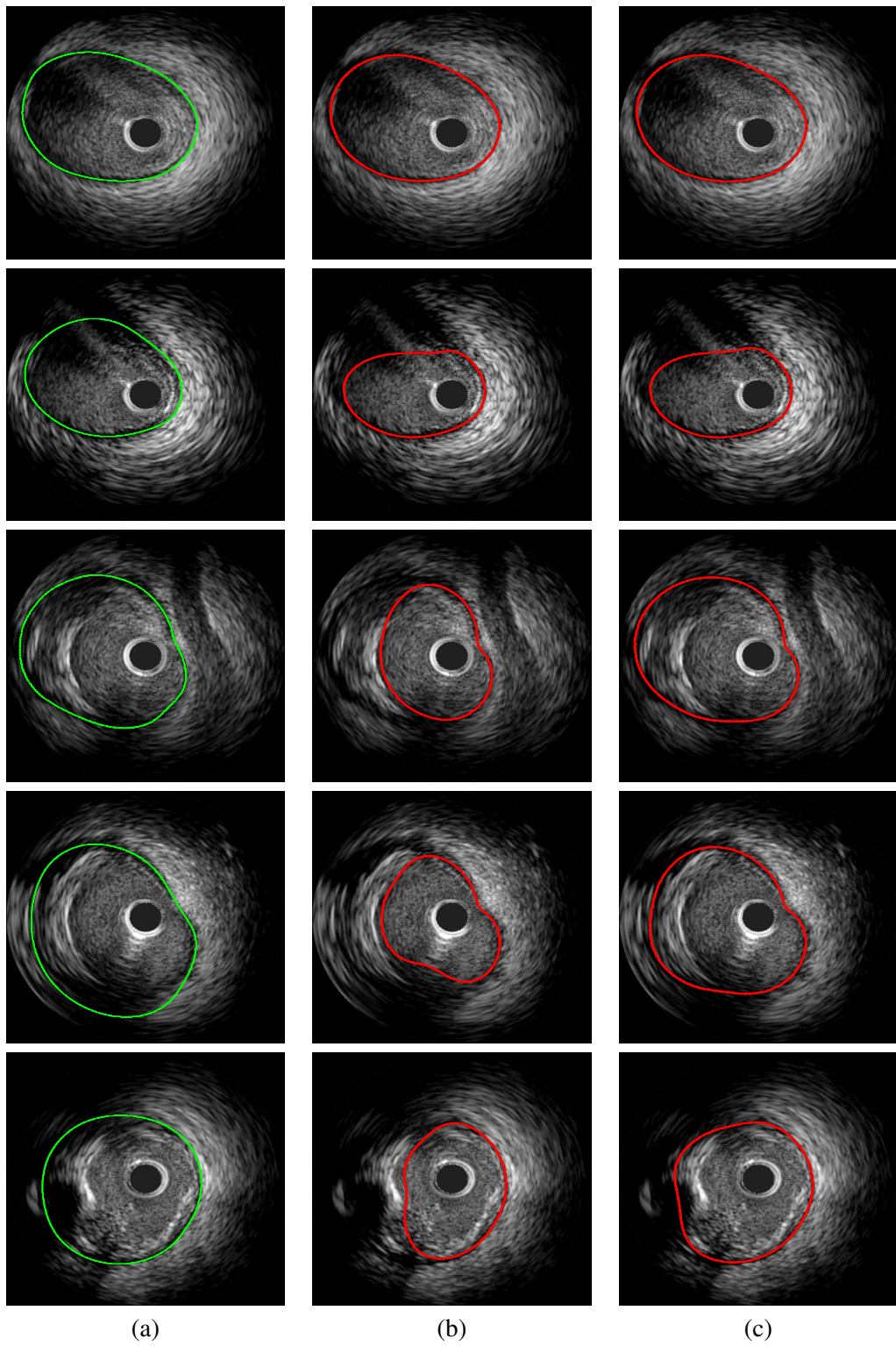


Figure 3.7: (a) Ground-truth. (b) Single-interface. (c) Double-interface.

Table 3.2: Quantitative results with 2283 images for star graph cut [1] and the proposed method. AMD: Absolute Mean Difference(pixel); HD: Hausdorff Distance(pixel); AO: Area Overlap(%); Sens.: Sensitivity(%); Spec.: Specificity(%).

|                    | AMD         | HD           | AO           | Sens.        | Spec.        |
|--------------------|-------------|--------------|--------------|--------------|--------------|
| Star Graph cut [1] | 5.85        | 22.11        | 91.27        | <b>96.52</b> | 98.07        |
| Proposed method    | <b>4.94</b> | <b>19.09</b> | <b>92.51</b> | 96.03        | <b>98.85</b> |

### 3.6 Results: OCT

In our study, for validating the performance of the proposed method in the vessel lumen border detection, ten OCT *in vivo* scans of the human artery were acquired with a Frequency Domain OCT Imaging System (C7-XR, LightLab). Among these images used, there are various forms of fibrous plaque, calcification, stents, and bifurcation which are created from the acquisition process. To establish the groundtruth, the ten pullbacks, i.e., 2283 images in total, are manually labelled to identify the lumen area. By contrast, four recently developed methods are employed to demonstrate the performance of the proposed method. These include the star graph cut [1], VFC [3], the modified Chan-Vese model [156, 2] and DRLSE [4]. Among these methods, Zhang *et al.* [2] proposed a region-based signed pressure force that combines Chan-Vese model and geodesic active contour model and utilises a Gaussian filter to avoid re-initialisation of the signed distance function of the generated level set; DRLSE is a typical edge-based method without the need for level set reinitialisation using a distance regularisation term; VFC is a derived active contour model with a proposed vector field convolution as a new external force; and the star graph cut incorporates a star shape prior into the graph cut formulation. In terms of graph-based technique and shape prior integration, the proposed method is most similar to the star graph cut in principle. The proposed method is compared to the star graph cut quantitatively and qualitatively with the full acquired data of 2283 images. For other methods used in comparison, they are all initialisation-dependency and thus we need to choose an appropriate iteration number for best results apart from a careful choice of an initialisation. With these considerations, we randomly select 226 images from the total 2283 images to show their performance dealing with the OCT segmentation.

In Figure 3.8, a set of six OCT images show the performance of both the star graph cut [1] and the proposed method. The results for the star graph cut and the proposed method are illustrated in Columns (c) and (d) respectively, while the original images and their ground-truth are listed

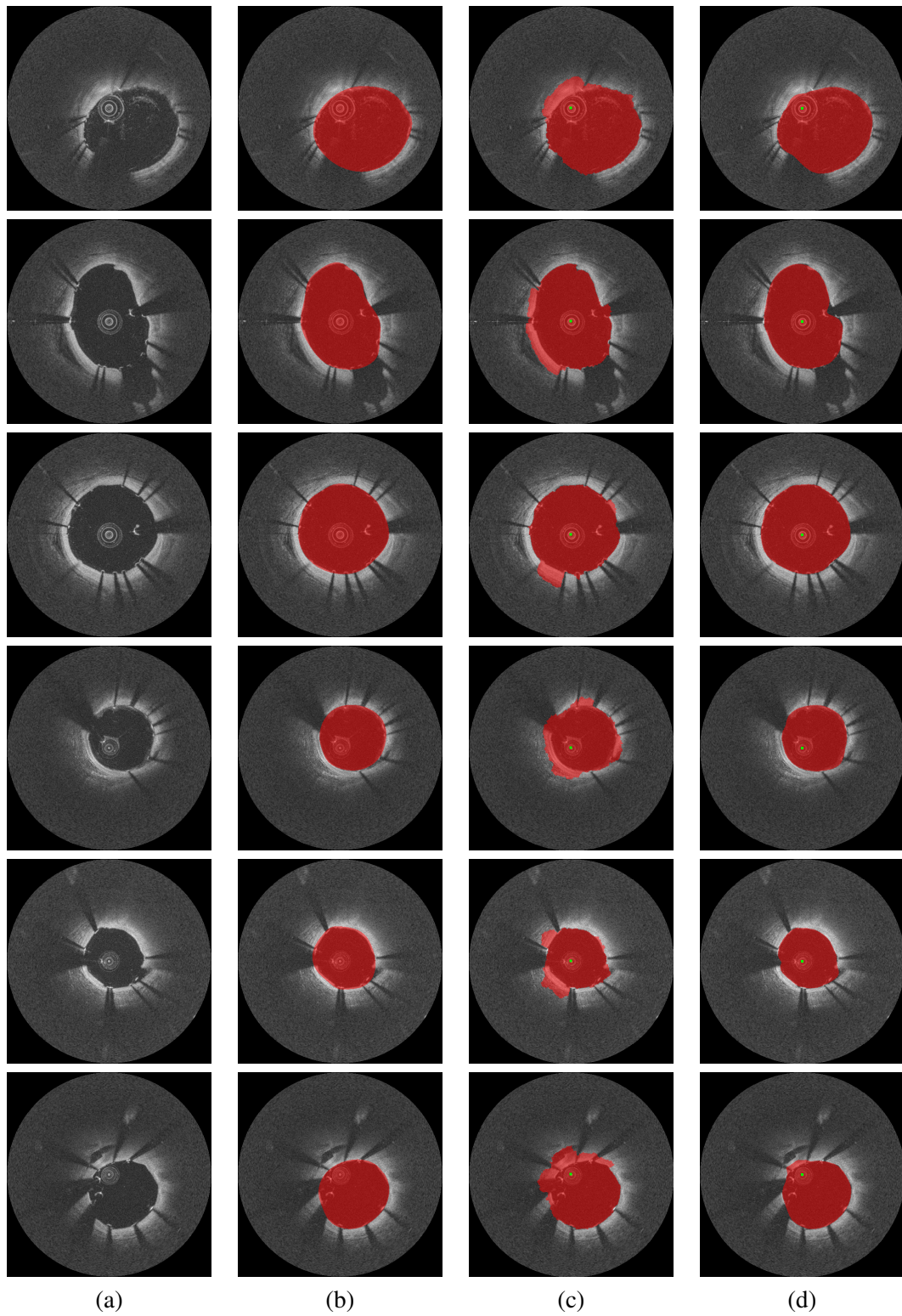


Figure 3.8: Comparison with star graph cut. (a) Original image. (b) Ground-truth. (c) Star graph cut. (d) Proposed Method.

### 3. Graph Cut Segmentation: A Bottom-Up Approach

---

in Columns (a) and (b). It is obviously shown that most of the cases in the star graph cut are over-segmented due to the use of “balloon” force. But, the proposed method generally performs quite well although the interference of various artifacts exists. However, the proposed method is still affected in some situations due to the adversities in the OCT modality. Several examples with inferior performance are presented in Figure 3.9. In Row 1, the results show that the serious bifurcation leads to the poor performance of the proposed method. In addition, the residual blood (shown in Row 2) and guide-wire artefact also cause the undermining in the border delineation as shown in Rows 3 and 4. Star graph cut performs better than the proposed method in some of these cases.

In order to comprehensively examine the performance of the proposed method, we use five performance metrics to quantitatively measure the accuracy of the segmentation on all images. These metrics include Absolute Mean Difference (AMD), Hausdorff Distance (HD), Area Overlap (AO), Sensitivity, and Specificity, which are defined as:

$$\begin{aligned}
 AMD &= \frac{1}{N} \sum_{i=1}^N |y_{AT}(i) - y_{GT}(i)|, \\
 HD &= \max_{a \in y_{AT}} \{ \max_{b \in y_{GT}} [dis(a, b)] \}, \\
 AO &= \frac{TP}{TP + FN + FP}, \\
 Sens. &= \frac{TP}{TP + FN}, \\
 Spec. &= \frac{TN}{TN + FP},
 \end{aligned} \tag{3.13}$$

where  $N$  is the number of border points,  $y_{AT}$  is the automatic border,  $y_{GT}$  is the groundtruth border,  $dis(a, b)$  is the Euclidean distance between  $a$  and  $b$  sets of points of the borders  $y_{AT}$  and  $y_{GT}$ ,  $TP$  is true positive area of the vessel,  $FN$  denotes false negative,  $FP$  denotes false positive, and  $TN$  is true negative. Note, the area that is within the vessel border is the positive area; outside is negative. The quantitative results are presented in Table 3.2. The proposed method is superior to the star graph cut in all metrics except for Sensitivity. It is understandable that the sensitivity of the star graph cut is a little bigger than ours because the star graph cut performs usually over-segmented.

To exhibit the superior performance of the proposed method over the deformable methods in capturing the lumen area of OCT images, Table 3.3 shows the quantitative results of three

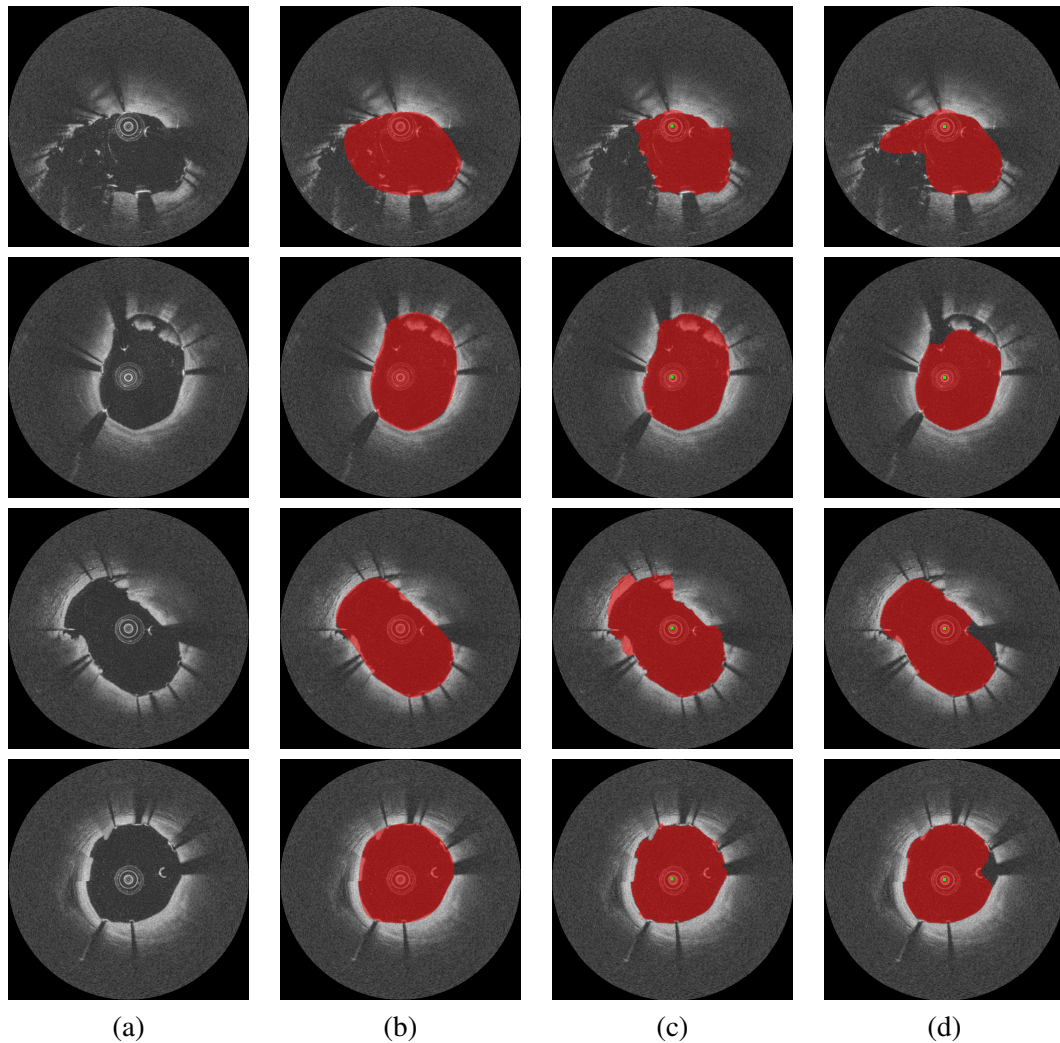


Figure 3.9: Cases with the inferior performance of the proposed method. (a) Original image. (b) Ground-truth. (c) Star graph cut. (d) Proposed method.

Table 3.3: Quantitative results with 226 images for the methods in [2], [3] and [4]. AMD: absolute mean difference(pixel); HD: Hausdorff distance(pixel); AO: area overlap(%); Sens.: sensitivity(%); Spec.: specificity(%).

|                        | AMD         | HD           | AO           | Sens.        | Spec.        |
|------------------------|-------------|--------------|--------------|--------------|--------------|
| Improved Chan-Vese [2] | 39.99       | 95.77        | 38.67        | 38.78        | <b>99.86</b> |
| VFC [3]                | 14.34       | 50.03        | 80.05        | 85.65        | 97.67        |
| DRLSE [4]              | 28.44       | 62.75        | 68.02        | 94.72        | 86.57        |
| Star Graph cut [1]     | 5.45        | 19.89        | 91.68        | <b>96.77</b> | 98.14        |
| Proposed               | <b>4.61</b> | <b>17.08</b> | <b>92.75</b> | 96.37        | 98.83        |

edge/region based methods along with the star graph cut and our method applied to 226 images. Due to being without the help of shape prior, the overall performance of these methods is very poor. In contrast, the proposed method outperforms these techniques significantly. In fact, the Chan-Vese method usually takes the advantage over the edge-based method because the region information can be extracted appropriately. However, it is incapable of dealing with the OCT segmentation where the induced artefact is very serious so that its AMD even reaches 39.99 and the AO is merely 38.67%. Among these methods, VFC performs reasonable in terms of the use of the vector field feature, whilst DRLSE cannot detect the lumen properly. In Figure 3.10, four examples are presented to illustrate the relevant issues in these methods. In Column (c), due to the nature of the Chan-Vese method, the lumen area is always segmented as the background while the bright area is detected. So, the method in [2] is impotent to deal with the OCT image. In contrast, VFC can perform well in some cases but it meets great difficulties in the situation of serious artifacts such as the last three cases. A quite similar performance happens to the method of DRLSE. However, its overall performance is poorer than VFC because it is sensitive to weak edge. It is worth noting that DRLSE and VFC can work well when the artefact interference is acceptable such as the first case Figure 3.10.

## 3.7 Summary

Single and double-interface segmentation methods for OCT and IVUS images were presented. The segmentation problem is defined here as the delineation of the media-adventitia border in IVUS and lumen-intima border in OCT. Images unravelled to polar coordinates which facilitate the removing of the catheter ring-down artifact and converting the segmentation problem into finding the minimum closed set graph that implies the border of interest. Steerable Gaussian derivative, Gabor and local phase features are extracted from images that utilise image intensity and texture information to highlight the desired border at different orientations and scales. A new image feature is introduced that is derived from global interactions of gradient vectors across the whole image domain. Laplacian diffusion is employed to refine image feature so as to produce more coherent segmentation.

For IVUS segmentation, an automatic double-interface segmentation method is proposed, whose cost functions combine local and global image features and its geometric constraint is integrated in graph construction. An auxiliary interface is simultaneously searched to prevent undesirable image features from interfering with the segmentation of the media-adventitia border.

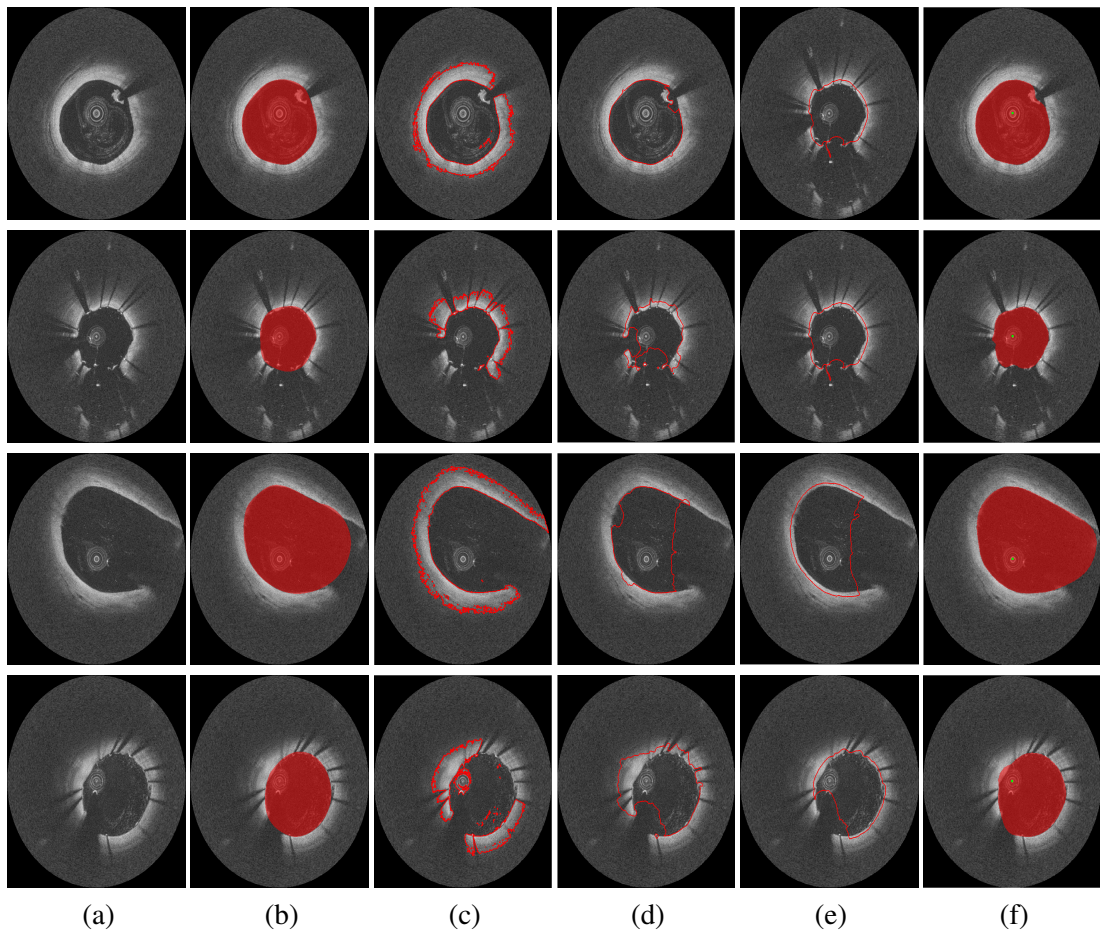


Figure 3.10: Results of the traditional methods in OCT. Column (a): Original image, Column (b): Ground-truth, Column (c): Improved Chan-Vese, Column (d): DRLSE, Column (e): VFC and Column (f): Proposed

Qualitative and quantitative comparison showed superior performance of the proposed method to the traditional graph cut method or single interface segmentation. For OCT segmentation, a single interface segmentation is proposed with a cost function defined at the zero-crossing of the circulation density of the gradient convolution field. Experimental results in OCT images demonstrate promising performances in comparison with the star graph cut method. It is also evident that the proposed method takes great advantages against the traditional edge/region-based deformable methods. However, the proposed method here needs a further improvement to reduce the artifact interferences.



## Chapter 4

# Segmentation with Shape Prior

### Contents

---

|     |  |    |
|-----|--|----|
| 4.1 | Introduction . . . . .                       | 63 |
| 4.2 | Tissue and Artifact Classification . . . . . | 66 |
| 4.3 | Cost Function Optimisation . . . . .         | 68 |
| 4.4 | Shape Prior Model . . . . .                  | 70 |
| 4.5 | Graph Cut . . . . .                          | 74 |
| 4.6 | Experimental Results . . . . .               | 75 |
| 4.7 | Summary . . . . .                            | 82 |

---

### 4.1 Introduction

In Chapter 3, IVUS imaging is segmented by a bottom-up approach in which an auxiliary border is used to tackle the distractions caused by stents and calcification and with the assumption the real media-adventitia border is beneath the auxiliary border in a simultaneous segmentation. The behaviour of the auxiliary border can be hard to predict, particularly when there is no such distractions.

In an attempt to overcome the shortcomings of imaging features, anatomical and imaging priors have been used to constrain the segmentation. Sonka *et al.* [14] requires the user to draw an elliptic shape to identify the region-of-interest (ROI) and uses parameterised prior knowledge on arterial wall thickness and double echo pattern in objective function to carry out segmentation. However, these hard constraints may not be valid in some cases, e.g., media thickness.

Learning and using appropriate priors are hence important. One approach is to adopt user interaction and directly impose prior knowledge through initialisation and/or user adjustment, e.g., [14, 149, 22, 1]. An alternative is to generalise priors and impose them as constraints in order to achieve automated segmentation. Unal *et al.* [33] used signed distance transform to implicitly represent prior shapes and applied principal component analysis (PCA) to generalise the shape variation. Its automated initialisation of the media-adventitia border, however, is based on the maximum gradient information which is susceptible to imaging artifacts. In [15], short vertical image segments are collected along media-adventitia borders to score image segments in unseen images based on the frequency of occurrence. Those score values are then used as the basis for data term in a cost function minimised using graph cut. The distribution of image segments however is not generalised, and its discrete form inevitably produces undesirable oscillations in score values.

Incorporating shape prior into graph-based segmentation attracted much attention in recent years, e.g., [266, 267, 268, 1]. In [266], a set of user-specified landmarks are used to define a shape template as a distance function and integrated with neighbouring edges in the graph to impose shape prior. Veksler [1] introduced a star shape prior to graph cut, also through user interaction. The user is required to specify the centre of ROI as the star point, and hence all boundary points of ROI lie on the radial spikes from the star point. Additional points, specifying foreground and background, are often necessary. A ballooning term is necessary to discourage the inherent bias in graph construction towards smaller size segmentation. Decomposition techniques, e.g., kernel PCA, have been used to generalise shape priors. In [267], graph cut is iteratively computed with the terminal edges updated according to PCA subspace projection of segmented shape from the previous iteration. However, user initialisation is generally necessary, as shown in [267], in order to impose shape constraint when computing the graph cut. In [268], non-parametric density estimation is used to generalise prior shapes. The terminal edges are iteratively updated according to the similarity between the current shape obtained through the graph cut and training shapes. Several graph cuts have to be computed before reaching the final result.

In this chapter, prior information is incorporated into the segmentation method to delineate anatomical borders in both IVUS and OCT without any user initialisation or interaction. The proposed prior model is not only to learn image artifacts in order to produce optimal cost function combination for image features but also to learn shape prior to impose global and local

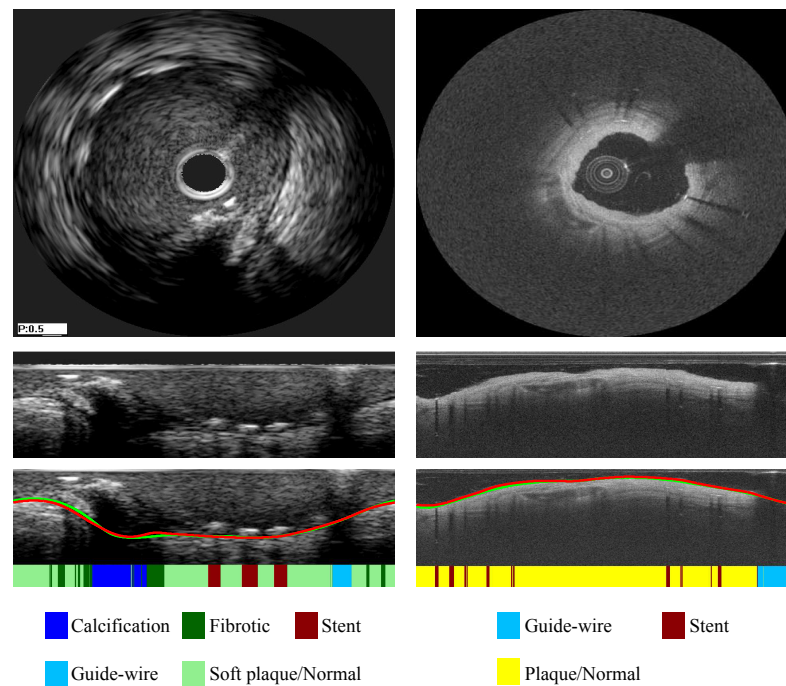


Figure 4.1: Example IVUS and OCT images. First row: original images. Second row: polar transformed images. Last row: segmented media-adventitia border in IVUS and lumen border in OCT using the proposed method (red); the groundtruth is shown in green. The bottom of each segmented image visualises our column-wise tissue and artifact classification results.

shape constraints. As in Chapter 3, the optimal surface graph construction method is adopted [8] in order to avoid user initialisation. However, by using an optimised cost function based on tissue classification, this initial segmentation is far more meaningful. The graph construction is then adjusted to impose local shape constraint, and a new shape prior term is incorporated into the cost function to impose a global constraint.

In order to automatically optimise the feature selection for the cost function, a supervised column-wise tissue classification is performed so that weightings for different types of features in the cost functions adapt to the tissue compositions in each individual column of pixels. To perform column classification, Haar-like features are extracted from each column in polar coordinates and classified in five categories for IVUS and three categories for OCT that represent different tissue properties using the Random Forests (RF) classifier. To compose the image-based cost function, a number of feature extraction methods are used, including derivatives of Gaussian and local phase, each of which has a different sensitivity to different types of tissues.

The weighting of those features in the image-based cost function is based on RF classification. A node-weighted directed graph is constructed with intrinsic local shape constraint. An initial segmentation is then obtained by computing the minimum closed set. Based on the initial segmentation and shape prior, the directed graph is updated to impose a more effective shape constraint and the shape prior is also incorporated into the cost function. The final segmentation is obtained by finding the minimum closed set on the adapted node-weighted graph. Figure 4.1 shows an example of the results using the proposed classification-based cost function and shape prior model. Through qualitative and quantitative comparisons, the proposed approach is shown to achieve superior performance compared to the state-of-the-art segmentation methods.

## 4.2 Tissue and Artifact Classification

As aforementioned, IVUS and OCT contain various forms of imaging artifacts that disrupt the continuity of lumen and media-adventitia borders. Hence it is desirable to detect those regions and treat them differently. In IVUS, calcification causes strong acoustic shadow and stents exhibit strong bright echo. In OCT, a stent casts a shadow behind its metallic strut, and calcified plaque has heterogeneous bright tissue with strong borders. There are some reported attempts to detect those artifacts and structures, such as calcification, metallic stent, and plaque, in both IVUS and OCT. In [269], the authors used intensity thresholding and contrast comparison to identify calcification in IVUS. Image gradient magnitude has also been used to detect calcification, e.g., [33]. In OCT, several works were proposed to detect a stent by using an intensity profile [192, 191], gradient information [150], and ridge detector [270]. An active contour method was also used in [271] to find the location of calcification after automatic segmentation of the lumen and guide wire based on the edge map. However, these heuristic driven approaches often rely on manually tuned parameters to make decisions. Machine learning methods have been recently applied to detect stents [272] and plaques [198]. Textural features, such as co-occurrence and local binary patterns, and geometrical features are used for supervised classification to localise those regions. To ensure satisfactory accuracy, these methods require a predetermined segmentation of the lumen and arterial borders, which itself is not a trivial task.

In this work, instead of the usual attempt of localising those image artifacts, which is problematic, we transform the images into polar coordinates, which is an intrinsic part of our graph construction, and classify the entire columns of pixels that may contain those imaging artifacts.

The idea of classifying the columns in polar coordinates comes from the physical construction of catheterisation coronary imaging in which the probe transmits radial lines of signal at different angles and receives its corresponding reflected echo, actually columns in the polar coordinates are representing the response coming from different angles and contains rich information about the characterisation of the tissues. The detection result will then have an influence on the formulation of the cost function, i.e., dynamically selecting appropriate features for each column.

We classify individual columns of pixels in the polar coordinates into a number of categories. For IVUS, we use five categories, i.e., calcification, fibrotic plaque, stent, guide-wire artifact, and normal tissue or soft plaque, because of both their different feature appearance and their influence on the media-adventitia border. For OCT, since some features such as calcification are below the lumen border, we only need to separate the guide-wire artifact, stent, and plaque or normal tissue. Calcification behind the lumen wall creates weaker features in OCT, partly due to its much stronger signal attenuation. Hence, in the case of OCT lumen segmentation, we group normal tissue with soft, fibrotic and calcified plaque to form a single class. Figure 4.1 shows an example image of the classification result.

Among many others, Support Vector Machines (SVM) and Adaptive Boosting are popular choices in supervised classification and have shown effective results on noisy images, e.g., ultrasound [273, 190, 272]. Some are more computationally expensive than others, e.g., pruning may be needed to improve SVM efficiency in classification but it increases training time [274, 275, 276]. In this work, we train a Random Forests classifier [277] to perform the task. RF is an ensemble classifier consisting of a set of unpruned decision trees, each decision tree is trained on a randomised selection of a subset of data sampling. At each node in every decision tree of the RF, a subset of feature variables is randomly selected to be used to determine the best split of the tree based on the Gini index or information gain criteria, which significantly improves the generalisation ability of the classifier compared to a single decision tree, and compared to SVM, RF is generally much more efficient to train and classify.

It is possible to directly use intensity values from each column for classification, since the goal is not to localise imaging artifacts but to determine which columns may contain them. However, particularly for IVUS, the intensity profiles from individual columns may appear similar to each other for certain classes, e.g., stent and calcification. We thus extract both horizontal and vertical Haar-like features at multiple scales. The horizontal template is defined as  $[1, -2, 1]$

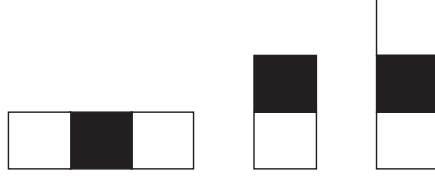


Figure 4.2: Haar-like Features.

to take into account neighbouring columns, and two vertical templates are defined as  $[-1, 1]^T$  and  $[1, -1, 1]^T$  to highlight edges and bar-like features as shown in Figure 4.2. These Haar-like features are similar to those that have been used in, for instance, face recognition [183]. Haar-like features are computed as the difference between the black rectangles and white rectangles. Since we are not dealing with localisation, one-dimensional templates are sufficient, which ensures efficiency.

### 4.3 Cost Function Optimisation

In this work, we propose a dynamic cost function based on the classification result to overcome the obstacles of detecting boundaries in IVUS and OCT, in which each column polar coordinates images is classified into a set of labels  $\mathcal{L}$  each of which has distinct features. The cost function can be defined as a combination of costs  $cf_l(x, y)$  that is defined based on label  $l$ :

$$C_B = \bigcup_{l \in \mathcal{L}} \bigcup_{(x, y) \in \mathcal{P}_l} cf_l(x, y), \quad (4.1)$$

Where  $\mathcal{P}_l$  is a set of columns in polar coordinates  $x, y$  that classified as label  $l$ . The cost  $cf_l(x, y)$  could have various forms based on not only edge or region cost, but it can also be a specific design cost to handle any obstacles.

Here, we adopt a boundary-based energy functional to form the basis of the classification-based cost function, which later is incorporated with shape prior. The boundary term in the energy function can be generically formulated as:

$$E_B = \sum_{V \in S} \hat{C}_B(x, y), \quad (4.2)$$

where  $S$  is a path in the directed graph. The actual formulation of the pre-normalised boundary cost  $C_B$  is determined by the result of RF classification, i.e., different tissue type requires

different feature selection.

### 4.3.1 IVUS cost function

For normal tissue and soft plaque, the media layer has a good contrast to adventitia. Hence,  $c_1$  is defined as

$$cf_1(x, y) = G_1(x, y), \quad (4.3)$$

where  $G_1$  is summation of filtering response of the first order Gaussian derivative (GD) from six different orientations. That is  $G_1$  measures total edge strength. The first order GD filters are designed so that the stronger the media-adventitia border the lower the filtering response.

Calcified plaque exhibits strong edge feature and casts varying degrees of acoustic shadow on media-adventitia border. We use normalised intensity  $\hat{I}(x, y)$  directly as feature, i.e.,

$$cf_2(x, y) = \hat{I}(x, y). \quad (4.4)$$

Which means that all the shadowing area underneath the calcified plaque has the same cost values. The calcified regions are then penalised, and meanwhile the smoothness constraint in graph construction and shape prior have much greater influence in determining the optimal location of the border.

Fibrous tissue exhibits similarly to calcification, except in majority cases the media layer is still discernible. Hence, combining the phase symmetry feature with the edge feature detection is appropriate to enhance the border, i.e.,

$$cf_3(x, y) = G_1(x, y) - \phi_s(x, y), \quad (4.5)$$

where  $\phi_s$  is the local phase symmetry feature. Note that  $G_1$  and  $\phi_s$  are generally not collocated when detecting the media-adventitia border, i.e.,  $\phi_s$  focuses on the middle of the media layer which is slightly above the media-adventitia border. To address this discrepancy, we accumulate the  $\phi_s$  response in a short line segment immediately above the current pixel so that  $\phi_s$  response is shifted downwards by a few pixels. We set the line segment length to be 8 pixels in consideration of the  $\phi_s$  parameter and the normal expectation of media layer thickness.

The presence of stents causes scattering of ultrasound signals, leading to very bright pixels. Hence, once a stent is detected by RF classifier, it is straightforward to localise the stent region which should not be part of the media or adventitia. The cost for the area above the stent

is assigned a positive constant as the desired border is below the stent. Second order GD responses ( $G_2$ ) are used to assign cost value for the regions underneath the stent, and  $G_2$  is rotational invariant measurement of bar-like feature. The same feature transformation used for  $\phi_s$  is applied to  $G_2$  due to the similar nature.

For the guide-wire artifact, there are also very bright pixels very close to the catheter, and it casts acoustic shadow or reverberation over its entire column. Hence, we do not extract any feature and a constant is used as their cost value.

### 4.3.2 OCT cost function

For OCT lumen segmentation, plaques in the artery pose little impact on the lumen border since they are not obstructing the lumen border. When there are no imaging artifacts, a good contrast along the lumen is achieved because the blood is flushed out before imaging. Hence, we can highlight the border based on intensity discontinuity. We use a combination of asymmetric local phase and the first order GD, both of which have good response to the lumen border. The cost function is thus defined as

$$cf_1(x,y) = G_1(x,y) - \phi_a(x,y), \quad (4.6)$$

where  $\phi_a$  is the local phase asymmetry feature. A stent is implanted between the lumen and intima. Optical shadow caused by stent in OCT is narrow and generally behind the lumen border, see Figure 4.1. The guide-wire artifact in OCT is similar to the stent and has a bright echo usually near the catheter, casting large shadows. Hence, it is treated in the same way, i.e., we assign a constant cost value to the entire columns that are detected as containing guide-wire artifacts. We rely on other constraints to estimate the lumen border at regions where no or very little imaging information is available for the border of interest.

## 4.4 Shape Prior Model

The proposed shape prior consisted of two terms; cost function and graph construction, the cost function is defined as a likelihood term of each node in the graph, which is based on the similarity between the initial shape (obtained by finding the minimum closed set of our basic graph) and prior shapes. Whilst, the graph construction is modified so that inter-column arcs change dynamically according to the prior. The energy term for shape prior can be expressed

as:

$$E_S = \sum_{(x,y) \in \mathcal{S}} \mathcal{C}_P(x,y) + \sum_{(p,q) \in \mathcal{N}} f_s(S(p) - S(q)), \quad (4.7)$$

where  $\mathcal{C}_P$  denotes the cost function associated to prior and  $f_s$  is a convex function penalising abrupt changes in  $S$  between neighbouring columns  $p$  and  $q$  in the set  $\mathcal{N}$  of neighbouring columns in the graph.

#### 4.4.1 Graph construction: shape prior

As aforementioned in Chapter 3, The images are first transformed from Cartesian coordinates to polar coordinates to facilitate our feature extraction and classification, as shown in Figure 4.1, and the catheter region can be easily removed as it is fixed in size and location. The lumen and media-adventitia borders in the polar coordinates are shown as interfaces that intersect with each column once and once only. This allows us to define the segmentation of these borders as an optimal path in the horizontal direction. In order to adapt the graph construction based on shape prior, we follow a similar approach to [278] by using a convex function define on neighbouring columns. However, different to previous approaches, a smoothness constraint is imposed at the initial stage of estimating the border of interest and shape clustering is performed with the nearest set selected to generalise the shape prior.

Let  $G = \langle V, E \rangle$  denote the graph, where each node  $V(x, y)$  corresponds to a pixel in the transformed IVUS image  $I(x, y)$  in polar coordinates. Here, the graph  $G$  consists of three arc types: intra-column, inter-column and smoothness arcs, see Figure 4.3. The intra-column is still the same as in Chapter 3 to ensure that the desired interface intersects with each column exactly once, accordingly along each column every node  $V(x, y)$ , where  $y > 0$ , has a directed arc to the node  $V(x, y - 1)$  with  $+\infty$  weight assigned to the arc.

In the case of inter-column, for each node  $V(x, y)$  a directed arc with  $+\infty$  weight is established to link with node  $V(x + 1, y - \bar{\Delta}_{p,q})$ . Similarly, node  $V(x + 1, y)$  is connected to  $V(x, y + \underline{\Delta}_{p,q})$ , where the difference between two neighbouring columns  $p$  and  $q$  of the desired border is in between  $\bar{\Delta}_{p,q}$  and  $\underline{\Delta}_{p,q}$  and it acts as a hard constraint. Inter-column and intra-column arcs are illustrated in Figure 4.3(a).

A convex function  $f_{p,q}(h)$  is defined between neighbouring columns  $p$  and  $q$  to penalise inter-column changes that deviate from expectation (obtained from prior) in  $S$  and impose smooth inter-column transitions (see orange arcs in Figure 4.3 (b)). To that end, the smoothness penalty

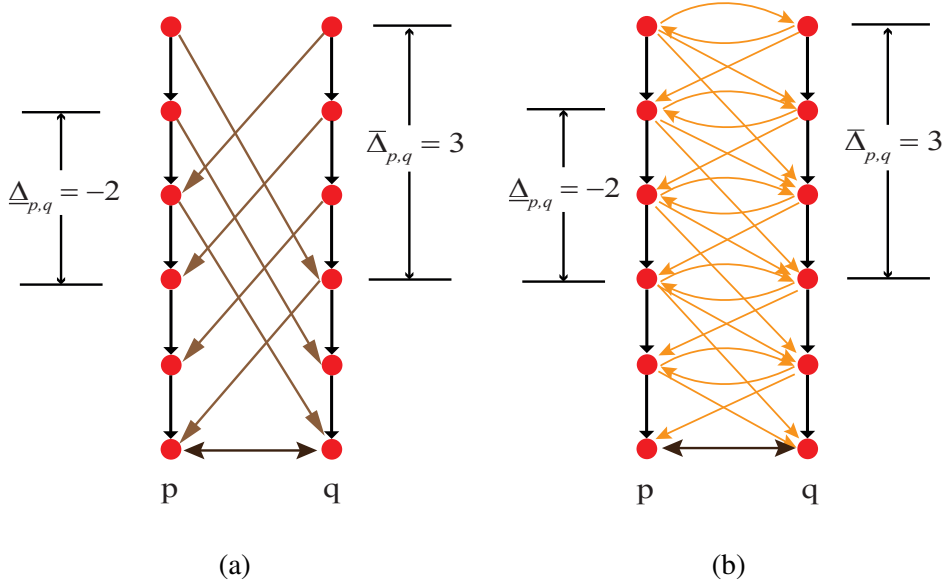


Figure 4.3: Example graph construction. (a) inter-columns arcs connecting two neighbouring columns and, where  $\Delta_{p,q} = -2$  and  $\bar{\Delta}_{p,q} = 3$  in this example, shown as brown arcs. (b) smoothness arcs, in orange, for the same columns when  $f'_{p,q}(0) = 0$ .

arcs are constructed with intermediate links, i.e.,  $h \in (\Delta_{p,q}, \bar{\Delta}_{p,q})$  for inter-column arcs. The direction of these arcs is based on the first order derivative of the convex function  $f_{p,q}(h)$ . Here, we employ a quadratic function,  $f_{p,q}(h) = \eta_1 (h - \mu_{p,q})^2$  where  $\eta_1$  is a weighting factor for smoothness constraint and  $\mu_{p,q}$  is the expected difference between neighbouring columns  $p$  and  $q$ . If the inter-column difference matches expectation, i.e.  $f'_{p,q}(h) = 0$ , two directional arcs of opposite direction are established between  $V(x, y)$  and  $V(x + 1, y - h)$ . The weights on the arcs are determined by the second order derivative of the convex function ( $f''_{p,q}(h)$ ) and are equally distributed. If  $f'_{p,q}(h) > 0$ , an arc from  $V(x, y)$  to  $V(x + 1, y - h)$  is established and its weight is assigned as  $f''_{p,q}(h)$ ; and if  $f'_{p,q}(h) < 0$ , the arc is connected from  $V(x + 1, y)$  to  $V(x, y + h)$  with its weight also assigned as  $f''_{p,q}(h)$ . The cost of cut between columns  $p$  and  $q$  depends on the border difference  $\Delta_{p,q} \leq S(p) - S(q) \leq \bar{\Delta}_{p,q}$  and it equals the convex function  $f_{p,q}(S(p) - S(q))$ .

In this work, we use this mean difference,  $\mu_{p,q}$ , to impose shape prior in graph construction, in addition to the shape prior term in the cost function. The training shapes are also transformed into polar coordinates.  $K$ -means clustering is then carried out to group those 1D shapes. Shape alignment may be carried out before clustering; however, it is generally computationally ex-

pensive given the large dataset we have. Clustering these 1D shape profiles is inexpensive. The nearest cluster may be selected to impose the shape constraint in graph construction. Hence an initial segmentation with an elastic smooth constraint in graph construction, i.e.  $\mu_{p,q} = 0$ , is carried out to select the nearest cluster. The inter-column differences are then generalised using mean  $\mu_{p,q}$  and standard deviation  $\sigma_{p,q}$  on individual columns. These statistics are then used in determining maximum and minimum distances when connecting neighbouring columns, i.e.,  $\bar{\Delta}_{p,q} = \mu_{p,q} + c \cdot \sigma_{p,q}$ ,  $\underline{\Delta}_{p,q} = \mu_{p,q} - c \cdot \sigma_{p,q}$ , and  $c$  is a real constant. The smoothness arcs are also defined between  $\underline{\Delta}_{p,q}, \bar{\Delta}_{p,q}$ . These inter-column arcs impose a hard constraint, enforcing a general variation in shape with its details determined by minimising the cost function that is based on both image feature and shape prior.

#### 4.4.2 Cost function: shape prior

In [164], Cremers et al. introduce a nonparametric shape prior model based on multiple shape templates to be incorporated with a level set method. Notably in [268] the authors transform the method into discretization domain and used a graph cut as the segmentation method. The terminal edge connection is determined by comparing the initial labelling with the template, e.g., if the node is in the template but not in the initial labelling, it connects to the source. However, the method is still dependent on the user interaction to determine the object and background and needs multiple iterations until convergence. In this work, we adopt a nonparametric estimation method to add a statistical shape prior model without any user intervention.

Each shape in the training set is treated as a binary template,  $v$ , where the interior is set to one and the exterior is set to zero. The distance between two templates  $v^a$  and  $v^b$  is defined using a discrete version of Zhu-Chan distance [279], which is in effect the sum of the squared difference:

$$d^2(v^a, v^b) = \sum_{\Omega} (v^a - v^b)^2. \quad (4.8)$$

where  $\Omega$  denotes the image domain. This distance measure is a true metric and is not influenced by image size. Let  $\Upsilon = v^1, \dots, v^N$  denote the  $N$  number of shapes from the training set. Given a possible cut in the graph which produces an aligned binary shape  $f$ , its similarity to a shape template  $v^n$  in the training set is computed as:

$$\alpha(f, v^n) = \exp\left(-\frac{1}{2\sigma^2} d^2(f, v^n)\right). \quad (4.9)$$

Thus, the likelihood of this particular cut can be evaluated by taking into account of all training shapes and based on nonparametric kernel estimation:

$$c_{R_0} = \frac{\sum_{n=1}^N \alpha(f, v^n) v^n}{\sum_{n=1}^N \alpha(f, v^n)}. \quad (4.10)$$

In our case, an initial cut can be conveniently obtained by minimising the classification-based cost function alone. Note, it is fully automatic and there is no need for user initialisation. The labelling of the shape likelihood and initial cut needs to be compared in order to assign appropriate terminal arcs. The shape prior cost is defined as:

$$\mathcal{C}_P(x, y) = \eta_2 |c_{R_0}(x, y) - c_{R_1}(x, y)|, \quad (4.11)$$

where  $c_{R_0}$  and  $c_{R_1}$  denote the cost associated to prior for the inferior region (the region under the border) and superior region (the region above the border) respectively, and  $\eta_2$  is the weight for the shape prior cost. The summation of the normalised weighted templates  $c_{R_0}$  is in effect the inferior-region cost and is inversely proportional to the likelihood of a pixel belonging to the region underneath the border of interest. To define the superior-region prior cost  $c_{R_1}$ , we simply compute the complement of  $c_{R_0}$ , i.e.  $c_{R_1} = \max_{x,y} c_{R_0}(x, y) - c_{R_0}(x, y)$ . As shown in Section 4.5, the shape prior cost  $\mathcal{C}_P$  is used to assign weights for each pixel according to its position from the border. By assigning the shape prior cost in this way, we eliminate the need to identify the terminal connection type. The complexity of computing the cost function term of the shape prior is  $O(N)$  where  $N$  is the shape templates.

## 4.5 Graph Cut

Every cost function, boundary-based term  $\mathcal{C}_B$  and shape prior term  $\mathcal{C}_P$ , is inversely correlated to the likelihood that the border of interest passes through pixel  $(x, y)$ . The weight for each node on the directed graph can be assigned as by computing the first derivative between every two consecutive nodes along the same column of the cost function. Thus, finding the optimal border is achieved by defining the minimum-cost closed set in the directed graph using the  $s - t$  cut algorithm by dividing the vertices into negative  $V^-$  and positive  $V^+$  subset based on its weight  $w(v)$ ,  $v \in V$  and connect each subset to the source  $s$  and  $t$  respectively with the absolute weight value. An efficient 1D RBF interpolation using the thin plate base function is also used to obtain the smoothed final interface.

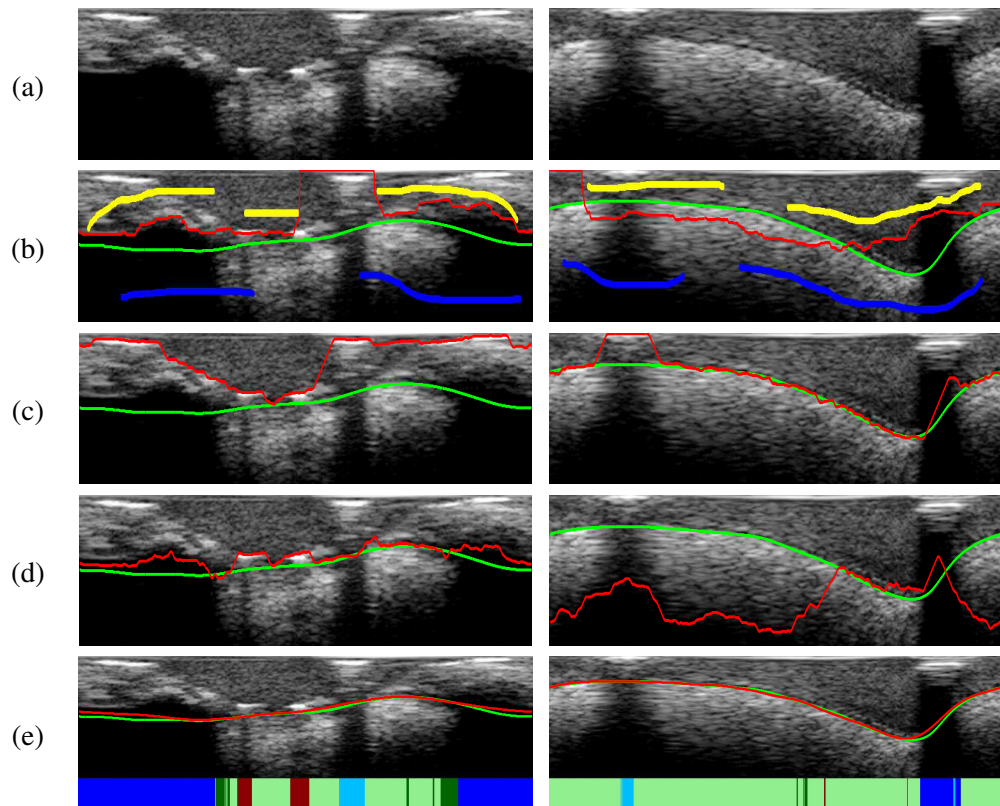


Figure 4.4: Comparison between ground-truth (green) and segmentation results (red): (a) Original image; (b)  $s-t$  cut [7] (foreground: yellow, background: blue); (c) Optimal surface [8] with 1st order GD; (d) Optimal surface [8] with 2nd order GD; (e) Proposed method: bottom of each image also visualises the RF classification result: calcified plaque (blue), fibrotic plaque (dark green), stent (dark red), guide-wire shadowing (cyan), and soft plaque/normal tissue (light green).

## 4.6 Experimental Results

Two datasets are used for the evaluation of the proposed method, one of which contains 33,220 IVUS images and the other contains 2,283 OCT images. The datasets were captured from both left anterior descending arteries (LAD) and right coronary arteries (RCA). Manual labelling was carried out to establish ground-truth for quantitative analysis. The proposed method was compared against a number of recent and state-of-the-art techniques, which include optimal surface graph cut [8], star graph cut [1] and texture-RBF for IVUS segmentation [27]. Five different evaluation metrics defined in equation (3.13) were used to evaluate the performances: absolute mean difference, Hausdorff distance, area overlap, sensitivity and specificity.

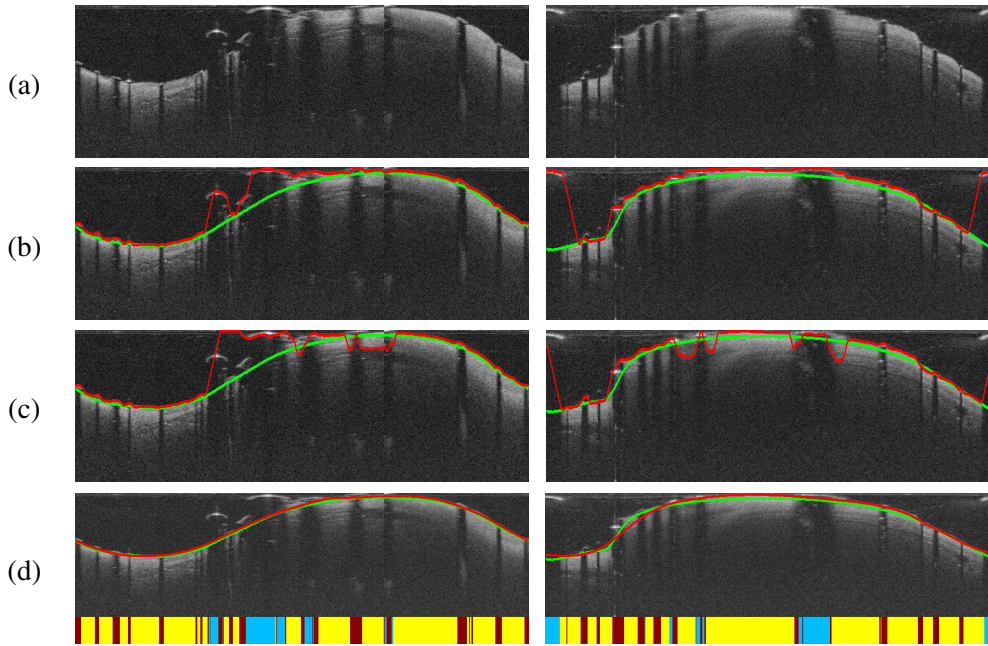


Figure 4.5: Comparison between ground-truth (green) and segmentation results (red): (a) Original image; (b) Optimal surface [8] with 1st order DoG; (c) Optimal surface [8] with local phase asymmetry; (d) Proposed method: bottom of each image also visualises the RF classification result: stent (dark red), guide-wire shadowing (cyan), and plaque/normal tissue (yellow).

Table 4.1: IVUS column-wise tissue classification.

| Accuracy(%) | IVUS               |          |               |       |            |        |              |
|-------------|--------------------|----------|---------------|-------|------------|--------|--------------|
|             | Class              | Fibrotic | Calcification | Stent | Guide-wire | Others | Overall      |
|             | Intensity features | 62.42    | 88.16         | 59.97 | 72.75      | 89.87  | 80.64        |
|             | Haar-like features | 72.52    | 89.67         | 64.42 | 80.84      | 89.72  | <b>83.78</b> |

#### 4.6.1 IVUS segmentation

A total of 33,220 IVUS images of  $240 \times 1507$  pixels in polar coordinates from 10 *in vivo* pullbacks were acquired by a 40 MHz catheter Atlantis SR Pro, Boston Scientific ultrasound machine. Manual labelling was carried out on every 10th frame, i.e., 3322 frames to establish ground-truth for quantitative analysis<sup>1</sup>. These images contain various forms of fibrous plaque, calcification, stent, and acoustic shadow.

<sup>1</sup>Manual labeling the entire dataset is too time consuming. However, quantitative comparison on every 10th frame should provide reliable assessment.

To perform column-wise tissue classification, we randomly selected a small number of images for supervised training, i.e., 615 IVUS images or less than 2% of the IVUS images. The total number of trees in RF is set to be 500 and the number of features used to make the decision at a node of the tree is  $4\sqrt{L}$ , where  $L$  is the length of feature vector. The IVUS feature length is 3808 computed from a vertical window of size 128 and horizontal window size of 512. Using the proposed Haar-like feature, we achieved a modest improvement in overall accuracy from 80.64% using intensity-based feature in our earlier work [280] to 83.78% in classifying individual columns of pixels into five different categories. Detailed classification results are shown in Table 4.1. However, since most columns of pixels are classified as “others” (mainly contain normal tissues), there are substantial improvements in classifying columns that contain imaging artifacts, e.g., fibrotic tissue classification increased from 62.42% to 72.52%. The same amount of images are used to generalise the shape prior to impose shape constraints both at the graph construction stage and at energy minimisation.

The number of training templates for the shape prior is 667, while the number of shape clusters set as 40 in which the nearest cluster based on the initial segmentation is used to adapt the graph construction for the shape prior model. The shape prior parameters are defined as  $\eta_1 = 0.06$ ,  $\eta_2 = 0.083$ . Note,  $\eta_1$  controls the amount of freedom that the border can move around the expected difference  $\mu_{p,q}$ , and between the hard constraints of neighbouring columns  $p$  and  $q$ .

First, we provide a comparison to a conventional graph cut method that does not use shape prior constraints but relies on user intervention to guide segmentation. In Figure 4.4, we qualitatively compare our proposed method (row (e)) to the conventional  $s-t$  cut algorithm (row (b)). The  $s-t$  cut does not incorporate shape prior into the cost function. Instead, prior information is incorporated through user initialisation by providing strokes on foreground and background regions. Even with careful initialisation, the conventional  $s-t$  cut did not produce satisfactory results. Due to its high initialisation dependency and relatively intensive manual process, we did not carry out a full quantitative analysis. However, later we show a full quantitative comparison to an alternative graph cut which also adopts user initialisation but which we believe is more suited for IVUS segmentation. The failure of standard  $s-t$  cut suggests that a stronger prior is necessary and also the image features and its cost function may need to be tailored for IVUS.

Next, we employ the optimal surface graph [8], which is the basis of our graph construction

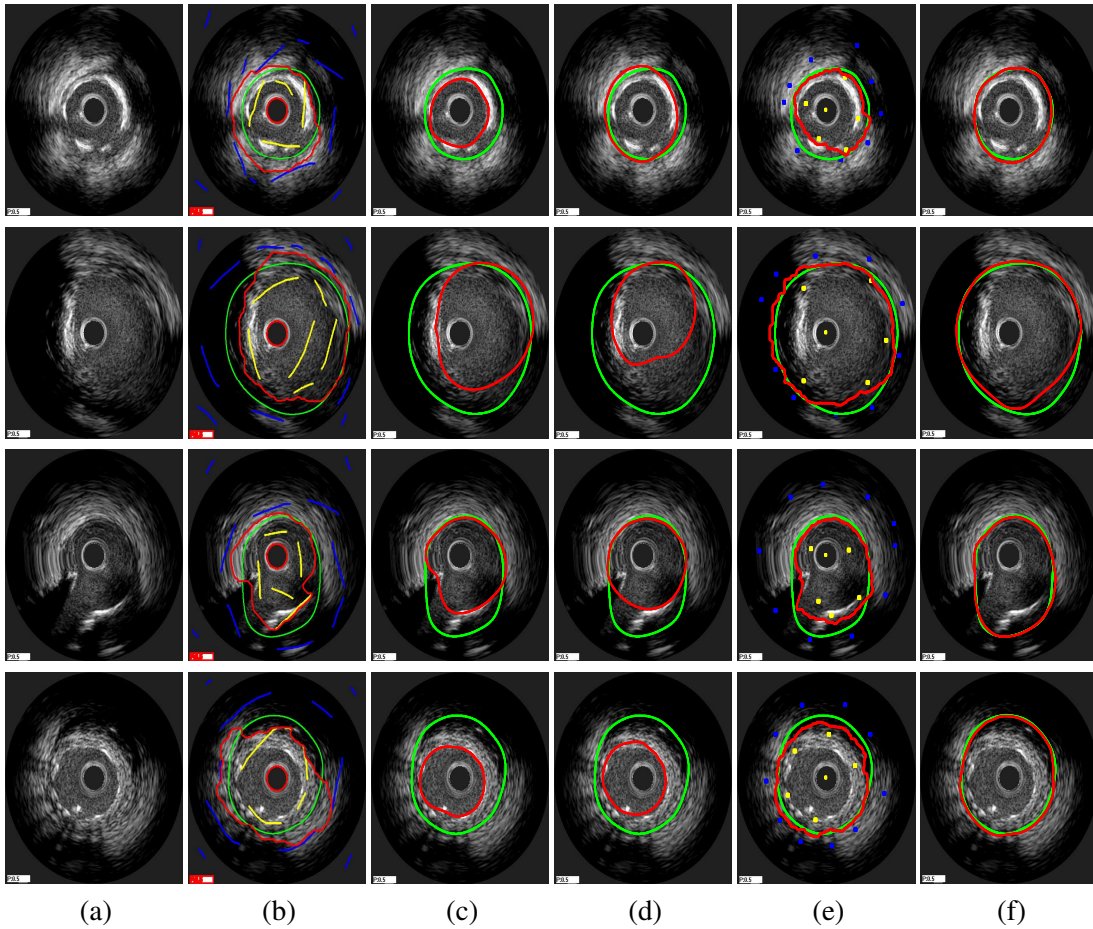


Figure 4.6: Comparison between ground-truth (green) and segmentation results (red): (a) original image. (b)  $s-t$  cut (foreground user strokes: yellow, background user strokes: blue). (c) optimal surface [8] with first order GD. (d) Texture-RBF method. (e) star graph cut (foreground user points: yellow, background user points: blue). (f) proposed method.

and the single/double interface segmentation described in Chapter 3, to examine the role of image features. The first and second order GD features are the fundamental features in our method. Hence, we applied these two features separately with an optimal surface graph, with the same local shape constraint as in the proposed method. Rows (c) and (d) in Figure 4.4 show typical results of applying first order GD and second order GD with the optimal surface graph, respectively. With the proposed method, we used RF to classify five different types of tissue and adapted the cost function accordingly. The bottom of each image in row (e) visualises the classification result. Further examples of the optimal surface method can be found in column (c), Figures 4.6, 4.7. The quantitative results are shown in Table 4.2. It is evidently clear

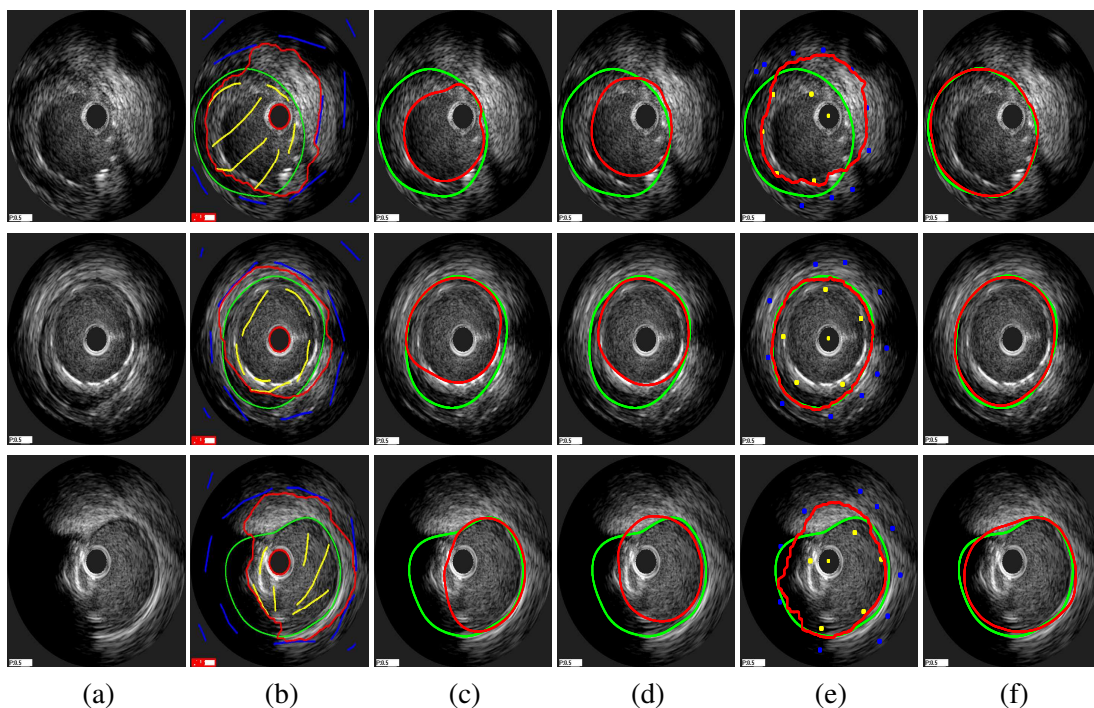


Figure 4.7: Comparison between ground-truth (green) and segmentation results (red): (a) original image. (b)  $s - t$  cut (foreground user strokes: yellow , background user strokes: blue). (c) optimal surface [8] with first order GD. (d) Texture-RBF method. (e) star graph cut (foreground user points: yellow , background user points: blue). (f) proposed method.

Table 4.2: IVUS quantitative comparison. AMD: absolute mean difference(pixel); HD: Hausdorff distance(pixel); AO: area overlap(%); Sens.: sensitivity(%); Spec.: specificity(%).

|                                 | AMD         | HD           | AO           | Sens.        | Spec.        |
|---------------------------------|-------------|--------------|--------------|--------------|--------------|
| Optimal surface [8] with 1st GD | 21.94       | 53.77        | 83.57        | 84.57        | <b>98.87</b> |
| Optimal surface [8] with 2nd GD | 35.52       | 68.97        | 78.92        | 94.46        | 77.77        |
| Texture-RBF method [27]         | 21.68       | 49.82        | 83.67        | 87.92        | 95.60        |
| Star Graph cut [1]              | 14.70       | 38.98        | 89.11        | 94.90        | 92.84        |
| Proposed method                 | <b>6.92</b> | <b>20.30</b> | <b>94.65</b> | <b>96.58</b> | 97.63        |

that the proposed method achieved significantly superior performance, e.g., the absolute mean difference for the proposed method is 6.92 compared to 21.94 and 35.52 for optimal surface with two different feature sets.

We also implemented the Texture-RBF method [27], which is designed for segmenting IVUS. Its overall performance is very similar to the optimal surface graph, as shown in Table 4.2.

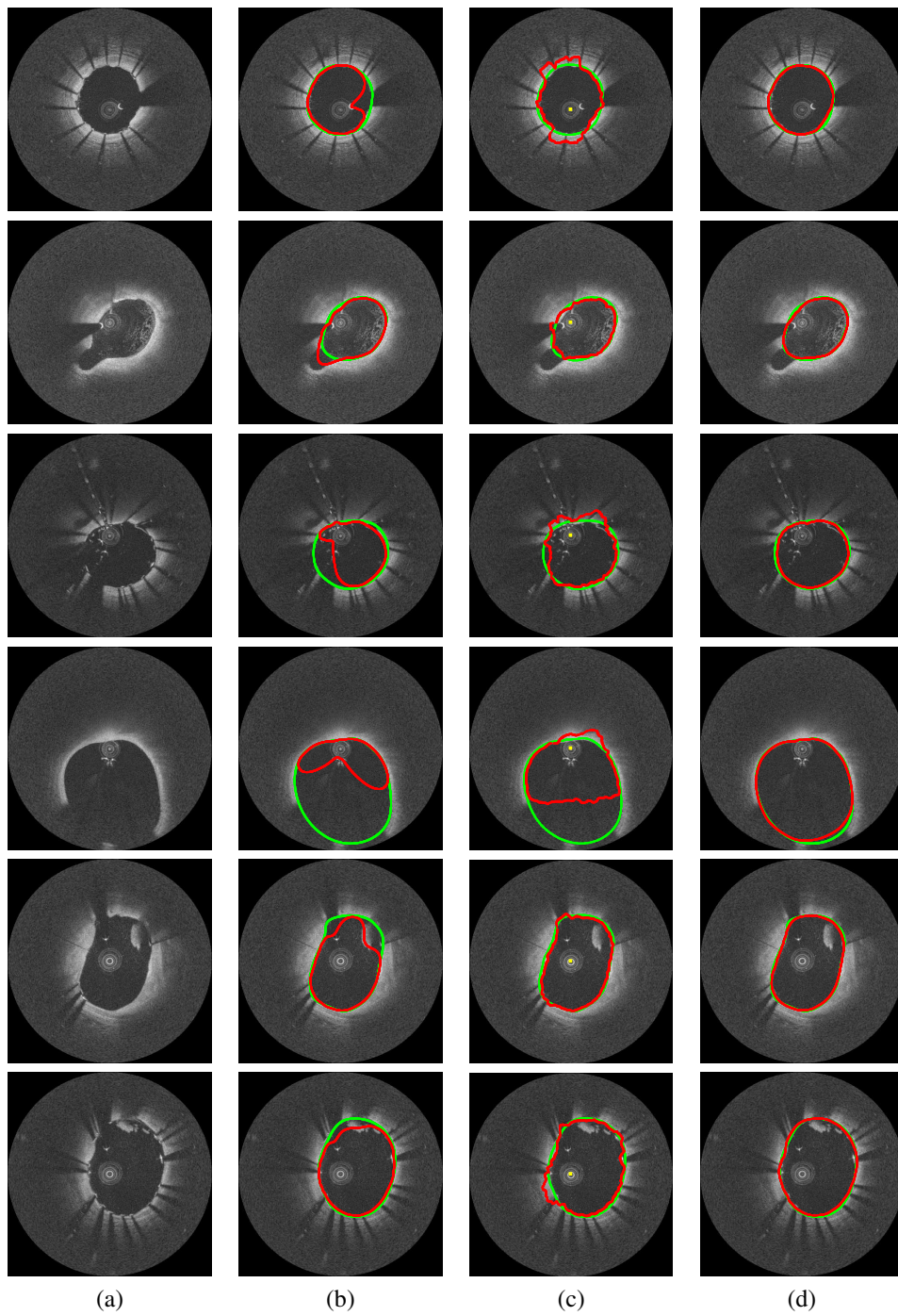


Figure 4.8: Comparison between ground-truth (green) and segmentation results (red): (a) original image. (b) optimal surface [8] with first order GD. (c) star graph cut (star point: yellow). (d) proposed method.

Table 4.3: OCT column-wise tissue classification.

| Accuracy(%)        | OCT   |            |        |              |
|--------------------|-------|------------|--------|--------------|
| Class              | Stent | Guide-wire | Others | Overall      |
| Intensity features | 44.08 | 95.69      | 97.64  | 89.47        |
| Haar-like features | 82.82 | 95.91      | 99.25  | <b>96.27</b> |

Example results are shown in column (d) in Figures 4.6, 4.7. This method consistently underestimated the media-adventitia border and it cannot deal with image artifacts, e.g., calcification and stents.

Finally, we compare our method against the semi-automatic star graph cut [1]. Since the media-adventitia border is assumed on the radial direction from the catheter centre without obstruction, the intrinsic shape regularisation in the star graph cut is well suited for IVUS segmentation, i.e., the catheter centre is treated as the star point and the media-adventitia border lies on the radial spikes from the star point. Segmentation using a single user point (star point) however resulted in failure in most cases. Hence, additional user points were carefully placed on each cross section: 5 foreground points and 10 background points, see column (e) in Figure 4.6, 4.7. These additional constraints improved its performance, but it was still adversely affected by IVUS artifacts. The proposed method, as shown in column (f), showed very close segmentation to the ground-truth. Comparative quantitative results are shown in Table 4.2. It clearly shows statistically significant improvements of the proposed method.

#### 4.6.2 OCT segmentation

The OCT dataset consists of 13 *in vivo* pullbacks acquired from a C7-XR LightLab Imaging system, a total of 1846 images are manually labelled to define groundtruth.

For column-wise tissue classification, 476 images were randomly selected from three pullbacks to train the RF classifier. The overall accuracy using the proposed Haar-like features is 96.27%, compared to an overall accuracy of using a pixel intensity profile of 89.47%. The main improvement is in detecting stents, i.e., a substantial improvement from 44.08% to 82.82%. Detailed classification results for each type of tissue can be seen in Table 4.3. Those same images are then used to learn shape prior, in the same way as in IVUS segmentation. The number of shape templates that were for OCT is 457 and clustered into 30 classes. The shape prior

Table 4.4: OCT quantitative comparison. AMD: absolute mean difference(pixel); HD: Hausdorff distance(pixel); AO: area overlap(%); Sens.: sensitivity(%); Spec.: specificity(%).

|                                 | AMD         | HD           | AO           | Sens.        | Spec.        |
|---------------------------------|-------------|--------------|--------------|--------------|--------------|
| Optimal surface [8] with 1st GD | 7.25        | 37.06        | 89.44        | 89.76        | 99.80        |
| Star Graph cut [1]              | 5.86        | 22.23        | 91.49        | <b>96.28</b> | 98.16        |
| Proposed method                 | <b>3.31</b> | <b>11.16</b> | <b>95.17</b> | 95.59        | <b>99.82</b> |

parameter  $\eta_2 = 0.2$ .

Table 4.4 shows the quantitative comparison between the star graph [1] and our proposed method. Here, the star graph method requires the catheter region to be removed before segmentation in order to obtain meaningful results. Similar to IVUS segmentation, the proposed method achieved superior performance in segmenting the lumen border in OCT. Figure 4.8 shows typical results of star graph cut and our proposed method.

## 4.7 Summary

An automated segmentation method to delineate media-adventitia and lumen borders in two rather different intravascular imaging modalities, i.e. IVUS and OCT was presented. The proposed method uses local and global shape constraints in both graph construction and adaptive cost function implementation. Tissue classification proved useful to optimise the cost function and we show that column-wise classification is sufficient, rather than pixel-wise classification which is problematic, and helpful to produce meaningful initial segmentation, based on which shape prior was effectively imposed to regularise the border extraction. Comprehensive comparative analysis has shown statistically significant improvements in segmentation accuracy when compared to both conventional graph cut methods and state-of-the-art approaches, including optimal surface and star graph cut. However, the relationship between consecutive frames is not explicitly examined.

## Chapter 5

# Longitudinal Tracking and Segmentation

### Contents

---

|     |  |     |
|-----|--|-----|
| 5.1 | Introduction . . . . .   | 83  |
| 5.2 | Border Parameterisation . . . . .                              | 86  |
| 5.3 | Spatio-Temporal Segmentation Using the Kalman filter . . . . . | 87  |
| 5.4 | Tracking Through HMM Modelling . . . . .                       | 91  |
| 5.5 | Summary . . . . .  | 102 |

---

### 5.1 Introduction

Object tracking has been widely used in many applications such as motion-based recognition [281], surveillance [282, 283], and medical imaging [284, 285]. The goal is to track the object trajectory over time and identify the object location in every time frame. The object can be represented in various forms, e.g., points, geometric shape, and contour. Geometric shapes, e.g., rectangle and ellipse, are suitable for representing rigid objects, such as vehicles, where the tracker tries to estimate motion parameters. Tracking object contour is sometimes carried out using complex and nonrigid shapes where a contour provides more accurate representation than a bounding box for the object. In this chapter, we present approaches to track IVUS and OCT anatomical borders over the longitudinal axis, in order to achieve more coherent segmentation.

Kalman and particle filters are popular Bayesian probabilistic tracking models used in the estimation of the object over time. The Kalman filter is a linear dynamic estimator that predicated the system state over time and corrects its estimation by the measurements acquired in the current instant of time. The Kalman filter can produce an optimal solution with a system corrupted by a white noise and be extended to tackle a non-linear system or measurement by using one of these approaches: extended Kalman filter and unscented Kalman filter. A particle filter is a non-linear/non-Gaussian estimator model that represents the state vector by a set of samples called particles. Over time, these particles propagate to the next frame; each particle has a weight that is computed based on the observation taken at the current frame. The filter resamples these particles based on their weight and the final object position can be estimated based on the new sampling. However, a particle filter is more computationally expensive than Kalman. Moreover, authors in [286] argue that a particle filter requires a large number of samples and with increasing the dimension of system space its performance can deteriorate.

Various techniques of contour detection methods have been used in tracking and could be integrated with the state space model; for example, active contour and hidden Markov model. Active contour is an energy minimisation method that utilises two forces: internal force describes the regularity of the contour shape, and external force describes the boundary features to evolve the contour to reach the object boundary. For example, Terzopoulos *et al.* [287] represent the system state by B-spline control points and integrate the Kalman filter with the snake model. In [288], authors also used B-spline representation and proposed the Condensation algorithm to track affine motion parameters using a particle filter. The measurement is computed by extracting edge features along normal lines. In [285] authors use watershed segmentation to initialise the contour position and then evolve an edge-based snake to track the left ventricle in echocardiographic images. However, active contour heavily depends on the initialisation of the contour and may converge to the local minima. A Level set has been also used in tracking [289, 290, 291].

The hidden Markov model (HMM) is a stochastic model in which the Markov property is assumed to be satisfied in a finite set of states in which these states are hidden. Many applications have demonstrated the advantage of HMM to deal with the time-varying signals such as speech recognition [292], classification [281], and tracking [293, 294, 295]. In [281], authors use HMM to classify the local wall motion of stress echocardiography to normal or abnormal. They build two HMM models, one for each class and use a forward algorithm to compute the

probability of the observation of each model. In [296], HMM is used in conjunction with a particle filter to track hand motion. A particle filter is used to estimate the hand region that is most likely to appear. HMM estimates the hand shape using the Viterbi algorithm where the state is a set of quantised pre-learned exemplars [297]. However, the number of exemplars can grow exponentially depending on the complexity of the object. In [298], the authors used the Kalman filter with P2DHMM (pseudo 2-dimensional HMM) to perform a person tracking. P2DHMM is a nested 1D HMM in which a number of super hidden states modelling image columns, each of which contains another number of HMM hidden states. The Viterbi algorithm is used to find the best sequence of states that classify the image as object and background. These measurements are used by the Kalman filter to predicate the rectangle box containing the object in the next frame. However, the system becomes more complex and time-consuming with the increase of object size. In [293, 294], the authors incorporated region and edge features with HMM. The contour is sampled into a set of discrete points, and the features are extracted along the normal direction at each contour point. The ellipse shape is fitted based on the contour and the unscented Kalman filter is used for tracking. In [295], authors extended the previous idea to deal with variable length open contours and investigated using arc emission instead of traditional state emission for defining the observation probabilities of the HMM. The optimal contour is identified using the Viterbi algorithm.

In this chapter, two tracking methods that combine cross-sectional segmentation and longitudinal tracking are proposed, in order to efficiently delineate the arterial borders in IVUS and OCT with the presence of occlusions and image artifacts. The transformation of coronary images from Cartesian coordinates to polar coordinates allows efficient parametrisation of the border using radial basis functions (RBF) and thus reduces the tracking size from a large number of border points to a very few RBF centres.

In the first proposed method, a node-weighted directed graph is constructed on two consecutive cross-sectional frames with embedded shape constraints within individual frame and between consecutive frames. The intra-frame constraints are derived from a set of training shapes and are embedded in both the graph construction and its cost function as presented in Chapter 4. The inter-frame constraints are imposed by tracking the border of interest across multiple frames, i.e., the longitudinal constraint is derived far beyond two consecutive frames that are used in graph construction. Moreover, to improve the consistency among cross sections, we integrate Kalman filtering into our segmentation process to produce coherent and consistent

results. In the second method, an HMM-based border tracking method is presented. The emission probabilities are defined based on two probability distributions for the arterial border and background respectively that are derived directly from both the classification-based cost function and the shape prior model. Arc and state HMM emission are examined for better HMM accuracy. The training of the transition probability is achieved by using the forward-backward algorithm. The optimal sequence of the hidden states corresponds to RBFs of the border and is obtained by using the Viterbi algorithm.

## 5.2 Border Parameterisation

Tracking all the border points in their polar coordinates is computationally expensive. Alternatively, we interpolate the border using radial basis functions. Thus, tracking the border of interest becomes localising those RBF centres at a set of angular positions in the polar coordinates. The thin plate local compact support RBF is used for interpolation. The movement of the border across frames is in effect determined by the locations of those RBF centres.

The radial basis function is defined as a linear combination of the basis functions  $\Phi$  and a low degree polynomial term  $p(x)$ , each basis function associated with a weighted coefficient  $\omega_j$ , and centred at the constraint locations  $c_i$ . RBF [299] is formulated as:

$$f(\mathbf{x}) = \sum_{i=1}^M \omega_i \Phi(\mathbf{x} - c_i) + p(\mathbf{x}), \quad (5.1)$$

where  $\mathbf{x}$  is the border points. The thin-plate function is given by  $\Phi(x) = |x|^2 \log(|x|)$ . To find the unknown parameters, the weights  $\omega_i$  and the coefficients of  $p(\mathbf{x})$  that satisfy the interpolation constraints, the border points which define the RBF centres must interpolate the function  $y_i = f(c_i)$ . Since the RBF is a linear equation with respect to unknown parameters, the interpolation problem could be written as a linear system as following:

$$\begin{bmatrix} \Phi_{11} & \Phi_{12} & \dots & \Phi_{1M} & 1 & c_1 \\ \Phi_{21} & \Phi_{22} & \dots & \Phi_{2M} & 1 & c_2 \\ \vdots & \vdots & \ddots & \vdots & \vdots & \vdots \\ \Phi_{M1} & \Phi_{M1} & \dots & \Phi_{MM} & 1 & c_M \\ 1 & 1 & \dots & 1 & 0 & 0 \\ c_1 & c_2 & \dots & c_M & 0 & 0 \end{bmatrix} \begin{bmatrix} \omega_1 \\ \omega_2 \\ \vdots \\ \omega_M \\ p_0 \\ p_1 \end{bmatrix} = \begin{bmatrix} y_1 \\ y_2 \\ \vdots \\ y_M \\ 0 \\ 0 \end{bmatrix} \quad (5.2)$$

where  $\Phi_{ij} = \Phi(c_i - c_j)$ . This linear system is solved by symmetric lower upper (LU) decomposition.

### 5.3 Spatio-Temporal Segmentation Using the Kalman filter

Thus far, segmentation is carried out on a frame-by-frame basis, which is commonly used in object localisation, e.g., [27], [14],[33]. However, it ignores the temporal information which could help to refine the object estimation, particularly when there is large uncertainty due to image artifact or noise. In optimal surface segmentation [8], the authors added the shape constraints between columns in neighbouring frames as a constant value along the whole volume, whose optimal value is difficult to choose. The optimal surface method would also require substantial memory to construct a 3D volume for thousands of IVUS or OCT frames. In [278], the authors used mean and standard deviation to model the shape variation between neighbouring frames.

Here, we propose a spatio-temporal segmentation that is adaptive and only requires additional graph construction at adjacent frames. The spatial information is obtained by the proposed graph-based segmentation using both boundary and shape prior cost as described previously and the temporal information is extracted by using a Kalman filter to predict the border location in polar coordinates across frames and use this prior information to find the final location of the border by adjusting the graph construction constraints between two consecutive frames.

#### 5.3.1 Kalman filter

The Kalman filter is an optimal estimator based on a linear state space system that recursively perform two processes: prediction and measurement. Generally the state estimation is defined as [300]:

$$x_t = Ax_{t-1} + w_t \approx N(0, Q), \quad (5.3)$$

and the measurement:

$$z_t = Hx_t + v_t \approx N(0, R), \quad (5.4)$$

where  $A$ ,  $H$  are the state transition and measurement matrices, and  $w_t$ ,  $v_t$  are process and measurement Gaussian white noise respectively, with covariance matrices  $Q$  and  $R$ . A continuous Wiener process acceleration (CWPA) model [300] is used to estimate the RBF motion model and define the  $A$  and  $Q$  matrices. The matrix  $H$  relates the measurement vector and the state

vector. The desired border is sampled across  $M$  points of the border location in polar coordinates with fixed angle location so that only the radial coordinate needs to be predicated. The state vector has three components, i.e., location  $y_i$ , velocity  $\dot{y}_i$  and acceleration  $\ddot{y}_i$ , which can be defined as:

$$x_k = [y_1 \dots y_M, \dot{y}_1 \dots \dot{y}_M, \ddot{y}_1 \dots \ddot{y}_M]^T \quad (5.5)$$

The prediction phase is to estimate the prior state  $\hat{x}_k^-$  and its covariance matrix  $P_k^-$  according to the motion model:

$$\begin{aligned} \hat{x}_k^- &= A\hat{x}_{k-1}, \\ P_k^- &= AP_{k-1}A^T + Q. \end{aligned} \quad (5.6)$$

At the measurement phase, the posterior state  $\hat{x}_k$  is computed by correcting the prior state  $\hat{x}_k^-$  based on the current observation of the border  $z_k$  and controlled by the Kalman gain  $K$ :

$$\begin{aligned} \hat{x}_k &= \hat{x}_k^- + K(z_k - H\hat{x}_k^-), \\ K &= P_k^- H^T (HP_k^- H^T + R)^{-1}, \\ P_k &= (1 - KH)P_k^-. \end{aligned} \quad (5.7)$$

The observation  $z_k$  is obtained by using a proposed temporal segmentation model without including the shape prior part for efficiency. Since the prediction and measurement processes are linear, we can simply use the linear Kalman filter.

### 5.3.2 Temporal graph construction

The Kalman measurement is acquired by temporal graph cut segmentation, in which new inter-frame/inter-column arcs are defined between the two adjacent frames. These arcs are working as hard constraints to control the maximum distance  $\Delta_{p_{k-1}, p_k}$  at column  $p$  between the initial border  $S^*$  of frame  $k$  and the final border  $S$  of frame  $k-1$ , so that  $|S_k^*(p) - S_{k-1}(p)| \leq \Delta_{p_{k-1}, p_k}$ . The value of  $\Delta_{p_{k-1}, p_k}$  is adapted based on the classification result in frame  $k$ , to allow a small movement distance when any kind of artifacts is detected (i.e., guide-wire, stent, fibrotic and calcification in IVUS, and guide-wire, stent in OCT) and a large movement distance otherwise. An example of the temporal graph construction is shown in Figure 5.1.

To incorporate the Kalman predicated border  $\hat{S}$  into the proposed graphically based model. We define a convex function between the two adjacent frames so that the energy function is defined as following:

$$E_T = \sum_{(p_{k-1}, p_k) \in \mathcal{N}_t} f_t(S_{k-1}(p) - S_k(p)), \quad (5.8)$$

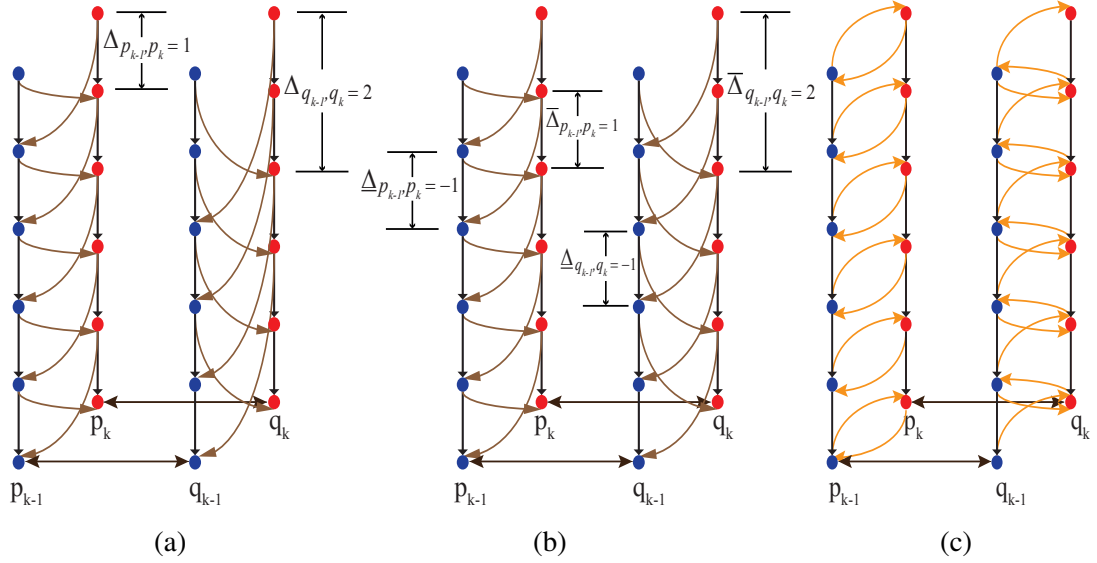


Figure 5.1: Example temporal graph construction between two frames  $k - 1$  and  $k$  for the corresponding columns  $p$  and  $q$ . (a) inter-frame arcs (brown) for the initial segmentation, where  $\Delta_{p_{k-1}, p_k} = 1$ , and  $\Delta_{q_{k-1}, q_k} = 2$ . (b) inter-frame arcs (brown) adapted by the Kalman predicted border, assuming that  $\bar{\Delta}_{p_{k-1}, p_k} = 1$ ,  $\Delta_{p_{k-1}, p_k} = -1$ , and  $\bar{\Delta}_{q_{k-1}, q_k} = 2$ ,  $\Delta_{q_{k-1}, q_k} = -1$ . (c) smoothness arcs (orange) for the same columns when  $f'_{t_{p_{k-1}, p_k}}(0) = 0$  and  $f'_{t_{q_{k-1}, q_k}}(0) = 1$ .

where  $f_t(h) = \eta_3(h - \mu_{p_{k-1}, k})^2$  is penalising abrupt changes between the same columns  $p$  in two adjacent frames  $k - 1, k$  in the set  $\mathcal{N}_t$  of all columns in two adjacent graphs. The arcs between the two frames are defined as described in Section 4.4.1, where  $\mu_{p_{k-1}, k}$  is the difference between the Kalman posterior estimation of border  $\hat{S}$  in the current frame  $k$  and the final border segmentation in the previous frame  $k - 1$ . The inter-frames constraint is defined as  $\bar{\Delta}_{p_{k-1}, p_k} = \mu_{p_{k-1}, k} + w \cdot \sigma_{p_{k-1}, k}$ ,  $\Delta_{p_{k-1}, p_k} = \mu_{p_{k-1}, k} - w \cdot \sigma_{p_{k-1}, k}$ , where  $w$  is a real constant and  $\sigma_{p_{k-1}, k}$  is defined based on the Kalman covariance  $P_k$ .

### 5.3.3 Cost function and graph cut

The final segmentation is then obtained by minimising the three energy functions (4.2), (4.7), and (5.8) representing the classification-based cost function, the shape prior model, and the temporal graph constraints respectively. The temporal segmentation without using the Kalman filter is used to derive the shape prior model. To make the Kalman filter more consistent, the final segmented border is used to update the measurement process. This process is known in literature [301] as a sequential Kalman filter. Note, the final border segmentation for frame

$k - 1$  is not changed after segmenting the frame  $k$ . This can be achieved by redefining the cost function  $\mathcal{C}_B(x, y)$  for frame  $k - 1$  so that negative infinite cost is assigned to the nodes  $V(x, y)$  corresponding to the border in frame  $k - 1$  and the remaining nodes are assigned value one. In other words, we connect the nodes just above the border to the sink and the border nodes themselves to the source, both with infinite weight, so that the result of the minimum closed set graph for frame  $k - 1$  is fixed.

### 5.3.4 Experimental results

The proposed spatio-temporal segmentation method is tested on both IVUS and OCT datasets. The datasets are described in Chapter 4, i.e., the IVUS dataset contains 33,220 images representing almost the entirety of 10 *in vivo* pullbacks acquired by a 40 MHz transducer Boston Scientific ultrasound machine with Atlantis SR Pro Catheter and manual labelling was carried out on every 10th frame, i.e., 3322 frames, whilst the OCT dataset contains 1,826 images for 8 *in vivo* pullbacks acquired from a C7-XR LightLab Imaging system. The segmentation for the first frame is achieved by using the proposed shape prior model as described in Chapter 4. For columns classified as normal/soft plaque, the  $\Delta_{p_{k-1}, p_k}$  set to 40 pixels, otherwise  $\Delta_{p_{k-1}, p_k} = 25$ .

Here, we present the results of the proposed classification-based segmentation discussed in Chapter 4 and the proposed spatio-temporal method. Table 5.1 shows the quantitative comparison between the two methods. The classification-based segmentation relies on the classification result to formulate the cost function and segmenting each frame without taking either the shape prior model or the temporal information in consideration. It clearly shows that the proposed spatio-temporal method improves significantly the performance of the segmentation framework, e.g., the Hausdorff distance for the spatio-temporal method is 19.23 compared to 25.11 for classification-based method. Comparing to Table 4.2 presented in Chapter 4, the proposed spatio-temporal method outperforms all other IVUS segmentation methods, i.e., the Texture-RBF method [27], star graph cut [1], and optimal surface method [8] applied on 2D images. Table 5.2 shows the quantitative results of OCT images. The proposed method achieved superior performance in segmenting the lumen border in OCT.

Figures 5.2, 5.3, and 5.4, show typical examples of the longitudinal views of eight different pullbacks of IVUS and five different OCT pullbacks. The proposed method provides much more temporal coherent segmentation across all pullbacks and significantly reduce the abrupt change of the border. Rows (a,b,c,d, and f) show clearly the benefit of the temporal constraints

Table 5.1: IVUS quantitative results of the proposed spatio-temporal method. AMD: Absolute Mean Difference(pixel); HD: Hausdorff Distance(pixel); AO: Area Overlap(%); Sens.: Sensitivity(%); Spec.: Specificity(%).

|                                   | AMD         | HD           | AO           | Sens.        | Spec.        |
|-----------------------------------|-------------|--------------|--------------|--------------|--------------|
| Classification-based segmentation | 8.11        | 25.15        | 93.72        | 95.95        | 97.15        |
| Proposed spatio-temporal method   | <b>6.46</b> | <b>19.23</b> | <b>94.97</b> | <b>96.60</b> | <b>98.01</b> |

Table 5.2: OCT quantitative results of the proposed spatio-temporal method. AMD: Absolute Mean Difference(pixel); HD: Hausdorff Distance(pixel); AO: Area Overlap(%); Sens.: Sensitivity(%); Spec.: Specificity(%).

|                                   | AMD         | HD           | AO           | Sens.        | Spec.        |
|-----------------------------------|-------------|--------------|--------------|--------------|--------------|
| Classification-based segmentation | 4.14        | 13.69        | 93.90        | 94.28        | 99.82        |
| Proposed spatio-temporal method   | <b>3.26</b> | <b>11.01</b> | <b>95.15</b> | <b>95.55</b> | <b>99.84</b> |

compared to single frame segmentation. The abrupt changes of border may happen due to misclassification of the columns, weak features retrieved from the border, or small vessels called perivascular surrounding the adventitia that have similar edge characteristics. Both methods achieved similar performance on the normal arterial area and for columns that are classified correctly. For OCT segmentation, the proposed spatio-temporal method maintains coherent segmentation, despite the residual blood and bifurcation as shown in Rows (a,c d and e) of Figure 5.4.

## 5.4 Tracking Through HMM Modelling

As mentioned earlier, the proposed segmentation method needs two steps to obtain the final border. In the first step, the initial cut based on the optimisation of the classification-based cost function is achieved, that serving as a basis for further processing, while incorporating both shape prior model and temporal constraints are the second step toward an accurate delineation of the border. Here, we introduce an alternative approach to find the final border, by combining a classification-based cost function optimisation, shape prior and temporal information based

## 5. Longitudinal Tracking and Segmentation

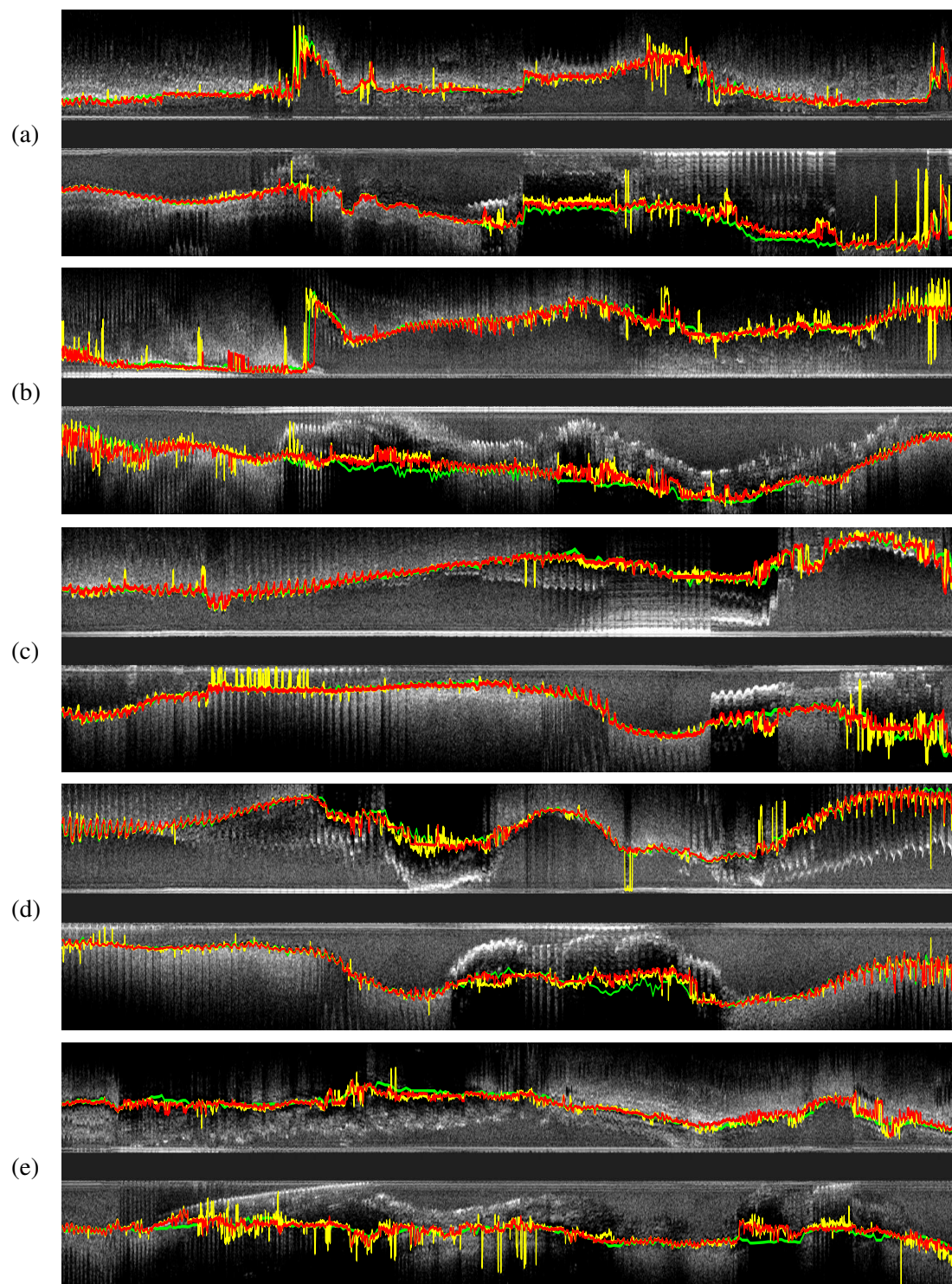


Figure 5.2: Longitudinal view for five different pullbacks, the proposed spatio-temporal (red), the classification-based method (yellow) and groundtruth (green).

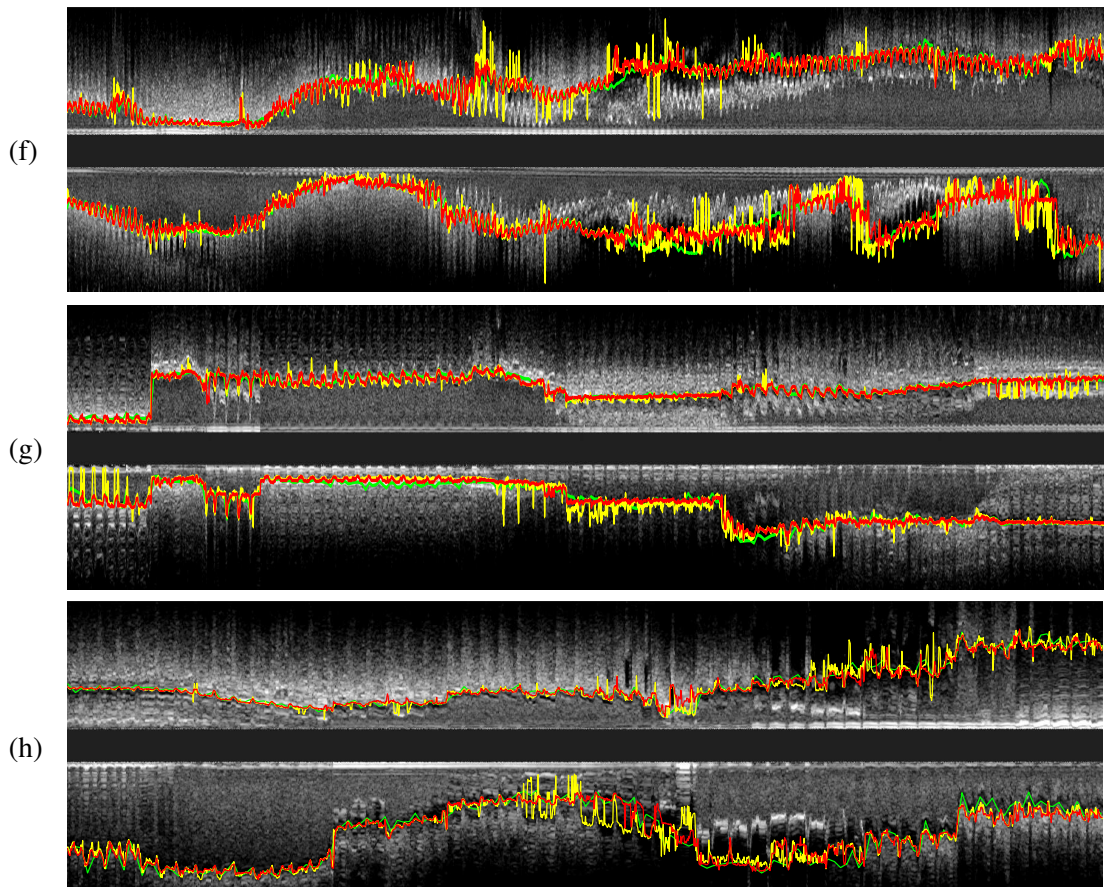


Figure 5.3: Longitudinal view for three different pullbacks, the proposed spatio-temporal (red), the classification-based method (yellow) and groundtruth (green).

on the HMM and without the need to define the Kalman filter or constructing any additional graphs.

In this work, HMM is proposed to track and segment the border across frames. The border  $S$  is approximated by using the RBF function where the hidden states of the HMM model are referred to the potential RBF centres. The border is evenly sampled into  $M$  points and at each point line segment is drawn perpendicular to the tangent line of the border where each line segment has  $K$  points. The index of contour RBF centres is  $\phi = 1, \dots, M$  and the index of each normal line is  $\psi = 1, \dots, K$  where  $K$  is an odd number. The initial RBF centres are defined from the previous frame and located as the centre of normal line  $\psi = (K + 1)/2$  as shown in Figure 5.5. The normal line restricts the search space for the predicated contour to be within

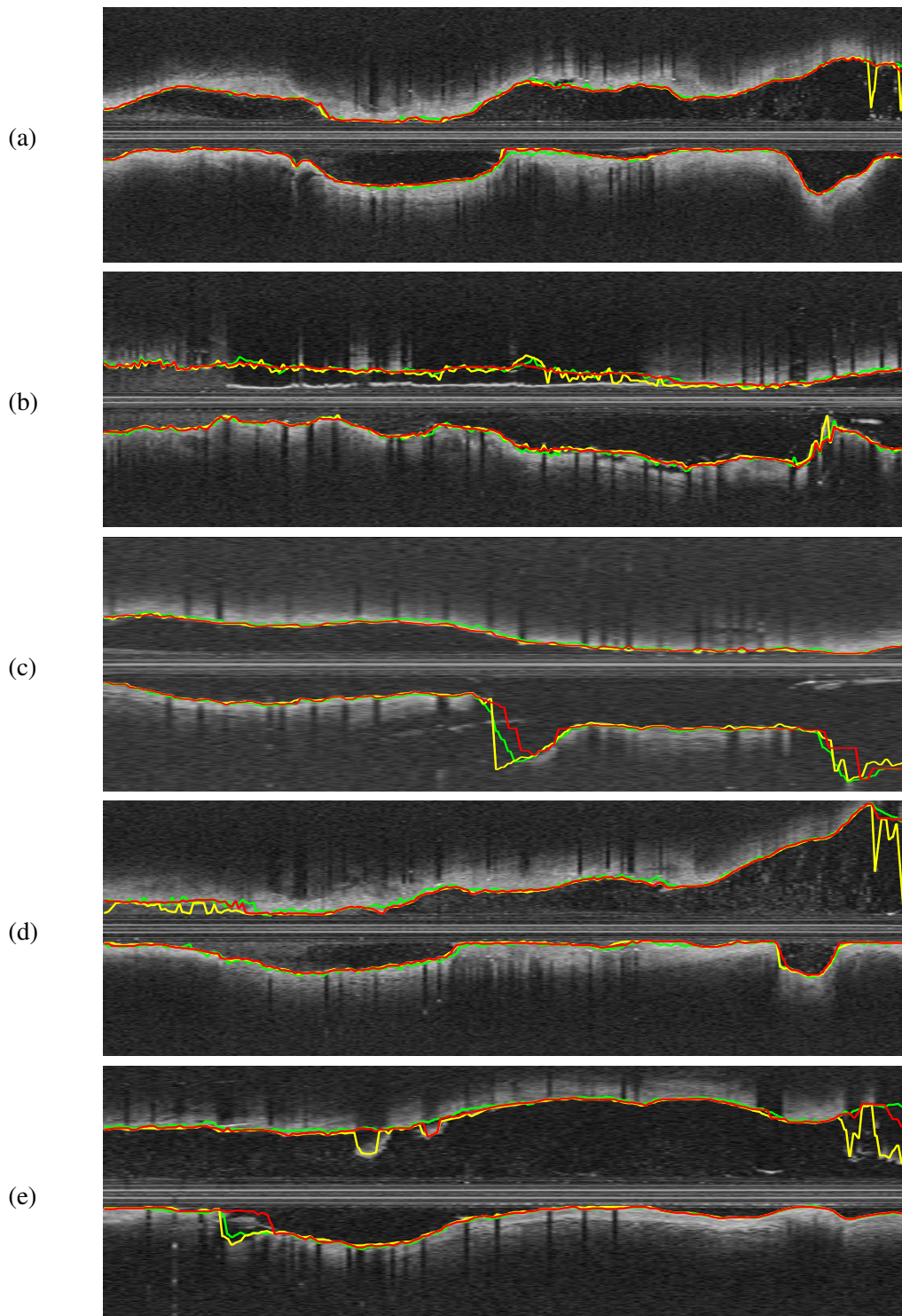


Figure 5.4: Longitudinal view for five different OCT pullbacks, the proposed spatio-temporal (red), the classification-based method (yellow) and groundtruth (green).

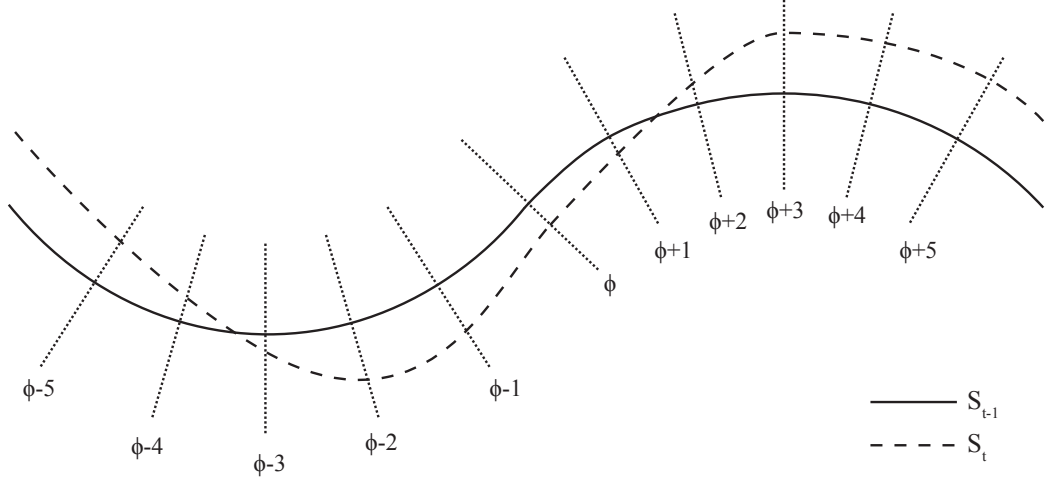


Figure 5.5: An example of border segmentation  $S_t$  based on the border  $S_{t-1}$  obtained in the previous frame using the proposed HMM Model. The border is divided into  $M$  points and at each point a normal line is drawn with length  $K$ . The final border is interpolated using RBF.

$(K - 1)/2$  point distance from the initial contour.

We denote to all possible sequences of hidden states by  $Q = \{q\}$ , where  $q = \{q_1, \dots, q_\phi, \dots, q_M\}$  is one possible state sequence and  $q_\phi$  is the state on the normal at  $\phi$ . These sequences correspond to possible RBF centre locations. The HMM observations  $O = \{O_1, \dots, O_\phi, \dots, O_M\}$  are extracted from the normal lines. HMM is specified by three probability measures  $\lambda = (A, B, \pi)$ , where  $A, B$  and  $\pi$  are the probabilities for the transition, emission and initial state. The transition between states  $q$  at two normals  $\phi$  and  $\phi + 1$  are governed by a set of probabilities called transition probabilities  $P(q_\phi | q_{\phi+1})$  and any state can only be observed by an output event according to associated probability distribution called emission probabilities  $P(O_\phi | q_\phi)$ . The output event is the image features extracted from each state at the normal.

Here, we investigate the use of both state and arc emission based on the observation extracted from the proposed classification-based cost function and the shape prior model. In fact, the arc-emission [302] is a generalised form of the state-emission. When the observation is emitted from only a single state, it is called state-emission. The observation can also be emitted depending on a pair of states, known as arc-emission.

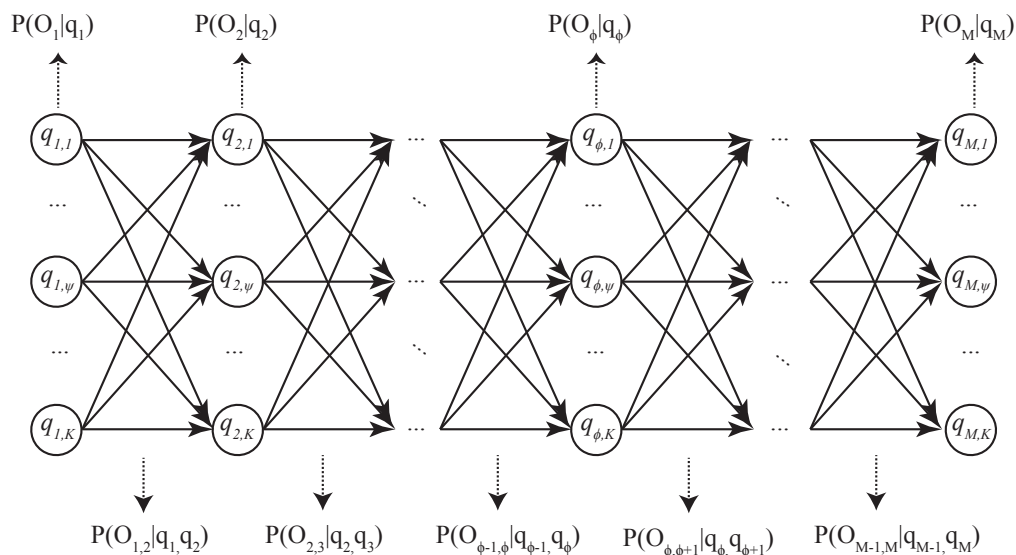


Figure 5.6: HMM construction. The state-emission is illustrated in the upper part, whilst the arc-emission in the lower part. The arcs between the states are carrying the transition probabilities.

### 5.4.1 Transition probability

In [303], the authors used smoothness constraints to define the transition probability that favours small displacements from the initial contour, i.e., it limits the deformation ability for the contour. In [293], the authors used region and smoothness constraints. They assumed that the object is opaque and the segmented foreground and background regions have different appearances, however, it could be disrupted by background clutter. In [295], authors compute transition probabilities by modelling the amount of bending between the normal lines and the displacement of contour position with respect to the previous frame using two Gaussian distributions and defining weighted coefficients for each transition. A fixed point iterative method is used to find the optimal value of these coefficients.

Baum-Welch and Viterbi training are popular estimation methods for the HMM parameters  $(A, B, \pi)$ . The Viterbi training is an approximation of the Baum-Welch method and is computationally much faster, however, it may perform less well compared to the Baum-Welch method. In this work, we use the Baum-Welch (Forward-Backward) algorithm [292] to define both the transition and prior probabilities. The Baum-Welch algorithm is a special case of

the Expectation-Maximisation method. We define the probability of traversing from state  $i$  at normal  $\phi$  to state  $j$  at normal  $\phi + 1$ , where  $1 \leq \phi \leq M$  and,  $1 \leq i, j \leq K$  as:

$$\xi_{\phi}(i, j) = P(q_{\phi} = i, q_{\phi+1} = j | O, \lambda), \quad (5.9)$$

This definition can be written by using forward and backward variables as:

$$\xi_{\phi}(i, j) = \frac{\alpha_{\phi}(i) a_{ij} b_j(O_{\phi+1}) \beta_{\phi}(j)}{\sum_{i=1}^K \sum_{j=1}^K \alpha_{\phi}(i) a_{ij} b_j(O_{\phi+1}) \beta_{\phi}(j)} \quad (5.10)$$

where  $\alpha_{\phi}(i)$  and  $\beta_{\phi}(j)$  are the forward and backward variables for state  $i$  and  $j$  respectively.  $b_j(O_{\phi+1})$  is the emission probability and it is measured by  $P(O_{\phi+1} | q_j)$  or  $P(O_{\phi, \phi+1} | q_i, q_j)$  for state-emission or arc-emission respectively. The probability of being in state  $i$  at normal  $\phi$  is given by:

$$\gamma_{\phi}(i) = \sum_{j=1}^K \xi_{\phi}(i, j). \quad (5.11)$$

The summation of  $\gamma_{\phi}(i)$  over all normals is interpreted as the expected number of transitions from state  $i$ , while the summation of  $\xi_{\phi}(i, j)$  over all normals is the expected number of transitions from state  $i$  to state  $j$ . The expected initial state distribution at the first normal  $\phi = 1$  is defined as:

$$\hat{\pi}_i = \gamma_{\phi_1}(i), \quad (5.12)$$

and the expected transition probability is given as:

$$\hat{a}_{ij} = \frac{\sum_{\phi=1}^{M-1} \xi_{\phi}(i, j)}{\sum_{\phi=1}^{M-1} \gamma_{\phi}(i)} \quad (5.13)$$

Note the observation probability  $B$  is already computed as described in Section 5.4.2 and there is no need for it to be re-estimated. The process is iterated and each of iterations increases the likelihood of the data  $P(O | \hat{\lambda}) \geq P(O | \lambda)$  until convergence.

### 5.4.2 Emission probability

We use a similar method to describe the emission probability as presented in [295, 294]. Image observations are modelled by two probability density functions: one for the contour and the

other for the background. Let  $O_\phi = \{o_{\phi,1}, \dots, o_{\phi,\psi}, \dots, o_{\phi,K}\}$  be a set of features along the normal  $\phi$  and  $o_{\phi,\psi}$  one feature extracted from point  $\psi$  on the line.  $P(o_{\phi,\psi}|FG)$  and  $P(o_{\phi,\psi}|BG)$  represent the probabilities of that feature belonging to the contour and the background respectively. The state-emission probability is defined as:

$$P(O_\phi|q_\phi) \propto P(o_{\phi,\psi}|FG) \prod_{\psi \neq q_\phi} P(o_{\phi,\psi}|BG). \quad (5.14)$$

The likelihood of the observed variables  $O_\phi$  from a state  $q_\phi$  is achieved by measuring the likelihood of each feature  $o_{\phi,\psi}$  at index  $\psi$  of the line  $\phi$  to belong to the contour and all the rest of features on that line belong to the background.

For the arc-emission, the set of all arc-observation is defined as  $O = \{O_{\phi,\phi'}\}$ , where  $O_{\phi,\phi'} = \{o_{\phi_1,\phi'_1}, \dots, o_{\phi_\psi,\phi'_\psi}, \dots, o_{\phi_K,\phi'_K}\}$ . The feature vector  $O_{\phi,\phi'}$  is extracted between two adjacent lines  $\phi$  and  $\phi'$ . The arc-emission probability is given by:

$$P(O_{\phi,\phi'}|q_\phi, q_{\phi'}) \propto P(o_{\phi,\phi'}|FG) \times \prod_{\psi, \psi' \neq q_\phi, q_{\phi'}} P(o_{\phi,\phi'}|BG). \quad (5.15)$$

From a set of training data with a manually labelled contour, we extract features that correspond to the contour and the background and use it to learn the parameters, mean and variance of two Gaussian distributions  $FG$  and  $BG$ .

### 5.4.3 Cost function

The inference of the HMM hidden states can be achieved with the help of a set of observations. These observations determine the potential position of the RBF centres. The observation is obtained from pixel intensity, image features such as edge, ridge, colour distribution of the object, or shape prior. In [303], the authors used edge-based features to define the observation probability by detecting all possible edges along the normals assuming that the noise is a Poisson process to maximise the probability of the state with less edge localisation error. However it relies significantly on edges. In [293, 294], the authors combined edge with region-based features by defining two histograms for object and background colour distributions. However, assuming that the object has discriminative distribution is not always applicable and the image noise can change object colour distribution. In [295], a Hessian matrix is used to highlight microtubules in a live cell. However, the calculation of these features is based on the local

orientation between every two states in two adjacent normal lines, which increases the computational time of defining the arc-emission with a growing number of hidden states.

In this work, we propose to extract the observation from our classification-based cost function  $\mathcal{C}_B$  and the shape prior model  $\mathcal{C}_P$  presented in Chapter 4. The cost function is inversely proportional to the likelihood of each pixel in the image domain belonging to the border of interest. Each cost function is normalised by unit variance to facilitate its combination so that:

$$\mathcal{C}(x, y) = \mathcal{C}_B(x, y) + \mathcal{C}_P(x, y). \quad (5.16)$$

Hence, the two probability distributions  $FG$  and  $BK$  are estimated from the cost function  $\mathcal{C}$  from the training data. The observation of state-emission  $o_{\phi, \psi}$  is defined as the following:

$$o_{\phi, \psi} = \mathcal{C}(\mathbf{x}_{\phi, \psi}), \quad (5.17)$$

where  $\mathbf{x}_{\phi, \psi}$  is the corresponding location in the image domain for the state defined on the normal  $\phi$  at index  $\psi$ . For the arc-emission, the observations are obtained between every two consecutive lines:

$$o_{\phi_{\psi}, \phi'_{\psi}} = \mathbb{E}[\mathcal{C}(\mathbf{x}_{\phi_{\psi}, \phi'_{\psi}})], \quad (5.18)$$

where  $\mathbb{E}$  is the mean operation of the extracted cost, and  $\mathbf{x}_{\phi_{\psi}, \phi'_{\psi}}$  is the interpolated line index between the normals  $\phi$  and  $\phi'$ . The complexity of the observation extraction for state-emission HMM is  $O(MK)$ , whilst for arc-emission it is  $O(MK^2)$  where  $M$  is the total number of normal lines and  $K$  is the number of points along these normals.

#### 5.4.4 Viterbi algorithm

The optimal sequence of states  $q^*$  can be efficiently found by applying the Viterbi algorithm, given the image observation  $O_t$ , and HMM model  $\lambda$ :

$$q^* = \underset{q \in Q}{\operatorname{arg\,max}} P(q|O_t, \lambda). \quad (5.19)$$

The corresponding sequence of RBF centres in the image domain is defined based on a mapping function of the optimal states  $q^*$  and the RBF centre locations computed at the previous frame  $t - 1$ . The final border  $S$  at frame  $t$  is interpolated by the RBF equation (5.1). The running time complexity of the Viterbi algorithm in both state-emission and arc-emission HMM is  $O(MK^2)$ .

Table 5.3: OCT quantitative comparison. HD: Hausdorff distance (pixel).

|   | HD          |
|---|-------------|
| Arc-emission with Baum-Welch Training   | <b>9.84</b> |
| Arc-emission with Viterbi Training      | 9.98        |
| State-emission with Baum-Welch Training | 10.81       |
| State-emission with Viterbi Training    | 11.38       |
| State-emission with Online Training     | 11.83       |

### 5.4.5 Experimental results

The proposed method is evaluated on both OCT and IVUS. In OCT, we have 10 *in vivo* pullbacks acquired from a C7-XR LightLab Imaging system. We randomly select 3 pullbacks to train the HMM and 7 pullbacks to test (i.e., 1617 frames). For IVUS, we randomly select 2 pullbacks for HMM training and 8 pullbacks for testing (i.e., 26,390 images) and the evaluation was carried out on every 10th frame.

#### OCT

The number of RBF centre is set to 51 which are evenly sampled. The normal line segment length is 81 pixels. Table 5.3 shows a comparison between different training methods using state and arc emission for the HMM model based on the combination of classification-based cost function and shape prior on OCT data. The Hausdorff distance between the segmented border and the manual labelling are used as a measurement of the maximum distance between points of the automatic segmentation set and the groundtruth. Our experiments show that the arc-emission is better than the state emission in both training schemes. Baum-Welch training outperforms the Viterbi training. Both algorithms converge after a few numbers of iteration (less than 30 iterations). We also show that an online training method is feasible by using the on-the-fly computation of the arc-emission probabilities between every two states across the whole border to adapt the transition probabilities combining with a smoothness term to reduce the effect of the outliers transition. In this case, the state-emission is used as emission probabilities. The result shown is promising and is close to the data-driven training methods.

A comparison of different configurations of the cost function with the HMM is shown in Table 5.4. Five different evaluation metrics were used for quantitative analysis: absolute mean difference, Hausdorff distance, area overlap, sensitivity and specificity. The HMM is tested with a

Table 5.4: OCT quantitative comparison. AMD: absolute mean difference(pixel); HD: Hausdorff distance(pixel); AO: area overlap(%); Sens.: sensitivity(%); Spec.: specificity(%).

|                                    | AMD         | HD           | AO           | Sens.        | Spec.        |
|------------------------------------|-------------|--------------|--------------|--------------|--------------|
| HMM with Region cost               | 34.81       | 80.63        | 51.36        | 52.71        | 99.37        |
| HMM with Edge cost                 | 5.02        | 21.45        | 92.75        | 93.23        | <b>99.80</b> |
| HMM with classification-based cost | <b>4.41</b> | <b>16.69</b> | <b>93.49</b> | <b>95.85</b> | 99.11        |

Table 5.5: OCT quantitative comparison. AMD: absolute mean difference(pixel); HD: Hausdorff distance(pixel); AO: area overlap(%); Sens.: sensitivity(%); Spec.: specificity(%).

|   | AMD         | HD          | AO           | Sens.        | Spec.        |
|---|-------------|-------------|--------------|--------------|--------------|
| Star Graph cut [1]                                | 5.69        | 21.54       | 91.75        | <b>96.73</b> | 98.09        |
| Spatio-temporal method                            | 3.18        | 10.72       | 95.33        | 95.72        | <b>99.85</b> |
| State-emission HMM with star and shape prior cost | 3.10        | 10.81       | 95.37        | 95.84        | 99.81        |
| Arc-emission HMM with star and shape prior cost   | <b>2.99</b> | <b>9.84</b> | <b>95.46</b> | 95.96        | 99.80        |

region-based cost using discrete Chan-Vese function [8] and edge-based cost function defined by the equation (4.6), however, these cost functions do not cope well toward image artifacts and discontinuities in the lumen border. The classification-based cost function outperforms those cost functions as it builds on the transition probabilities to expect the border location in the occlusion caused by image artifacts. Note, for simplicity, state emission is used in these HMMs. In Table 5.5, the shape prior model is combined with the classification-based cost function for improved performance. The initial segmentation is obtained by using the graph-based method introduced in Chapter 4 without temporal constraints. The table shows results for both state and arc emissions. The result of the proposed spatio-temporal method using the Kalman filter and star graph cut [1] are also shown on the same testing set. Our proposed HMM methods outperform the star graph cut. On these datasets, the arc-emission HMM achieved the best result compared to all other methods.

Figures 5.7 and 5.8, show the longitudinal view of four pullbacks for the proposed state and arc HMM methods respectively. Both methods show good behaviour on treating the bifurcation and blood residual. However, arc emission HMM is utilising the local evaluation of the observations between every two states along the direction of transition to surpass the state emission.

For the qualitative comparison to the proposed spatio-temporal method, Rows (a,b,c, and d) in Figures 5.7 and 5.8 correspond to Rows (a,c,d, and e) in Figure 5.4. The results of the two methods are comparable.

### IVUS

In IVUS, the proposed methods are used to segment the outer wall of the vessel, i.e., the media-adventitia border. The proposed method normal lines have a length of 101 pixel with 51 RBF centres in polar coordinates. Table 5.6 shows a comparison between the Texture-RBF method [27], the star graph [1] and our proposed HMM methods. In the Texture-RBF method, Papadogiorgaki *et al.* used RBF to smooth the initial contour obtained by thresholding on discrete wavelet frames. For the star graph [1], the user has to add some seed points for the object and background to achieve reasonable results. The proposed HMM methods clearly outperform these methods. The comparison between state and arc emission HMMs is shown in the table. State emission is marginally better, where the Hausdorff distance and area overlap are 19.05 and 94.78% compared to 19.25 and 94.54% for the arc emission respectively. The sensitivity and specificity for detecting the vessel area are 96.73% and 97.71% for state emission and 96.77% and 97.38% for arc emission. The transition probabilities are trained based on the Baum-Welch algorithm. Also, our spatio-temporal method is outperforming the HMM methods with better specificity of 98.03% and area overlap 94.95%. However, the arc and state emission HMM methods can be improved by optimising the cost function, e.g., increasing the accuracy of the classifier and also adding some temporal constraints on the initial segmentation for more robust shape prior.

The longitudinal view of the state and arc emission are shown in Figures 5.9 and 5.10. Both methods produce comparable results. However, in some situations, the arc emission is inconsistently oscillated due to its high sensitivity to the extracted features. For qualitative comparison to the proposed spatio-temporal method, Rows (b, c, e and f) in Figures 5.2 and 5.3 correspond to Rows (a, b, c, and d) in Figures 5.9 and 5.10 for the state and arc emissions respectively.

### 5.5 Summary

We present two tracking and segmentation methods that exploit the temporal information in order to segment the cross-sectional IVUS and OCT images more coherently. The border

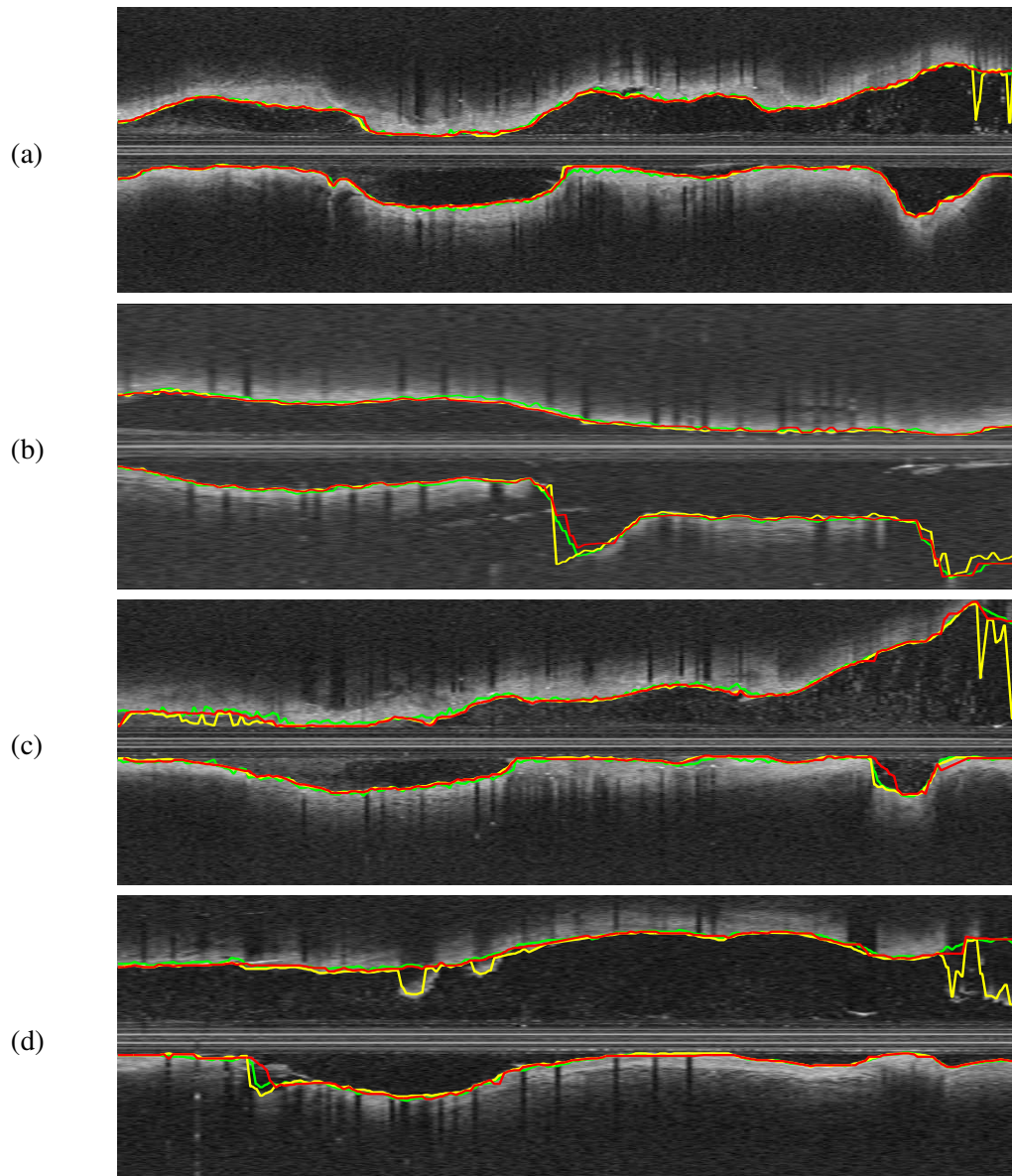


Figure 5.7: Longitudinal view for four different OCT pullbacks, the proposed state-emission HMM (red), the classification-based method (yellow) and groundtruth (green).

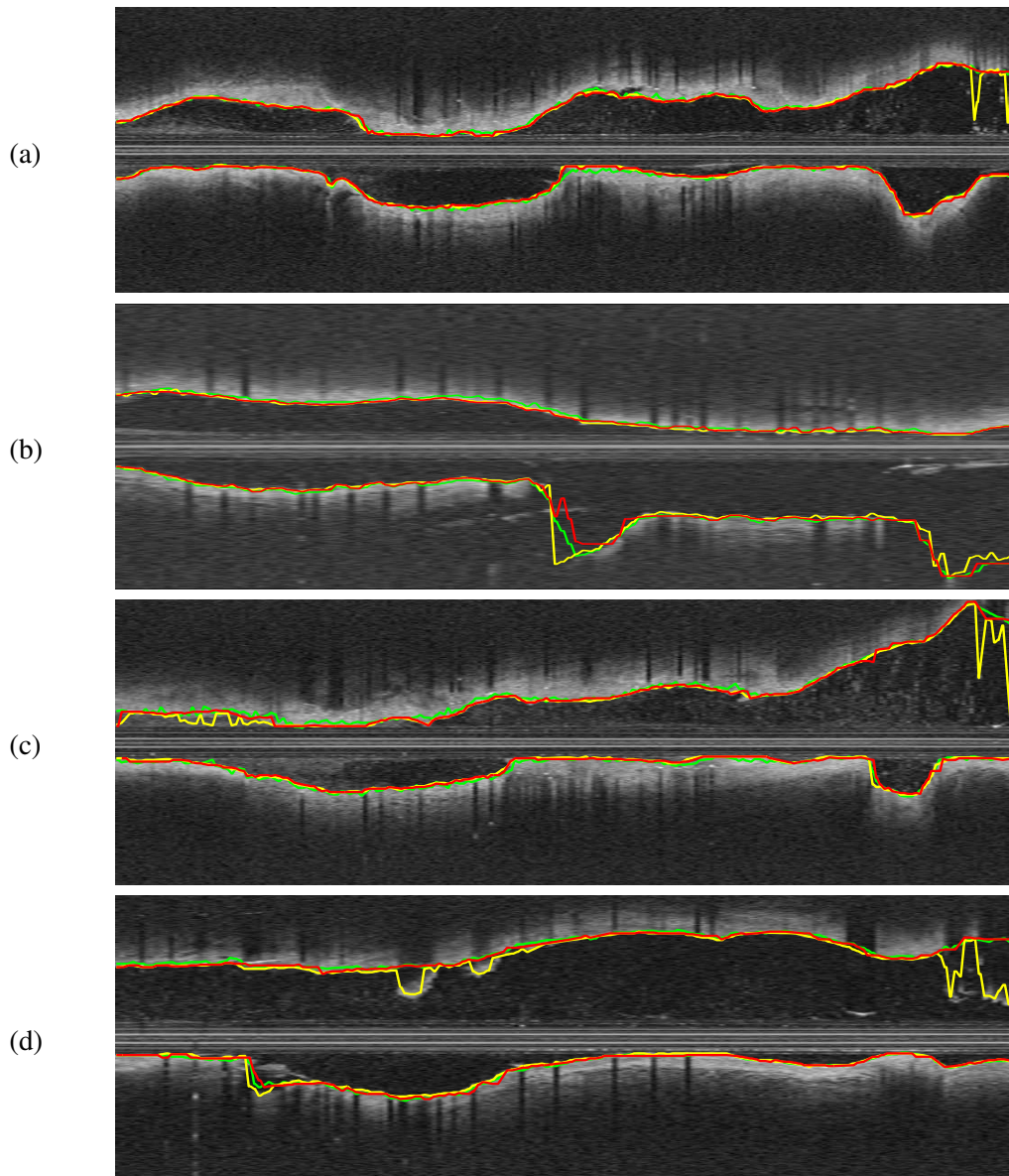


Figure 5.8: Longitudinal view for four different OCT pullbacks, the proposed arc-emission HMM (red), the classification-based method (yellow) and groundtruth (green).

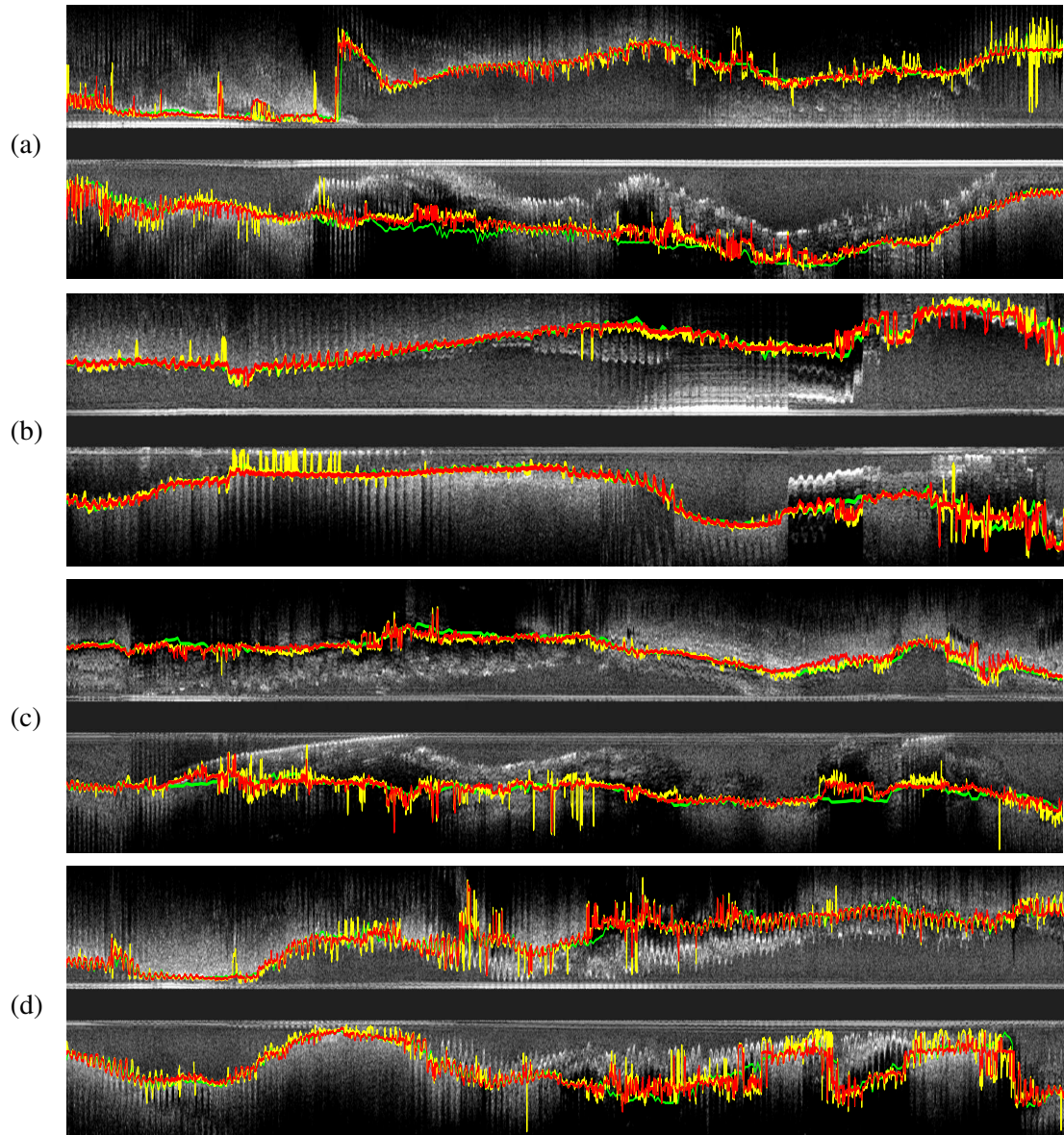


Figure 5.9: Longitudinal view for four different IVUS pullbacks, the proposed state-emission HMM (red), the classification-based method (yellow) and groundtruth (green).

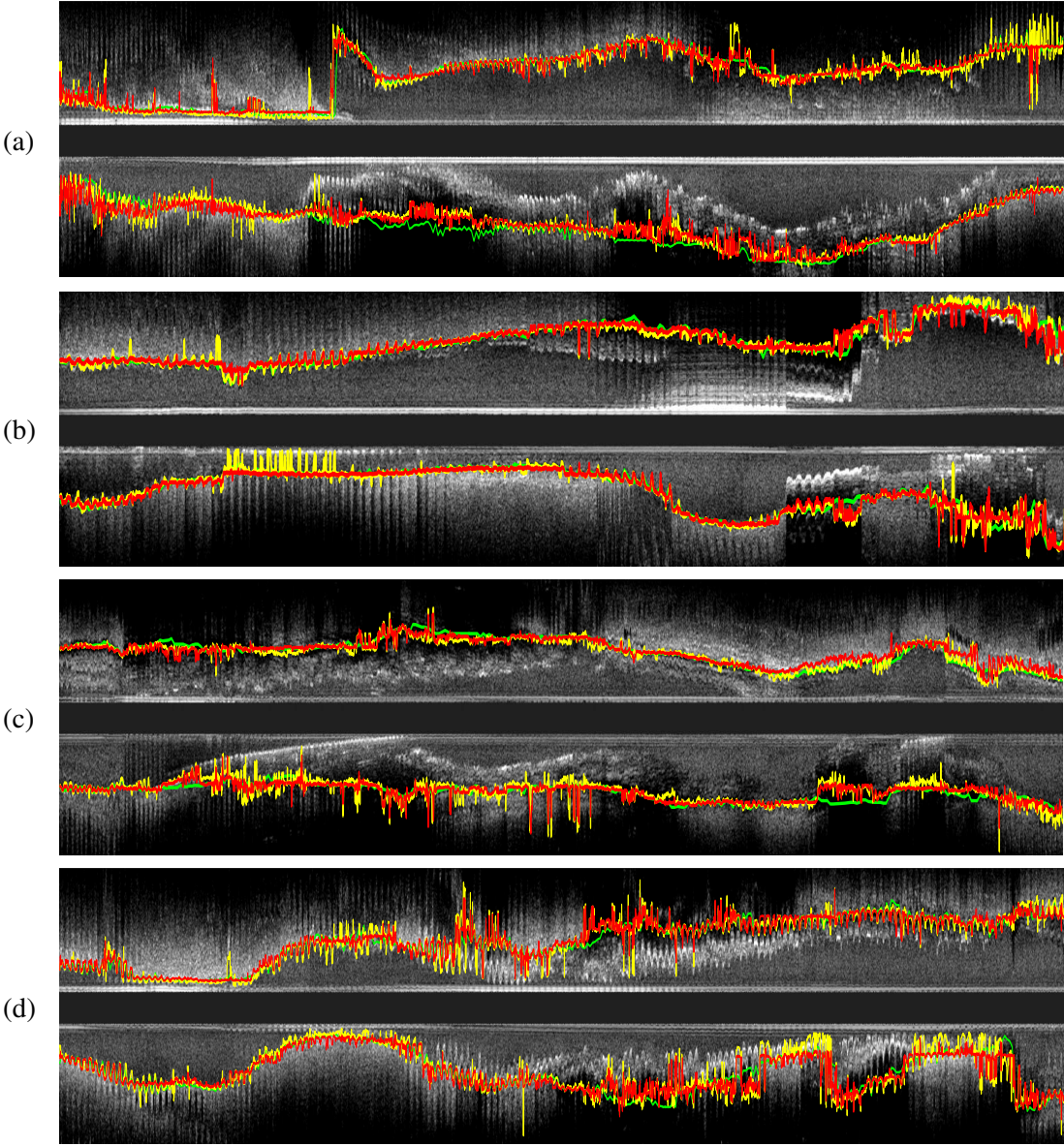


Figure 5.10: Longitudinal view for four different IVUS pullbacks, the proposed arc-emission HMM (red), the classification-based method (yellow) and groundtruth (green).

Table 5.6: IVUS quantitative comparison. AMD: absolute mean difference(pixel); HD: Hausdorff distance(pixel); AO: area overlap(%); Sens.: sensitivity(%); Spec.: specificity(%).

|   | AMD         | HD           | AO           | Sens.        | Spec.        |
|---|-------------|--------------|--------------|--------------|--------------|
| Texture-RBF method [27]                           | 21.93       | 50.72        | 83.38        | 87.54        | 95.88        |
| Star graph cut [1]                                | 14.07       | 38.48        | 89.43        | 94.67        | 93.54        |
| Spatio-temporal method                            | <b>6.40</b> | 19.39        | <b>94.95</b> | 96.62        | <b>98.03</b> |
| State-emission HMM with star and shape prior cost | 6.66        | <b>19.06</b> | 94.78        | 96.73        | 97.71        |
| Arc-emission HMM with star and shape prior cost   | 7.01        | 19.25        | 94.54        | <b>96.77</b> | 97.38        |

is parameterised by a few RBFs which effectively minimise the computational complexity for the tracking. A spatio-temporal method using a Kalman filter is proposed. The node-weighted directed graph is extended on two consecutive cross-sectional frames with embedded shape constraints within individual frames and between consecutive frames. A Kalman filter is used to predicate the border location in the next frame which is integrated by adapting new constraints to impose consistent tracking of the interesting border across multiple frames.

HMM based border tracking method is also proposed. The method searches for the border along a set of normal lines based on the segmentation of the previous frame. The emission probabilities are defined based on two probability distributions of the arterial border and background respectively, that are derived directly from both the classification-based cost function and the shape prior model. State and arc configurations of the HMM emission are studied. The optimal sequence of the hidden states corresponds to RBFs of the border and is obtained by using the Viterbi algorithm. The proposed spatio-temporal method performed better than the HMM based tracking methods on IVUS dataset, while the HMM methods outperformed the spatio-temporal method on OCT dataset. The HMM methods are also faster than the spatio-temporal method in terms of finding the final segmented border.

Comprehensive quantitative and qualitative comparisons have shown significant improvements in segmentation accuracy when compared to other segmentation methods.



## Chapter 6

# Conclusions and Future Work

### Contents

---

|     |                         |     |
|-----|-------------------------|-----|
| 6.1 | Conclusions . . . . .   | 109 |
| 6.2 | Contributions . . . . . | 112 |
| 6.3 | Future Work . . . . .   | 113 |

---

### 6.1 Conclusions

The aim of this project was to develop automatic segmentation methods for cross-sectional coronary arterial images, i.e., IVUS and OCT, that can easily incorporate prior and temporal information without any user intervention. Combinatorial optimisation methods are proposed to effectively minimise the energy functions in polynomial time. Designing the cost function is introduced in a novel way by achieving a column-wise classification that shows a superior usefulness to a uniform definition of the cost function to overcome various image artifacts. Shape prior model incorporates a local adaption of the graph construction and global shape constraints defined as a cost function to correct any irregular shape of the segmented vessel. Temporal information is incorporated to ensure coherence among consecutive frames and this is achieved by both the Kalman-based method and HMM for further more improvement of our results.

The preprocessing steps include transforming the images to polar coordinates and removing the catheter artifacts to convert the problem into finding the minimum closed graph and facilitates feature extractions. The vessel border has generally strong edge features which can be high-

lighted by using a steerable derivative of Gaussian, Gabor filter or local phase. However, these extracted features themselves are often distracted by different forms of image artifacts. To delineate the media-adventitia in IVUS images, we proposed a double-interface segmentation method where an auxiliary border is simultaneously searched above the media-adventitia border to reduce the effect of undesirable image features. Graph constraints are adapted between the two interfaces to control the interrelation between them. The cost function is a uniform combination of complementary edge and texture features. The experimental results show better performance by using double-interface segmentation than single interface and conventional graph cut. However, the auxiliary border might response to the media-adventitia border, if the lumen border or any other artifacts are not clearly prominent. For OCT segmentation, single interface segmentation with novel circulation density features is proposed to highlight the lumen border. Circulation density features are extracted from the gradient vector field that results from the global interactions among the original image gradient vectors. To reduce the effect of image noise, a diffusion method is used. The proposed method was compared to three recent deformable models, and the star graph cut method. The experimental results show outstanding performance of the proposed method. However, the proposed method may still be affected by the interference of the image artifacts produced by the guide-wire and stent.

The appearance of the vessel borders in IVUS and OCT is not consistent due to the variety of images artifacts and noise that could completely obscure the visibility of the border. In order to overcome the image artifacts problem, we propose an automatic feature selection optimisation to build a robust cost function. A supervised column-wise classification using Random Forest is performed so that the cost function for each individual columns of pixels is adapted by a different set of features based on the classification labelling. Haar-likes features are extracted to classify the IVUS images into five categories and three categories for OCT that give a better accuracy than using pixel intensities. A superior performance was achieved when using the proposed classification-based cost function than any uniform combination of the cost function.

The refinement of the delineated vessel is achieved both locally and globally by incorporating a shape prior model into the graph construction and by dynamically modifying the cost function. Smoothness arcs are defined between every two neighbouring columns to attain more meaningful initial segmentation. By utilising the initial segmentation and shape prior model, the directed graph is updated to impose more effective shape constraints by adapting the arcs between neighbouring columns to penalise any abrupt changes of the border. The shape prior

is also incorporated into the cost function based on a non-parametric density estimation of the similarity between the initial segmentation and a set of shape templates. The final segmentation is obtained by finding the minimum closed set on the adapted node-weighted graph. We compare the proposed method to the optimal surface segmentation using edge features, the Texture-RBF method, and the star graph cut on a large number of images. The proposed method demonstrates significantly better performance.

A combination of the cross-sectional segmentation and longitudinal tracking is also proposed, in order to increase the efficiency of the arterial border delineation in both IVUS and OCT in the presence of occlusions and image artifacts. The border is parameterised using radial basis functions to reduce the tracking points into a few RBF centres. The proposed spatio-temporal method is using the Kalman filter to predicate the border location in the next frame. The Kalman measurement is achieved by performing a temporal initial segmentation. Inter-frame arcs are defined between two consecutive frames to control the distance between the observed border in the current frame and the previous frame so these constraints are adapted by exploiting the classification result to have appropriate initial segmentation by giving the border more freedom to move far from the border in the previous frame when no image artifacts are detected. The inter-frames constraints is then updated based on the predicated border by Kalman filter to obtain the final segmentation as an energy minimisation of two consecutive closed set graphs. The quantitative statistical result and the qualitative images of the longitudinal view of different pullbacks show significant improvement of our results compared to individual frame segmentation.

The HMM shows to be a competent alternative of the Kalman filter to segment and track the border across image frames. The proposed HMM method is tracking the RBFs that represent the border along a set of normal lines based on the segmentation obtained from the previous frame. The hidden states are referring to the location of the RBF centres. The observation is derived from both the classification-based cost function and the shape prior model. The emission probability is defined directly based on two probability distributions for the arterial border and background respectively. The transition probability is learned by using the Baum-Welch algorithm, whilst the optimal sequence of the hidden states is obtained by using the Viterbi algorithm. The computational time to find the final border using the HMM is faster than the spatio-temporal method. The experiential results show that the transition probability learned by Baum-Welch algorithm is better than Viterbi learning. State and arc emissions give

a comparable performance, while the state-emission is less computationally expensive than the arc-emission. Arc-emission could be used to achieve an online training for the transition probabilities. The proposed HMM based on the classification cost function outperformed both uniform edge or region cost function.

## 6.2 Contributions

The contributions of this thesis are summarised as follows:

1. Double interface segmentation approach. An auxiliary interface is simultaneously segmented with the desired IVUS media-adventitia interface to highlight the border despite of the presence of image artifacts.
2. Circulation density features. Novel features are proposed to delineate the OCT lumen border based on the global interaction of the gradient vector field.
3. Cost function optimisation. A novel column-wise supervised classification is proposed to dynamically formulate the cost function for both IVUS and OCT. Haar-like features are extracted from both horizontal and vertical windows and classified by Random Forest.
4. Shape prior model. Global and local shape prior models are proposed based on the non-parametric similarity between an initial segmentation and a set of shape templates and also on adapting the graph construction locally between every two neighbouring columns to allow learned-based smoothness transition of the border.
5. Spatio-temporal segmentation using the Kalman filter. The Kalman filter is used to provide the temporal information about the border across frames. The measurement of the Kalman filter is defined based on the proposed temporal segmentation of the current frame. The Kalman predicated border is integrated into the system by adding a new set of arcs between every two consecutive frames.
6. HMM tracking and segmentation. HMM is used to segment and track the border by searching for the optimal sequence of the hidden states along a set of normal lines to find the corresponding RBF centres of the desired border. These normal lines are evenly sampled over the border in the polar coordinated images. The emission probability of

the HMM is directly derived from the proposed cost function and shape prior without need to train the model. The final border is interpolated by using radial basis functions.

### 6.3 Future Work

The double-interface segmentation could be adapted to segment the lumen border of IVUS images. However, the prominent blood speckles and the unavailability of the raw radiofrequency signals of these images make it a challenge. A classification-based method may be used to obtain a probabilistic map of the lumen area with respect to our initial segmentation highlights roughly the media-adventitia border which is significantly reducing the area of interest. A different set of features could be investigated for this purpose, e.g., histogram of oriented gradients and texture features, e.g., textons. The proposed column-wise classification could also be adapted to optimise the formulation of the cost function for the lumen border. For instance, in the presence of calcific plaque, fibrotic plaque, and stents, edge features are capable of highlighting the lumen border.

The circulation feature density can be improved more by using more sophisticated diffusion methods to reduce the image clutter. The current method has been tested on a set of natural images and compared to the star graph cut method with minimum user interaction. Only the centre point is required from the user, in order to convert the image into polar coordinates, then the graph is constructed, and the cost function is formulated as zero-crossings of the circulation density feature to segment the object. Figure 6.1 shows some promising results of using circulation density features.

The training of the column-wise classifier, i.e., Random Forest, is still accomplished off-line, however it is sufficient for our purpose in the thesis. It could be improved by allowing online training scheme to increase the flexibility and the accuracy of our methods on a wide different range of images. Saffari *et al.* [304] introduced an online Random Forest method by proposing an online growing of decision trees and combining it with online bagging method. This method is worth investigating for adapting our classifier and facilitating the testing of our methods on 20Mhz IVUS images.

Based on our column-wise classification and the delineation of the vessel walls, quantitative analysis of different plaque components could be accomplished. The plaque is localised between the inner and the outer vessel borders, the column-wise classifier already categorises the

image columns into different plaque types and artifacts. A simple post-processing step will be needed to identify precisely the plaque location. Similarly, the detection of OCT stents could be achieved based on our column-wise classification method. The columns contain the stent strut already detected with a good accuracy, and with knowing that the stent has a bright reflection with strong edge features followed by shadowing. A thresholding method is able to identify the location of the stent in each column.

Although the running time to minimise the energy functions of the proposed spatio-temporal segmentation is within a couple of seconds, it could be improved further by using dynamic graph cut methods [7, 124] that utilise the residual graph from the previous segmentation to find the max-flow/min-cut solution rather than start from scratch, so that our final segmentation after adapting the shape prior and temporal constraints will be achieved in real time.

We plan to make our dataset of images for IVUS and OCT publicly available along with the manual labelling. Currently, there is no dataset for OCT imaging publicly available yet. Our aim is to provide a standardised dataset of images so that the quantitative and qualitative comparisons of OCT lumen and stent detection algorithms will be easily accessible. For IVUS, there was an IVUS challenge [305] organised at MICCAI 2011 CVII workshop that allowed only participants at that time to assess their data. This dataset is not publicly available until 2014. Part of our future work, is to test our methods on these images. However, there are some shortcomings of this dataset that are worth mentioning: they only provide five adjacent frames for 40Mhz ultrasound images with a total of 77 frames, that undermines the ability to examine the temporal information and makes the segmentation far from realistic where every pullback contains a few thousands of frames. Thus, we will also make our IVUS dataset publicly available. It contains a large number of images with an adequate number of connective frames to provide a fair and accurate evaluation of IVUS segmentation methods.

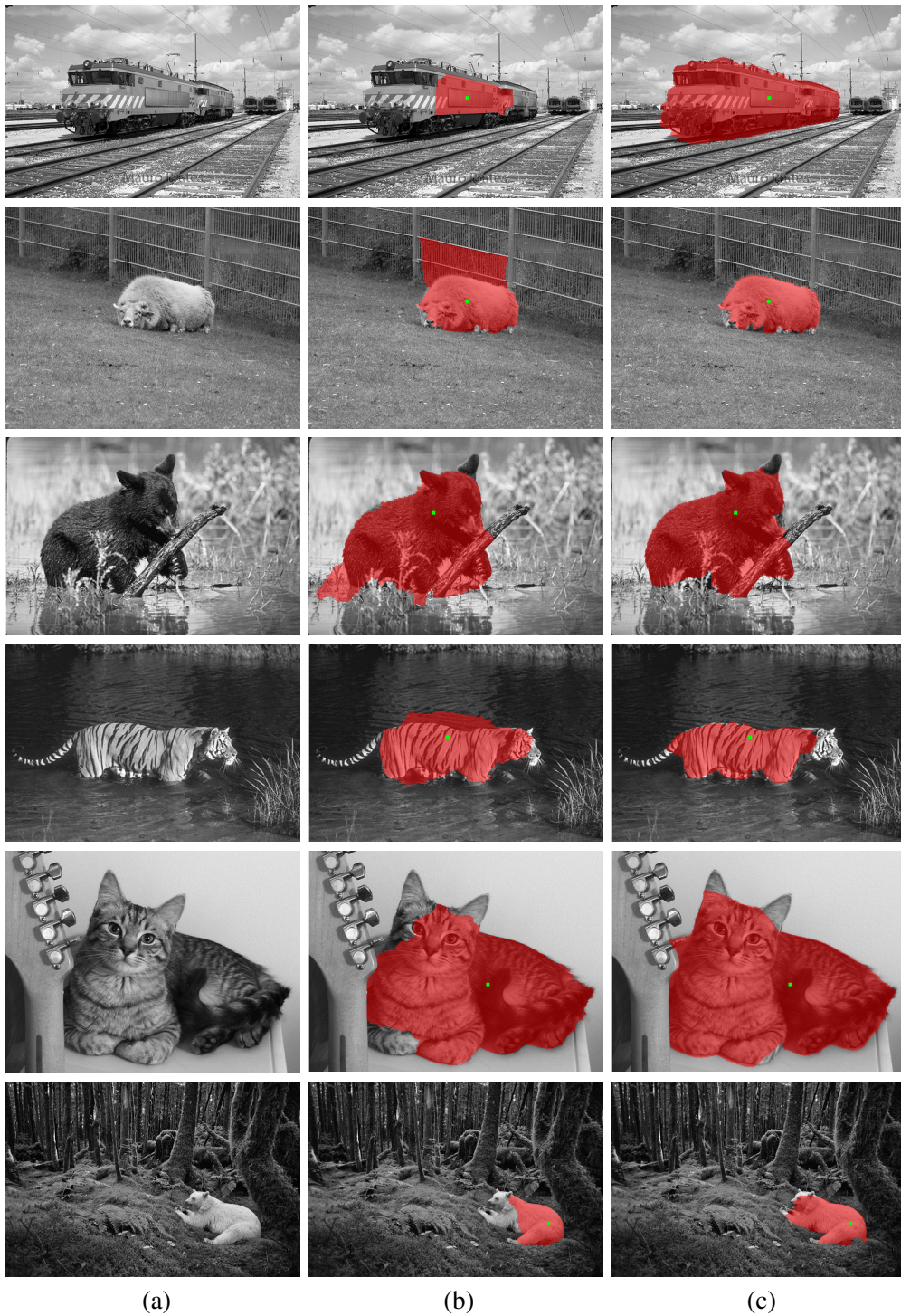


Figure 6.1: Preliminary results using circulation density features. (a) Original image. (b) Star graph cut. (c) Proposed method.



## Appendix A

# List Of Publications

In addition to the publications listed below, a journal paper is under review.

1. J.-L. Jones, E. Essa, X. Xie and J. Cotton, Interactive segmentation of lumen border in OCT, In Proceedings of International Conference on Computational and Mathematical Biomedical Engineering (CMBE), December 2013.
2. H. Zhang, E. Essa, and X. Xie, Graph Based Segmentation with Minimal User Interaction, In Proceedings of the 20th IEEE International Conference on Image Processing (ICIP), pages 4074-4078, September 2013.
3. J.-L. Jones, X. Xie, and E. Essa, Image Segmentation using Combined User Interactions, In Proceedings of the Computational Visual Media Conference, September 2013.
4. J.-L. Jones, E. Essa, X. Xie, and D. Smith, Interactive Segmentation of Media-Adventitia Border in IVUS, In Proceedings of 15th International Conference on Computer Analysis of Images and Patterns (CAIP), pages 466-474, August 2013.
5. E. Essa, X. Xie, I. Sazonov, P. Nithiarasu, D. Smith, Shape Prior Model for Media-Adventitia Border Segmentation in IVUS using Graph Cut, In Proceedings of the Medical Computer Vision MICCAI Workshop, pages 114-123, October 2012.
6. E. Essa, X. Xie, I. Sazonov, P. Nithiarasu, D. Smith, Graph-based Segmentation of Optimal IVUS Media-Adventitia Border using Shape Prior, In Proceedings of the 16th Medical Image Understanding and Analysis (MIUA), pages 143-149, July 2012.

### A. List Of Publications

---

7. E. Essa, X. Xie, I. Sazonov, P. Nithiarasu, Automatic IVUS Media-Adventitia Border Extraction using Double-Interface Graph Cut Segmentation, In Proceedings of the 18th IEEE International Conference on Image Processing (ICIP), pages 69-72, September 2011.
8. E. Essa, X. Xie, I. Sazonov, P. Nithiarasu, D. Smith, Automatic Segmentation of IVUS Media-Adventitia Border with Shape Prior, In Proceedings of the 15th Medical Image Understanding and Analysis (MIUA), pages 1-5, July 2011.
9. E. Essa, X. Xie, I. Sazonov, P. Nithiarasu, Local Phase based Automatic IVUS Media-Adventitia Border Detection, In Proceedings of the 2nd International Conference on Mathematical and Computational Biomedical Engineering (CMBE), pages 233-236, April 2011.

The following abstract has also been published as a result of this work:

- E. Essa, X. Xie, I. Sazonov, P. Nithiarasu, D. Smith , J. Cotton, Graph-based Segmentation For Coronary Artery Imaging, 1st UK National Conference on Patient-Specific Modelling & Translational Research, January 2013.

# Bibliography

- [1] O. Veksler, “Star shape prior for graph-cut image segmentation,” in *Computer Vision ECCV 2008* (D. Forsyth, P. Torr, and A. Zisserman, eds.), vol. 5304 of *Lecture Notes in Computer Science*, pp. 454–467, 2008.
- [2] K. Zhang, L. Zhang, H. Song, and W. Zhou, “Active contours with selective local or global segmentaiton: A new formulation and level set method,” *Image and Vision Computing*, vol. 28, pp. 668–676, 2010.
- [3] B. Li and S. Acton, “Active contour external force using vector field convolution for image segmentation,” *IEEE TIP*, vol. 16, pp. 2096–2106, August 2007.
- [4] C. Li, C. Xu, C. Gui, and M. Fox, “Distance regularized level set evolution and its application to image segmentation,” *IEEE TIP*, vol. 19, pp. 3243–3254, December 2010.
- [5] P. J. Lynch, F. the Oyste, and M. Häggström, “Coronary circulation.” [http://en.wikipedia.org/wiki/File:Coronary\\_arteries.svg#file](http://en.wikipedia.org/wiki/File:Coronary_arteries.svg#file), 2010. Wikimedia Commons [Online; accessed 27-Novmber-2013].
- [6] BruceBlaus, “Coronary artery disease.” [http://commons.wikimedia.org/wiki/File%3ABlausen\\_0259\\_CoronaryArteryDisease\\_02.png](http://commons.wikimedia.org/wiki/File%3ABlausen_0259_CoronaryArteryDisease_02.png), 2013. Wikimedia Commons [Online; accessed 27-Novmber-2013].
- [7] Y. Boykov and G. Funka-Lea, “Graph cuts and efficient N-D image segmentation,” *International Journal of Computer Vision*, vol. 70, no. 1, pp. 109–131, 2006.
- [8] K. Li, X. Wu, D. Z. Chen, and M. Sonka, “Optimal surface segmentation in volumetric images-a graph-theoretic approach,” *IEEE Transations on Pattern Analysis and Machine Intelligence*, vol. 28, no. 1, pp. 119–134, 2006.

- [9] P. Scarborough *et al.*, “Coronary heart disease statistics 2010 edition,” tech. rep., British Heart Foundation: London, 2010.
- [10] N. Townsend, K. Wickramasinghe, P. Bhatnagar, K. Smolina, M. Nichols, J. Leal, R. LungenoFernandez, and M. Rayne, “Coronary heart disease statistics 2012 edition,” tech. rep., British Heart Foundation: London, 2012.
- [11] A. S. Go *et al.*, “Heart disease and stroke statistics 2013 update: A report from the american heart association,” *Circulation*, vol. 127, no. 1, pp. e6–e245, 2013.
- [12] A. Frangi, W. Niessen, K. Vincken, and M. Viergever, “Multiscale vessel enhancement filtering,” in *Medical Image Computing and Computer-Assisted Intervention MICCAI98* (W. Wells, A. Colchester, and S. Delp, eds.), vol. 1496 of *Lecture Notes in Computer Science*, pp. 130–137, Springer Berlin Heidelberg, 1998.
- [13] A. Takagi, K. Hibi, X. Zhang, T. J. Teo, H. N. Bonneau, P. G. Yock, and P. J. Fitzgerald, “Automated contour detection for high frequency intravascular ultrasound imaging: A technique with blood noise reduction for edge enhancement,” *Ultrasound in Medicine and Biology*, vol. 26, no. 6, pp. 1033–1041, 2000.
- [14] M. Sonka, X. Zhang, M. Siebes, M. S. Bissing, S. C. DeJong, S. M. Collins, and C. R. McKay, “Segmentation of intravascular ultrasound images: A knowledge-based approach,” *IEEE Transactions on Medical Imaging*, vol. 14, pp. 719–732, 1995.
- [15] A. Wahle, J. J. Lopez, M. E. Olszewski, S. C. Vigmostad, K. B. Chandran, J. D. Rossen, and M. Sonka, “Plaque development, vessel curvature, and wall shear stress in coronary arteries assessed by x-ray angiography and intravascular ultrasound,” *Medical image analysis*, vol. 10, no. 1, pp. 615–631, 2006.
- [16] C. Gatta, O. Pujol, O. Leor, J. Ferre, and P. Radeva, “Fast rigid registration of vascular structures in ivus sequences,” *IEEE Transactions on Information Technology in Biomedicine*, vol. 13, no. 6, pp. 1006–1011, 2009.
- [17] M. Rosales, P. Radeva, O. Rodriguez-Leor, and D. Gil, “Modelling of image-catheter motion for 3-D IVUS,” *Medical Image Analysis*, vol. 13, no. 1, pp. 91 – 104, 2009.

- [18] C. Blondel, G. Malandain, R. Vaillant, and N. Ayache, "Reconstruction of coronary arteries from a single rotational x-ray projection sequence," *IEEE Transactions on Medical Imaging*, vol. 25, no. 5, pp. 653–663, 2006.
- [19] A. Wahle, G. P. M. Prause, S. DeJong, and M. Sonka, "Geometrically correct 3-d reconstruction of intravascular ultrasound images by fusion with biplane angiography-methods and validation," *Medical Imaging, IEEE Transactions on*, vol. 18, pp. 686–699, Aug 1999.
- [20] R. S. Snell, *Clinical Anatomy by Regions*. Lippincott Williams and Wilkins, 2007.
- [21] A. L. Mescher, *Junqueira's Basic Histology: Text and Atlas*. McGraw-Hill Medical, 2009.
- [22] M.-H. R. Cardinal, J. Meunier, G. Soulez, R. L. Maurice, É. Therasse, and G. Cloutier, "Intravascular ultrasound image segmentation: a three-dimensional fast-marching method based on gray level distributions," *IEEE Transactions on Medical Imaging*, vol. 25, no. 1, pp. 590–601, 2006.
- [23] E. U. G. H. T. H. M. M. Ryosuke Kubota, Noriaki Suetake, "Polynomial-based boundary extraction of plaque in intravascular ultrasound image by using its local statistical information," in *Information and Control Express Letters (ICIC-EL)*, vol. 2, pp. 387–393, 2008.
- [24] J.-L. Jones, E. Essa, X. Xie, and D. Smith, "Interactive segmentation of media-adventitia border in ivus," in *Computer Analysis of Images and Patterns* (R. Wilson, E. Hancock, A. Bors, and W. Smith, eds.), vol. 8048 of *Lecture Notes in Computer Science*, pp. 466–474, Springer Berlin Heidelberg, 2013.
- [25] S. Sun, M. Sonka, and R. Beichel, "Graph-based IVUS segmentation with efficient computer-aided refinement," *IEEE Transactions on Medical Imaging*, vol. 32, no. 8, pp. 1536–1549, 2013.
- [26] E. d. S. Filho, M. Yoshizawa, A. Tanaka, Y. Saijo, and T. Iwamoto, "Moment-based texture segmentation of luminal contour in intravascular ultrasound images," *Journal of Medical Ultrasonics*, vol. 32, no. 3, pp. 91–99, 2005.

- [27] M. Papadogiorgaki, V. Mezaris, Y. S. Chatzizisis, G. D. Giannoglou, and I. Kompatsiaris, "Image analysis techniques for automated ivus contour detection," *Ultrasound in Medicine and Biology*, vol. 9, no. 34, pp. 1482–1498, 2008.
- [28] E. Brusseau, C. De Korte, F. Mastik, J. Schaar, and A. F. W. Van der Steen, "Fully automatic luminal contour segmentation in intracoronary ultrasound imaging—a statistical approach," *IEEE Transactions on Medical Imaging*, vol. 23, no. 5, pp. 554–566, 2004.
- [29] Y. Boykov and M.-P. Jolly, "Interactive graph cuts for optimal boundary and region segmentation of objects in n-d images," in *IEEE International Conference on Computer Vision*, pp. 105–112, 2001.
- [30] S. Tsantis, G. C. Kagadis, K. Katsanos, D. Karnabatidis, G. Bourantas, and G. C. Niki-foridis, "Automatic vessel lumen segmentation and stent strut detection in intravascular optical coherence tomography," *Med. Phys.*, vol. 39, no. 1, pp. 503–513, 2012.
- [31] M. Zheng, W. Yubin, W. Yousheng, S. Xiaodi, and W. Yali, "Detection of the lumen and media-adventitia borders in ivus imaging," in *9th International Conference on Signal Processing, ICSP*, pp. 1059–1062, 2008.
- [32] D. Gil, P. Radeva, and J. Saludes, "Segmentation of artery wall in coronary ivus images: a probabilistic approach," in *15th International Conference on Pattern Recognition*, vol. 4, pp. 352–355 vol.4, 2000.
- [33] G. Unal, S. Bucher, S. Carlier, G. Slabaugh, T. Fang, and K. Tanak, "Shape-driven segmentation of the arterial wall in intravascular ultrasound images," *IEEE Transactions on Information Technology in Biomedicine*, vol. 12, no. 3, pp. 335–347, 2008.
- [34] G. Slabaugh and G. Unal, "Graph cuts segmentation using an elliptical shape prior," in *IEEE International Conference on Image Processing (ICIP)*, vol. 2, pp. II–1222–5, 2005.
- [35] D. Freedman and T. Zhang, "Interactive graph cut based segmentation with shape priors," in *IEEE Computer Society Conference on Computer Vision and Pattern Recognition (CVPR)*, vol. 1, pp. 755–762 vol. 1, 2005.

- 
- [36] J. Malcolm, Y. Rathi, and A. Tannenbaum, "Graph cut segmentation with nonlinear shape priors," in *IEEE International Conference on Image Processing (ICIP)*, vol. 4, pp. IV – 365–IV – 368, 2007.
- [37] N. Vu and B. Manjunath, "Shape prior segmentation of multiple objects with graph cuts," in *IEEE Conference on Computer Vision and Pattern Recognition (CVPR)*, pp. 1–8, 2008.
- [38] S. V. Raman, R. Morford, M. Neff, T. T. Attar, G. Kukielka, R. D. Magorien, and C. A. Bush, "Rotational x-ray coronary angiography," *Catheterization and Cardiovascular Interventions*, vol. 63, no. 2, pp. 201–207, 2004.
- [39] K. Empen, E. Kuon, A. Hummel, C. Gebauer, M. Drr, R. Knemann, W. Hoffmann, A. Staudt, K. Weitmann, T. Reffelmann, and S. B. Felix, "Comparison of rotational with conventional coronary angiography," *American Heart Journal*, vol. 160, no. 3, pp. 552 – 563, 2010.
- [40] A. Katouzian, E. Angelini, S. Carlier, J. Suri, N. Navab, and A. Laine, "A state-of-the-art review on segmentation algorithms in intravascular ultrasound (ivus) images," *Information Technology in Biomedicine, IEEE Transactions on*, vol. 16, pp. 823–834, Sept 2012.
- [41] D. Huang, E. Swanson, C. Lin, J. Schuman, W. Stinson, W. Chang, M. Hee, T. Flotte, K. Gregory, C. Puliafito, and a. et, "Optical coherence tomography," *Science*, vol. 254, no. 5035, pp. 1178–1181, 1991.
- [42] F. Prati *et al.*, "Expert review document on methodology, terminology, and clinical applications of optical coherence tomography: physical principles, methodology of image acquisition, and clinical application for assessment of coronary arteries and atherosclerosis," *European Heart Journal*, vol. 31, pp. 401–415, 2010.
- [43] S. Takarada, T. Imanishi, Y. Liu, H. Ikejima, H. Tsujioka, A. Kuroi, K. Ishibashi, K. Komukai, T. Tanimoto, Y. Ino, H. Kitabata, T. Kubo, N. Nakamura, K. Hirata, A. Tanaka, M. Mizukoshi, and T. Akasaka, "Advantage of next-generation frequency-domain optical coherence tomography compared with conventional time-domain system in the assessment of coronary lesion," *Catheterization and Cardiovascular Interventions*, vol. 75, no. 2, pp. 202–206, 2010.

- [44] S. Yun, G. Tearney, J. de Boer, N. Iftimia, and B. Bouma, “High-speed optical frequency-domain imaging,” *Opt. Express*, vol. 11, no. 22, pp. 2953–2963, 2003.
- [45] M. A. Choma, K. Hsu, and J. A. Izatt, “Swept source optical coherence tomography using an all-fiber 1300-nm ring laser source,” *Journal of Biomedical Optics*, vol. 10, no. 4, pp. 044009–044009–6, 2005.
- [46] N. Gonzalo, G. J. Tearney, P. W. Serruys, G. van Soest, T. Okamura, H. M. Garca-Garca, R. Jan van Geuns, M. van der Ent, J. Ligthart, B. E. Bouma, and E. Regar, “Second-generation optical coherence tomography in clinical practice. high-speed data acquisition is highly reproducible in patients undergoing percutaneous coronary intervention,” *Revista Española de Cardiología (English Version)*, vol. 63, no. 8, pp. 893–903, 2010.
- [47] Z. Sun, G. H. Choo, and K. H. Ng, “Coronary ct angiography: current status and continuing challenges,” *British Journal of Radiology*, vol. 85, no. 1013, pp. 495–510, 2012.
- [48] K. Nieman, M. Oudkerk, B. J. Rensing, P. van Ooijen, A. Munne, R.-J. van Geuns, and P. J. de Feyter, “Coronary angiography with multi-slice computed tomography,” *The Lancet*, vol. 357, no. 9256, pp. 599 – 603, 2001.
- [49] S. Ulzheimer and T. Flohr, “Multislice ct: Current technology and future developments,” in *Multislice CT* (M. F. Reiser, C. Becker, K. Nikolaou, and G. Glazer, eds.), Medical Radiology, pp. 3–23, Springer Berlin Heidelberg, 2009.
- [50] F. de Graaf, J. Schuijf, V. Delgado, J. van Velzen, L. Kroft, A. de Roos, J. Jukema, E. van der Wall, and J. Bax, “Clinical application of {CT} coronary angiography: State of the art,” *Heart, Lung and Circulation*, vol. 19, no. 3, pp. 107 – 116, 2010.
- [51] A. W. Leber, T. Johnson, A. Becker, F. von Ziegler, J. Tittus, K. Nikolaou, M. Reiser, G. Steinbeck, C. R. Becker, and A. Knez, “Diagnostic accuracy of dual-source multi-slice ct-coronary angiography in patients with an intermediate pretest likelihood for coronary artery disease,” *European Heart Journal*, vol. 28, no. 19, pp. 2354–2360, 2007.
- [52] J. Sun, Z. Zhang, B. Lu, W. Yu, Y. Yang, Y. Zhou, Y. Wang, and Z. Fan, “Identification and quantification of coronary atherosclerotic plaques: A comparison of 64-mdct and intravascular ultrasound,” *American Journal of Roentgenology*, vol. 190, no. 3, pp. 748–754, 2008.

- 
- [53] S. Achenbach and P. Raggi, "Imaging of coronary atherosclerosis by computed tomography," *European Heart Journal*, vol. 31, no. 12, pp. 1442–1448, 2010.
- [54] C. Yuan *et al.*, "In vivo accuracy of multispectral magnetic resonance imaging for identifying lipid-rich necrotic cores and intraplaque hemorrhage in advanced human carotid plaques," *Circulation*, vol. 104, no. 17, pp. 2051–2056, 2001.
- [55] T. Saam, M. Ferguson, V. Yarnykh, N. Takaya, D. Xu, N. Polissar, T. Hatsukami, and C. Yuan, "Quantitative evaluation of carotid plaque composition by in vivo mri," *Atherosclerosis, Thrombosis, and Vascular Biology*, vol. 25, no. 1, pp. 234–239, 2005.
- [56] Z. A. Fayad *et al.*, "In vivo magnetic resonance evaluation of atherosclerotic plaques in the human thoracic aorta: A comparison with transesophageal echocardiography," *Circulation*, vol. 101, no. 21, pp. 2503–2509, 2000.
- [57] Z. A. Fayad and V. Fuster, "The human high-risk plaque and its detection by magnetic resonance imaging," *The American Journal of Cardiology*, vol. 88, no. 2, Supplement 1, pp. 42–45, 2001.
- [58] Z. A. Fayad *et al.*, "Noninvasive in vivo human coronary artery lumen and wall imaging using black-blood magnetic resonance imaging," *Circulation*, vol. 102, no. 5, pp. 506–510, 2000.
- [59] R. M. Botnar, M. Stuber, K. V. Kissinger, W. Y. Kim, E. Spuentrup, and W. J. Manning, "Noninvasive coronary vessel wall and plaque imaging with magnetic resonance imaging," *Circulation*, vol. 102, no. 21, pp. 2582–2587, 2000.
- [60] K. Nikolaou *et al.*, "Multidetector-row computed tomography and magnetic resonance imaging of atherosclerotic lesions in human ex vivo coronary arteries," *Atherosclerosis*, vol. 174, no. 2, pp. 243 – 252, 2004.
- [61] T. Li *et al.*, "Classification of human coronary atherosclerotic plaques using ex vivo high-resolution multicontrast-weighted mri compared with histopathology," *American Journal of Roentgenology*, vol. 198, no. 5, pp. 1069–1075, 2012.
- [62] M. Hartung, T. Grist, and C. Francois, "Magnetic resonance angiography: current status and future directions," *Journal of Cardiovascular Magnetic Resonance*, vol. 13, no. 1, p. 19, 2011.

- [63] W. Y. Kim *et al.*, “Coronary magnetic resonance angiography for the detection of coronary stenoses,” *New England Journal of Medicine*, vol. 345, no. 26, pp. 1863–1869, 2001.
- [64] G. F. Greil *et al.*, “Coronary magnetic resonance angiography in adolescents and young adults with kawasaki disease,” *Circulation*, vol. 105, no. 8, pp. 908–911, 2002.
- [65] O. M. Weber, A. J. Martin, and C. B. Higgins, “Whole-heart steady-state free precession coronary artery magnetic resonance angiography,” *Magnetic Resonance in Medicine*, vol. 50, no. 6, pp. 1223–1228, 2003.
- [66] C. Jahnke, I. Paetsch, K. Nehrke, B. Schnackenburg, R. Gebker, E. Fleck, and E. Nagel, “Rapid and complete coronary arterial tree visualization with magnetic resonance imaging: feasibility and diagnostic performance,” *European Heart Journal*, vol. 26, no. 21, pp. 2313–2319, 2005.
- [67] X. Liu, X. Bi, J. Huang, R. Jerecic, J. Carr, and D. Li, “Contrast-enhanced whole-heart coronary magnetic resonance angiography at 3.0 t: Comparison with steady-state free precession technique at 1.5 t,” *Source Investigative Radiology*, vol. 43, no. 9, pp. 663–668, 2008.
- [68] Q. Yang, K. Li, X. Liu, X. Bi, Z. Liu, J. An, A. Zhang, R. Jerecic, and D. Li, “Contrast-enhanced whole-heart coronary magnetic resonance angiography at 3.0-ta comparative study with x-ray angiography in a single center,” *Journal of the American College of Cardiology*, vol. 54, no. 1, pp. 69–76, 2009.
- [69] M. Lettau, A. Sauer, S. Heiland, S. Rohde, M. Bendszus, and S. Hhnel, “Carotid artery stents: In vitro comparison of different stent designs and sizes using ct angiography and contrast-enhanced mr angiography at 1.5t and 3t,” *American Journal of Neuroradiology*, vol. 30, no. 10, pp. 1993–1997, 2009.
- [70] D. Lesage, E. D. Angelini, I. Bloch, and G. Funka-Lea, “A review of 3d vessel lumen segmentation techniques: Models, features and extraction schemes,” *Medical Image Analysis*, vol. 13, no. 6, pp. 819 – 845, 2009. Includes Special Section on Computational Biomechanics for Medicine.
- [71] C. Kirbas and F. Quek, “A review of vessel extraction techniques and algorithms,” *ACM Comput. Surv.*, vol. 36, no. 2, pp. 81–121, 2004.

- 
- [72] W. T. Freeman and E. H. Adelson, "The design and use of steerable filters," *IEEE Transactions on Pattern Analysis and Machine Intelligence*, vol. 13, no. 9, pp. 891–906, 1991.
- [73] M. Moraes and S. Furuie, "An automatic media-adventitia border segmentation approach for ivus images," in *Computing in Cardiology*, pp. 389–392, 2010.
- [74] N. Otsu, "A threshold selection method from gray-level histograms," *Automatica*, vol. 11, no. 285-296, pp. 23–27, 1975.
- [75] S. W. Zucker, "Region growing: Childhood and adolescence," *Computer Graphics and Image Processing*, vol. 5, no. 3, pp. 382 – 399, 1976.
- [76] R. Adams and L. Bischof, "Seeded region growing," *IEEE Transactions on Pattern Analysis and Machine Intelligence*, vol. 16, no. 6, pp. 641–647, 1994.
- [77] S. Bock, C. Khnel, T. Boskamp, and H.-O. Peitgen, "Robust vessel segmentation," vol. 6915, pp. 691539–691539–9, 2008.
- [78] J. Serra, *Image Analysis and Mathematical Morphology*. Orlando, FL, USA: Academic Press, Inc., 1983.
- [79] Y. Masutani, T. Schiemann, and K.-H. Hhne, "Vascular shape segmentation and structure extraction using a shape-based region-growing model," in *Medical Image Computing and Computer-Assisted Intervention MICCAI98* (W. Wells, A. Colchester, and S. Delp, eds.), vol. 1496 of *Lecture Notes in Computer Science*, pp. 1242–1249, 1998.
- [80] M. Donizelli, "Region-oriented segmentation of vascular structures from dsa images using mathematical morphology and binary region growing," in *Bildverarbeitung fr die Medizin 1998* (T. Lehmann, V. Metzler, K. Spitzer, and T. Tolxdorff, eds.), Informatik aktuell, pp. 303–307, Springer Berlin Heidelberg, 1998.
- [81] P. Brathwaite, K. Chandran, D. McPherson, and E. Dove, "Lumen detection in human ivus images using region-growing," in *Computers in Cardiology, 1996*, pp. 37–40, 1996.
- [82] S. Wesarg and E. A. Firl, "Segmentation of vessels: the corkscrew algorithm," vol. 5370, pp. 1609–1620, 2004.
- [83] B. Bouraoui, C. Ronse, J. Baruthio, N. Passat, and P. Germain, "Fully automatic 3d segmentation of coronary arteries based on mathematical morphology," in *5th IEEE*

- International Symposium on Biomedical Imaging: From Nano to Macro*, pp. 1059–1062, 2008.
- [84] E. Dijkstra, “A note on two problems in connexion with graphs,” *Numerische Mathematik*, vol. 1, no. 1, pp. 269–271, 1959.
- [85] P. E. Hart, N. J. Nilsson, and B. Raphael, “Correction to ”a formal basis for the heuristic determination of minimum cost paths”,” *SIGART Bull.*, no. 37, pp. 28–29, 1972.
- [86] M. Sonka, V. Hlavac, and R. Boyle, *Image Processing, Analysis, and Machine Vision*. Thomson-Engineering, 2007.
- [87] E. N. Mortensen and W. A. Barrett, “Interactive segmentation with intelligent scissors,” *Graphical Models and Image Processing*, vol. 60, no. 5, pp. 349 – 384, 1998.
- [88] A. X. Falcao, J. K. Udupa, S. Samarasekera, and B. E. Hirsch, “User-steered image boundary segmentation,” vol. 2710, pp. 278–288, 1996.
- [89] A. X. Falcão, J. K. Udupa, S. Samarasekera, S. Sharma, B. E. Hirsch, and R. d. A. Lotufo, “User-steered image segmentation paradigms: Live wire and live lane,” *Graph. Models Image Process.*, vol. 60, no. 4, pp. 233–260, 1998.
- [90] A. Falcao, J. Udupa, and F. Miyazawa, “An ultra-fast user-steered image segmentation paradigm: live wire on the fly,” *IEEE Transactions on Medical Imaging*, vol. 19, no. 1, pp. 55–62, 2000.
- [91] A. X. Falcao and J. K. Udupa, “Segmentation of 3d objects using live wire,” vol. 3034, pp. 228–235, 1997.
- [92] G. Hamarneh, J. Yang, C. McIntosh, and M. Langille, “3d live-wire-based semi-automatic segmentation of medical images,” in *Proc. SPIE*, pp. 1597–1603, 2005.
- [93] L. Grady, “Minimal surfaces extend shortest path segmentation methods to 3d,” *IEEE Transactions on Pattern Analysis and Machine Intelligence*, vol. 32, pp. 321–334, Feb 2010.
- [94] O. Wink, A. F. Frangi, B. Verdonck, M. A. Viergever, and W. J. Niessen, “3d mra coronary axis determination using a minimum cost path approach,” *Magnetic Resonance in Medicine*, vol. 47, no. 6, pp. 1169–1175, 2002.

- 
- [95] S. Olabbarriaga, M. Breeuwer, and W. Niessen, "Minimum cost path algorithm for coronary artery central axis tracking in ct images," in *Medical Image Computing and Computer-Assisted Intervention - MICCAI 2003* (R. Ellis and T. Peters, eds.), vol. 2879 of *Lecture Notes in Computer Science*, pp. 687–694, Springer Berlin Heidelberg, 2003.
- [96] O. Wink, W. Niessen, and M. Viergever, "Multiscale vessel tracking," *Medical Imaging, IEEE Transactions on*, vol. 23, no. 1, pp. 130–133, 2004.
- [97] C. T. Metz, M. Schaap, A. C. Weustink, N. R. Mollet, T. van Walsum, and W. J. Niessen, "Coronary centerline extraction from ct coronary angiography images using a minimum cost path approach," *Medical Physics*, vol. 36, no. 12, pp. 5568–5579, 2009.
- [98] W. Li *et al.*, "Semi-automatic contour detection for volumetric quantification of intracoronary ultrasound," in *Computers in Cardiology*, pp. 277–280, 1994.
- [99] C. von Birgelen *et al.*, "Morphometric analysis in three-dimensional intracoronary ultrasound: An in vitro and in vivo study performed with a novel system for the contour detection of lumen and plaque," *American Heart Journal*, vol. 132, no. 3, pp. 516 – 527, 1996.
- [100] D. M. Greig, B. T. Porteous, and A. H. Seheult, "Exact maximum a posteriori estimation for binary images," *Journal of the Royal Statistical Society. Series B (Methodological)*, pp. 271–279, 1989.
- [101] Y. Boykov, O. Veksler, and R. Zabih, "Fast approximate energy minimization via graph cuts," in *IEEE International Conference on Computer Vision*, vol. 1, pp. 377–384 vol.1, 1999.
- [102] Y. Boykov, O. Veksler, and R. Zabih, "Fast approximate energy minimization via graph cuts," *Pattern Analysis and Machine Intelligence, IEEE Transactions on*, vol. 23, no. 11, pp. 1222–1239, 2001.
- [103] H. Ishikawa, "Exact optimization for markov random fields with convex priors," *IEEE Transactions on Pattern Analysis and Machine Intelligence*, vol. 25, no. 10, pp. 1333–1336, 2003.

- [104] P. Kohli, L. Ladický, and P. H. S. Torr, “Robust higher order potentials for enforcing label consistency,” in *IEEE Conference on Computer Vision Pattern Recognition*, pp. 1–8, 2008.
- [105] H. Ishikawa, “Higher-order clique reduction in binary graph cut,” *IEEE Conference on Computer Vision Pattern Recognition*, vol. 0, pp. 2993–3000, 2009.
- [106] A. Fix, A. Gruber, E. Boros, and R. Zabih, “A graph cut algorithm for higher-order markov random fields,” in *IEEE International Conference on Computer Vision*, pp. 1020–1027, 2011.
- [107] M. F. Tappen and W. T. Freeman, “Comparison of graph cuts with belief propagation for stereo, using identical mrf parameters,” in *Proceedings of the Ninth IEEE International Conference on Computer Vision - Volume 2, ICCV '03*, pp. 900–, 2003.
- [108] R. Szeliski *et al.*, “A comparative study of energy minimization methods for markov random fields with smoothness-based priors,” *Pattern Analysis and Machine Intelligence, IEEE Transactions on*, vol. 30, no. 6, pp. 1068–1080, 2008.
- [109] M. Wainwright, T. Jaakkola, and A. Willsky, “Map estimation via agreement on trees: message-passing and linear programming,” *IEEE Transactions on Information Theory*, vol. 51, pp. 3697–3717, Nov 2005.
- [110] J. Besag, “On the Statistical Analysis of Dirty Pictures,” *Journal of the Royal Statistical Society. Series B (Methodological)*, vol. 48, no. 3, pp. 259–302, 1986.
- [111] Y. Boykov and O. Veksler, “Graph cuts in vision and graphics: Theories and applications,” in *Handbook of Mathematical Models in Computer Vision* (N. Paragios, Y. Chen, and O. Faugeras, eds.), pp. 79–96, Springer US, 2006.
- [112] E. A. Dinic, “Algorithm for Solution of a Problem of Maximum Flow in a Network with Power Estimation,” *Soviet Math Doklady*, vol. 11, pp. 1277–1280, 1970.
- [113] A. V. Goldberg and R. E. Tarjan, “A new approach to the maximum-flow problem,” *J. ACM*, vol. 35, no. 4, pp. 921–940, 1988.
- [114] Y. Boykov and V. Kolmogorov, “An experimental comparison of min-cut/max-flow algorithms for energy minimization in vision,” *IEEE Transactions on Pattern Analysis and Machine Intelligence*, vol. 26, no. 9, pp. 1124–1137, 2004.

- 
- [115] C. Rother, V. Kolmogorov, and A. Blake, “‘grabcut’: Interactive foreground extraction using iterated graph cuts,” *ACM Trans. Graph.*, vol. 23, no. 3, pp. 309–314, 2004.
- [116] Y. Li, J. Sun, C.-K. Tang, and H.-Y. Shum, “Lazy snapping,” *ACM Trans. Graph.*, vol. 23, no. 3, pp. 303–308, 2004.
- [117] S. Vicente, V. Kolmogorov, and C. Rother, “Graph cut based image segmentation with connectivity priors,” in *IEEE Conference on Computer Vision Pattern Recognition*, pp. 1–8, 2008.
- [118] Y. Boykov and V. Kolmogorov, “Computing geodesics and minimal surfaces via graph cuts,” in *IEEE International Conference on Computer Vision*, pp. 26–33 vol.1, 2003.
- [119] V. Kolmogorov and Y. Boykov, “What metrics can be approximated by geo-cuts, or global optimization of length/area and flux,” in *Proceedings of the Tenth IEEE International Conference on Computer Vision (ICCV’05) Volume 1 - Volume 01*, ICCV ’05, pp. 564–571, 2005.
- [120] J. Shi and J. Malik, “Normalized cuts and image segmentation,” vol. 22, no. 8, pp. 888–905, 2000.
- [121] A. Moore, S. Prince, and J. Warrell, “‘lattice cut’ - constructing superpixels using layer constraints,” in *IEEE Conference on Computer Vision Pattern Recognition*, pp. 2117–2124, 2010.
- [122] O. Veksler, Y. Boykov, and P. Mehrani, “Superpixels and supervoxels in an energy optimization framework,” in *Proceedings of the 11th European Conference on Computer Vision: Part V*, ECCV’10, pp. 211–224, 2010.
- [123] P. Kohli and P. H. S. Torr, “Efficiently solving dynamic markov random fields using graph cuts,” in *IEEE International Conference on Computer Vision*, vol. 2, pp. 922–929 Vol. 2, 2005.
- [124] P. Kohli and P. H. S. Torr, “Dynamic graph cuts for efficient inference in markov random fields,” vol. 29, no. 12, pp. 2079–2088, 2007.
- [125] M. Schaap, L. Neefjes, C. Metz, A. Giessen, A. Weustink, N. Mollet, J. Wentzel, T. Walsum, and W. Niessen, “Coronary lumen segmentation using graph cuts and robust ker-

- nel regression,” in *Information Processing in Medical Imaging* (J. Prince, D. Pham, and K. Myers, eds.), vol. 5636 of *Lecture Notes in Computer Science*, pp. 528–539, 2009.
- [126] F. Zhao, H. Zhang, A. Wahle, M. T. Thomas, A. H. Stolpen, T. D. Scholz, and M. Sonka, “Congenital aortic disease: 4d magnetic resonance segmentation and quantitative analysis,” *Medical Image Analysis*, vol. 13, no. 3, pp. 483 – 493, 2009.
- [127] C. Bauer, T. Pock, E. Sorantin, H. Bischof, and R. Beichel, “Segmentation of interwoven 3d tubular tree structures utilizing shape priors and graph cuts,” *Medical Image Analysis*, vol. 14, no. 2, pp. 172 – 184, 2010.
- [128] K.-P. Tung, W.-Z. Shi, R. D. Silva, E. Edwards, and D. Rueckert, “Automatic vessel wall detection in intravascular coronary oct,” in *Proc. IEEE International Symposium on Biomedical Imaging: From Nano to Macro*, pp. 610–613, 2011.
- [129] N. Zhu and A. Chung, “Graph-based optimization with tubularity markov tree for 3d vessel segmentation,” in *IEEE Conference on Computer Vision Pattern Recognition*, pp. 2219–2226, 2013.
- [130] C. Xu, D. L. Pham, and J. L. Prince, “Medical image segmentation using deformable models,” in *Handbook of Medical Imaging – Volume 2: Medical Image Processing and Analysis* (J. Fitzpatrick and M. Sonka, eds.), pp. 129–174, SPIE Press, 2000.
- [131] G. Tsechpenakis, “Deformable model-based medical image segmentation,” in *Multi Modality State-of-the-Art Medical Image Segmentation and Registration Methodologies* (A. S. El-Baz, R. Acharya U, M. Mirmehdi, and J. S. Suri, eds.), pp. 33–67, Springer US, 2011.
- [132] A. Sotiras, C. Davatzikos, and N. Paragios, “Deformable medical image registration: A survey,” *Medical Imaging, IEEE Transactions on*, vol. 32, no. 7, pp. 1153–1190, 2013.
- [133] S. Osher and J. A. Sethian, “Fronts propagating with curvature-dependent speed: Algorithms based on hamilton-jacobi formulations,” *Journal of Computational Physics*, vol. 79, no. 1, pp. 12 – 49, 1988.
- [134] J. A. Sethian, *Level Set Methods and Fast Marching Methods: Evolving Interfaces in Computational Geometry, Fluid Mechanics, Computer Vision, and Material Science*. Cambridge, UK: Cambridge University Press, 2 ed., 1999.

- 
- [135] M. Kass, A. Witkin, and D. Terzopoulos, "Snakes: Active contour models," *International Journal of Computer Vision*, vol. 1, no. 4, pp. 321–331, 1988.
- [136] A. Amini, T. Weymouth, and R. Jain, "Using dynamic programming for solving variational problems in vision," *IEEE Transactions on Pattern Analysis and Machine Intelligence*, vol. 12, no. 9, pp. 855–867, 1990.
- [137] D. Terzopoulos, A. Witkin, and M. Kass, "Constraints on deformable models: Recovering 3d shape and nongrid motion," *Artif. Intell.*, vol. 36, no. 1, pp. 91–123, 1988.
- [138] L. D. Cohen, "On active contour models and balloons," *CVGIP: Image Understanding*, vol. 53, no. 2, pp. 211 – 218, 1991.
- [139] L. Cohen and I. Cohen, "Finite-element methods for active contour models and balloons for 2-D and 3-D images," *IEEE Transactions on Pattern Analysis and Machine Intelligence*, vol. 15, no. 11, pp. 1131–1147, 1993.
- [140] C. Xu and J. Prince, "Snakes, shapes, and gradient vector flow," *IEEE Transactions on Image Processing*, vol. 7, no. 3, pp. 359–369, 1998.
- [141] R. Ronfard, "Region-based strategies for active contour models," *International Journal of Computer Vision*, vol. 13, no. 2, pp. 229–251, 1994.
- [142] S. Zhu, T. S. Lee, and A. Yuille, "Region competition: unifying snakes, region growing, energy/bayes/mdl for multi-band image segmentation," in *IEEE International Conference on Computer Vision*, pp. 416–423, 1995.
- [143] C. S. Poon and M. Braun, "Image segmentation by a deformable contour model incorporating region analysis," *Physics in Medicine and Biology*, vol. 42, no. 9, pp. 1833–1841, 1997.
- [144] A. Hernandez, D. Gil, P. Radeva, and E. N. Nofrerias, "Anisotropic processing of image structures for adventitia detection in intravascular ultrasound images," in *Computers in Cardiology, 2004*, pp. 229–232, Sept 2004.
- [145] D. Gil, A. Hernandez, O. Rodriguez, J. Mauri, and P. Radeva, "Statistical strategy for anisotropic adventitia modelling in ivus," *IEEE Transactions on Medical Imaging*, vol. 25, no. 6, pp. 768–778, 2006.

- [146] M. Zheng, W. Yubin, W. Yousheng, S. Xiaodi, and W. Yali, "Detection of the lumen and media-adventitia borders in ivus imaging," in *9th International Conference on Signal Processing, ICSP*, pp. 1059–1062, Oct 2008.
- [147] G. D. Giannoglou *et al.*, "A novel active contour model for fully automated segmentation of intravascular ultrasound images: In vivo validation in human coronary arteries," *Computers in Biology and Medicine*, vol. 37, no. 9, pp. 1292 – 1302, 2007.
- [148] M. Plissiti, D. Fotiadis, L. Michalis, and G. Bozios, "An automated method for lumen and media-adventitia border detection in a sequence of ivus frames," *IEEE Transactions on Information Technology in Biomedicine*, vol. 8, pp. 131–141, June 2004.
- [149] J. Klingensmith, R. Shekhar, and D. Vince, "Evaluation of three-dimensional segmentation algorithms for the identification of luminal and medial-adventitial borders in intravascular ultrasound images," *IEEE Transactions on Medical Imaging*, vol. 19, pp. 996–1011, Oct 2000.
- [150] C. Kauffmann, P. Motreff, and L. Sarry, "in vivo supervised analysis of stent reendothelialization from optical coherence tomography," *IEEE Transactions on Medical Imaging*, vol. 29, no. 3, pp. 807–818, 2010.
- [151] V. Caselles, F. Catté, T. Coll, and F. Dibos, "A geometric model for active contours in image processing," *Numerische Mathematik*, vol. 66, no. 1, pp. 1–31, 1993.
- [152] R. Malladi, J. Sethian, and B. Vemuri, "Shape modeling with front propagation: a level set approach," *IEEE Transactions on Pattern Analysis and Machine Intelligence*, vol. 17, no. 2, pp. 158–175, 1995.
- [153] V. Caselles, R. Kimmel, and G. Sapiro, "Geodesic active contours," *Int. J. Comput. Vision*, vol. 22, no. 1, pp. 61–79, 1997.
- [154] J. Yezzi, A., S. Kichenassamy, A. Kumar, P. Olver, and A. Tannenbaum, "A geometric snake model for segmentation of medical imagery," *IEEE Transactions on Medical Imaging*, vol. 16, no. 2, pp. 199–209, 1997.
- [155] K. Siddiqi, Y. Lauziere, A. Tannenbaum, and S. Zucker, "Area and length minimizing flows for shape segmentation," *IEEE Transactions on Image Processing*, vol. 7, no. 3, pp. 433–443, 1998.

- 
- [156] T. Chan and L. Vese, "Active contours without edges," *IEEE Transactions on Image Processing*, vol. 10, no. 2, pp. 266–277, 2001.
- [157] L. Vese and T. Chan, "A multiphase level set framework for image segmentation using the mumford and shah model," *International Journal of Computer Vision*, vol. 50, no. 3, pp. 271–293, 2002.
- [158] N. Paragios and R. Deriche, "Geodesic active regions and level set methods for supervised texture segmentation," *International Journal of Computer Vision*, vol. 46, no. 3, pp. 223–247, 2002.
- [159] X. Xie and M. Mirmehdi, "Rags: Region-aided geometric snake," *IEEE Transactions on Image Processing*, vol. 13, no. 5, pp. 640–652, 2004.
- [160] M. Leventon, W. E. L. Grimson, and O. Faugeras, "Statistical shape influence in geodesic active contours," in *IEEE Conference on Computer Vision and Pattern Recognition*, vol. 1, pp. 316–323 vol.1, 2000.
- [161] A. Tsai *et al.*, "A shape-based approach to the segmentation of medical imagery using level sets," *IEEE Transactions on Medical Imaging*, vol. 22, no. 2, pp. 137–154, 2003.
- [162] S. Dambreville, Y. Rathi, and A. Tannenbaum, "A framework for image segmentation using shape models and kernel space shape priors," *IEEE Transactions on Pattern Analysis and Machine Intelligence*, vol. 30, no. 8, pp. 1385–1399, 2008.
- [163] M. Rousson and N. Paragios, "Shape priors for level set representations," in *Computer Vision ECCV 2002* (A. Heyden, G. Sparr, M. Nielsen, and P. Johansen, eds.), vol. 2351 of *Lecture Notes in Computer Science*, pp. 78–92, Springer Berlin Heidelberg, 2002.
- [164] D. Cremers, S. Osher, and S. Soatto, "Kernel density estimation and intrinsic alignment for shape priors in level set segmentation," *International Journal of Computer Vision*, vol. 69, no. 3, pp. 335–351, 2006.
- [165] D. Cremers and M. Rousson, "Efficient kernel density estimation of shape and intensity priors for level set segmentation," in *Deformable Models*, Topics in Biomedical Engineering. International Book Series, pp. 447–460, Springer New York, 2007.

- [166] A. Jalba, M. H. F. Wilkinson, and J. B. T. M. Roerdink, “Cpm: a deformable model for shape recovery and segmentation based on charged particles,” *IEEE Transactions on Pattern Analysis and Machine Intelligence*, vol. 26, no. 10, pp. 1320–1335, 2004.
- [167] B. Li and S. Acton, “Active contour external force using vector field convolution for image segmentation,” *IEEE Transactions on Image Processing*, vol. 16, no. 8, pp. 2096–2106, 2007.
- [168] X. Xie and M. Mirmehdi, “Mac: Magnetostatic active contour model,” *IEEE Transactions on Pattern Analysis and Machine Intelligence*, vol. 30, no. 4, pp. 632–646, 2008.
- [169] X. Xie, “Active contouring based on gradient vector interaction and constrained level set diffusion,” *IEEE Transactions on Image Processing*, vol. 19, no. 1, pp. 154–164, 2010.
- [170] S. Y. Yeo, X. Xie, I. Sazonov, and P. Nithiarasu, “Geometrically induced force interaction for three-dimensional deformable models,” *IEEE Transactions on Image Processing*, vol. 20, no. 5, pp. 1373–1387, 2011.
- [171] I. Kononenko, “Machine learning for medical diagnosis: history, state of the art and perspective,” *Artificial Intelligence in Medicine*, vol. 23, no. 1, pp. 89 – 109, 2001.
- [172] P. De Toledo, P. Rios, A. Ledezma, A. Sanchis, J. Alen, and A. Lagares, “Predicting the outcome of patients with subarachnoid hemorrhage using machine learning techniques,” *Information Technology in Biomedicine, IEEE Transactions on*, vol. 13, no. 5, pp. 794–801, 2009.
- [173] M. Wernick, Y. Yang, J. Brankov, G. Yourganov, and S. Strother, “Machine learning in medical imaging,” *Signal Processing Magazine, IEEE*, vol. 27, no. 4, pp. 25–38, 2010.
- [174] M. Rahman, P. Bhattacharya, and B. Desai, “A framework for medical image retrieval using machine learning and statistical similarity matching techniques with relevance feedback,” *IEEE Transactions on Information Technology in Biomedicine*, vol. 11, no. 1, pp. 58–69, 2007.
- [175] A. Fuller, R. Zawadzki, S. Choi, D. Wiley, J. Werner, and B. Hamann, “Segmentation of three-dimensional retinal image data,” *IEEE Transactions on Visualization and Computer Graphics*, vol. 13, no. 6, pp. 1719–1726, 2007.

- 
- [176] I. Alexandrescu, F. Cheriet, and S. Delorme, "A novel 3d segmentation method of the lumen from intravascular ultrasound images," in *Image Analysis and Recognition* (M. Kamel and A. Campilho, eds.), vol. 4633 of *Lecture Notes in Computer Science*, pp. 949–960, Springer Berlin Heidelberg, 2007.
- [177] E. Filho, M. Yoshizawa, A. Tanaka, O. Saijo, T. Iwamoto, T. Yambe, and S. Nitta, "An adaptive fuzzy segmentation of intravascular ultrasound images," in *Biomedical Imaging: Nano to Macro, 2004. IEEE International Symposium on*, pp. 1311–1314 Vol. 2, 2004.
- [178] C. Cortes and V. Vapnik, "Support-vector networks," *Machine Learning*, vol. 20, no. 3, pp. 273–297, 1995.
- [179] N. Cristianini and J. Shawe-Taylor, *An Introduction to Support Vector Machines and Other Kernel-based Learning Methods*. New York, NY, USA: Cambridge University Press, 2000.
- [180] C.-W. Hsu and C.-J. Lin, "A comparison of methods for multiclass support vector machines," *Neural Networks, IEEE Transactions on*, vol. 13, no. 2, pp. 415–425, 2002.
- [181] Y. Freund and R. E. Schapire, "Experiments with a New Boosting Algorithm," in *International Conference on Machine Learning*, pp. 148–156, 1996.
- [182] A. Ferreira, "Survey on boosting algorithms for supervised and semi-supervised learning," tech. rep., Instituto de Telecomunicações- Instituto Superior de Engenharia de Lisboa, 2007.
- [183] P. Viola and M. Jones, "Robust real-time face detection," *International Journal of Computer Vision*, vol. 57, no. 2, pp. 137–154, 2004.
- [184] R. Nekovei and Y. Sun, "Back-propagation network and its configuration for blood vessel detection in angiograms," *IEEE Transactions on Neural Networks*, vol. 6, no. 1, pp. 64–72, 1995.
- [185] V. Gupta, A. Kale, and H. Sundar, "A robust and accurate approach to automatic blood vessel detection and segmentation from angiography x-ray images using multistage random forests," vol. 8315, pp. 83152F–83152F–6, 2012.

- [186] B. Kelm *et al.*, “Detection, grading and classification of coronary stenoses in computed tomography angiography,” in *Medical Image Computing and Computer-Assisted Intervention MICCAI 2011* (G. Fichtinger, A. Martel, and T. Peters, eds.), vol. 6893 of *Lecture Notes in Computer Science*, pp. 25–32, Springer Berlin Heidelberg, 2011.
- [187] S. Mittal, Y. Zheng, B. Georgescu, F. Vega-Higuera, S. Zhou, P. Meer, and D. Comaniciu, “Fast automatic detection of calcified coronary lesions in 3d cardiac ct images,” in *Machine Learning in Medical Imaging* (F. Wang, P. Yan, K. Suzuki, and D. Shen, eds.), vol. 6357 of *Lecture Notes in Computer Science*, pp. 1–9, Springer Berlin Heidelberg, 2010.
- [188] Y. Zheng, M. Loziczonek, B. Georgescu, S. K. Zhou, F. Vega-Higuera, and D. Comaniciu, “Machine learning based vesselness measurement for coronary artery segmentation in cardiac ct volumes,” vol. 7962, pp. 79621K–79621K–12, 2011.
- [189] D. Rotger, P. Radeva, E. Fernandez-Nofreras, and J. Mauri, “Blood detection in ivus longitudinal cuts using adaboost with a novel feature stability criterion,” in *CCIA* (C. Angulo and L. Godo, eds.), vol. 163 of *Frontiers in Artificial Intelligence and Applications*, pp. 197–204, IOS Press, 2007.
- [190] E. G. Mendizabal-Ruiz, M. Rivera, and I. A. Kakadiaris, “Segmentation of the luminal border in intravascular ultrasound b-mode images using a probabilistic approach,” *Medical Image Analysis*, vol. 17, no. 6, pp. 649 – 670, 2013.
- [191] G. Ughi, T. Adriaenssens, K. Onsea, P. Kayaert, C. Dubois, P. Sinnaeve, M. Coosemans, W. Desmet, and J. Dhooge, “Automatic segmentation of in-vivo intra-coronary optical coherence tomography images to assess stent strut apposition and coverage,” *The International Journal of Cardiovascular Imaging*, vol. 28, no. 2, pp. 229–241, 2012.
- [192] S. Gurmeric, G. Isguder, S. Carlier, and G. Unal, “A new 3-d automated computational method to evaluate in-stent neointimal hyperplasia in in-vivo intravascular optical coherence tomography pullbacks,” in *Medical Image Computing and Computer-Assisted Intervention MICCAI 2009* (G.-Z. Yang, D. Hawkes, D. Rueckert, A. Noble, and C. Taylor, eds.), vol. 5762 of *Lecture Notes in Computer Science*, pp. 776–785, Springer Berlin Heidelberg, 2009.

- 
- [193] N. Tahara, T. Imaizumi, R. Virmani, and J. Narula, "Clinical feasibility of molecular imaging of plaque inflammation in atherosclerosis," *Journal of Nuclear Medicine*.
- [194] A. Nair, B. D. Kuban, E. M. Tuzcu, P. Schoenhagen, S. E. Nissen, and D. G. Vince, "Coronary plaque classification with intravascular ultrasound radiofrequency data analysis," *Circulation*, vol. 106, no. 17, pp. 2200–2206, 2002.
- [195] A. König and V. Klauss, "Virtual histology," *Heart*, vol. 93, no. 8, pp. 977–982, 2007.
- [196] X. Zhang, C. McKay, and M. Sonka, "Tissue characterization in intravascular ultrasound images," *IEEE Transactions on Medical Imaging*, vol. 17, pp. 889–899, Dec 1998.
- [197] E. Brunenberg, O. Pujol, B. Haar Romeny, and P. Radeva, "Automatic ivus segmentation of atherosclerotic plaque with stop & go snake," in *Medical Image Computing and Computer-Assisted Intervention MICCAI 2006* (R. Larsen, M. Nielsen, and J. Sparring, eds.), vol. 4191 of *Lecture Notes in Computer Science*, pp. 9–16, Springer Berlin Heidelberg, 2006.
- [198] L. Athanasiou, P. S. Karvelis, V. Tsakanikas, K. Naka, L. Michalis, C. Bourantas, and D. Fotiadis, "A novel semiautomated atherosclerotic plaque characterization method using grayscale intravascular ultrasound images: Comparison with virtual histology," *IEEE Transactions on Information Technology in Biomedicine*, vol. 16, pp. 391–400, May 2012.
- [199] V. Giannoglou, D. Stavrakoudis, and J. Theocharis, "Ivus-based characterization of atherosclerotic plaques using feature selection and svm classification," in *IEEE 12th International Conference on Bioinformatics Bioengineering (BIBE)*, pp. 715–720, Nov 2012.
- [200] A. Taki, A. Roodaki, S. K. Setarehdan, S. Avansari, G. Unal, and N. Navab, "An IVUS image-based approach for improvement of coronary plaque characterization," *Computers in Biology and Medicine*, vol. 43, no. 4, pp. 268 – 280, 2013.
- [201] N. E. Green, S.-Y. J. Chen, A. R. Hansgen, J. C. Messenger, B. M. Groves, and J. D. Carroll, "Angiographic views used for percutaneous coronary interventions: A three-dimensional analysis of physician-determined vs. computer-generated views," *Catheterization and Cardiovascular Interventions*, vol. 64, no. 4, pp. 451–459, 2005.

- [202] E. Wellnhofer, A. Wahle, I. Mugaragu, J. Gross, H. Oswald, and E. Fleck, "Validation of an accurate method for three-dimensional reconstruction and quantitative assessment of volumes, lengths and diameters of coronary vascular branches and segments from biplane angiographic projections," *The International Journal of Cardiac Imaging*, vol. 15, no. 5, pp. 339–353, 1999.
- [203] S. Chen and J. Carroll, "3-d reconstruction of coronary arterial tree to optimize angiographic visualization," *IEEE Transactions on Medical Imaging*, vol. 19, no. 4, pp. 318–336, 2000.
- [204] C. Canero, F. Vilarino, J. Mauri, and P. Radeva, "Predictive (un)distortion model and 3-d reconstruction by biplane snakes," *IEEE Transactions on Medical Imaging*, vol. 21, no. 9, pp. 1188–1201, 2002.
- [205] B. Movassaghi, V. Rasche, M. Grass, M. Viergever, and W. Niessen, "A quantitative analysis of 3-d coronary modeling from two or more projection images," *IEEE Transactions on Medical Imaging*, vol. 23, no. 12, pp. 1517–1531, 2004.
- [206] J. Yang, Y. Wang, Y. Liu, S. Tang, and W. Chen, "Novel approach for 3-d reconstruction of coronary arteries from two uncalibrated angiographic images," *IEEE Transactions on Image Processing*, vol. 18, no. 7, pp. 1563–1572, 2009.
- [207] A. Wahle, E. Wellnhofer, I. Mugaragu, H. Saner, H. Oswald, and E. Fleck, "Assessment of diffuse coronary artery disease by quantitative analysis of coronary morphology based upon 3-d reconstruction from biplane angiograms," *IEEE Transactions on Medical Imaging*, vol. 14, no. 2, pp. 230–241, 1995.
- [208] R. Liao, D. Luc, Y. Sun, and K. Kirchberg, "3-d reconstruction of the coronary artery tree from multiple views of a rotational x-ray angiography," *The International Journal of Cardiovascular Imaging*, vol. 26, no. 7, pp. 733–749, 2010.
- [209] P. Radeva, R. Toledo, C. V. L., and J. Villanueva, "3d vessel reconstruction from biplane angiograms using snakes," in *Comput. Cardiol*, pp. 773–776, 1998.
- [210] L. E. Fencil and C. E. Metz, "Propagation and reduction of error in three-dimensional structure determined from biplane views of unknown orientation," *Medical Physics*, vol. 17, no. 6, pp. 951–961, 1990.

- [211] A. Sarwal and A. P. Dhawan, “Three dimensional reconstruction of coronary arteries from two views,” *Computer Methods and Programs in Biomedicine*, vol. 65, no. 1, pp. 25 – 43, 2001.
- [212] S. Zheng, T. Meiyang, and S. Jian, “Sequential reconstruction of vessel skeletons from x-ray coronary angiographic sequences,” *Computerized Medical Imaging and Graphics*, vol. 34, no. 5, pp. 333 – 345, 2010.
- [213] D. Rey, G. Subsol, H. Delingette, and N. Ayache, “Automatic detection and segmentation of evolving processes in 3d medical images: Application to multiple sclerosis,” *Medical Image Analysis*, vol. 6, no. 2, pp. 163 – 179, 2002.
- [214] C. Studholme, V. Cardenas, R. Blumenfeld, N. Schuff, H. Rosen, B. Miller, and M. Weiner, “Deformation tensor morphometry of semantic dementia with quantitative validation,” *NeuroImage*, vol. 21, no. 4, pp. 1387 – 1398, 2004.
- [215] M. Lorenzo-Valdés, G. Sanchez-Ortiz, R. Mohiaddin, and D. Rueckert, “Atlas-based segmentation and tracking of 3d cardiac mr images using non-rigid registration,” in *Medical Image Computing and Computer-Assisted Intervention MICCAI 2002* (T. Dohi and R. Kikinis, eds.), vol. 2488 of *Lecture Notes in Computer Science*, pp. 642–650, Springer Berlin Heidelberg, 2002.
- [216] E. M. van Rikxoort, I. Isgum, Y. Arzhaeva, M. Staring, S. Klein, M. A. Viergever, J. P. Pluim, and B. van Ginneken, “Adaptive local multi-atlas segmentation: Application to the heart and the caudate nucleus,” *Medical Image Analysis*, vol. 14, no. 1, pp. 39 – 49, 2010.
- [217] M. Cabezas, A. Oliver, X. Llad, J. Freixenet, and M. B. Cuadra, “A review of atlas-based segmentation for magnetic resonance brain images,” *Computer Methods and Programs in Biomedicine*, vol. 104, no. 3, pp. e158 – e177, 2011.
- [218] T. Makela, P. Clarysse, O. Sipila, N. Pauna, Q. C. Pham, T. Katila, and I. Magnin, “A review of cardiac image registration methods,” *IEEE Transactions on Medical Imaging*, vol. 21, no. 9, pp. 1011–1021, 2002.
- [219] M. Ferrant, A. Nabavi, B. Macq, F. Jolesz, R. Kikinis, and S. Warfield, “Registration of 3-d intraoperative mr images of the brain using a finite-element biomechanical model,” *IEEE Transactions on Medical Imaging*, vol. 20, no. 12, pp. 1384–1397, 2001.

- [220] J. Maintz and M. A. Viergever, “A survey of medical image registration,” *Medical Image Analysis*, vol. 2, no. 1, pp. 1 – 36, 1998.
- [221] B. Zitová and J. Flusser, “Image registration methods: a survey,” *Image and Vision Computing*, vol. 21, no. 11, pp. 977 – 1000, 2003.
- [222] M. Holden, “A review of geometric transformations for nonrigid body registration,” *IEEE Transactions on Medical Imaging*, vol. 27, pp. 111–128, Jan 2008.
- [223] D. Rueckert and J. Schnabel, “Medical image registration,” in *Biomedical Image Processing* (T. M. Deserno, ed.), Biological and Medical Physics, Biomedical Engineering, pp. 131–154, Springer Berlin Heidelberg, 2011.
- [224] H.-M. Chan and A. Chung, “Efficient 3d-3d vascular registration based on multiple orthogonal 2d projections,” in *Biomedical Image Registration* (J. Gee, J. Maintz, and M. Vannier, eds.), vol. 2717 of *Lecture Notes in Computer Science*, pp. 301–310, Springer Berlin Heidelberg, 2003.
- [225] W. R. Crum, T. Hartkens, and D. L. G. Hill, “Non-rigid image registration: theory and practice,” *British Journal of Radiology*.
- [226] T. W. Sederberg and S. R. Parry, “Free-form deformation of solid geometric models,” *SIGGRAPH Comput. Graph.*, vol. 20, no. 4, pp. 151–160, 1986.
- [227] G. E. Christensen, R. D. Rabbitt, and M. I. Miller, “3d brain mapping using a deformable neuroanatomy,” *Physics in Medicine and Biology*, vol. 39, no. 3, p. 609, 1994.
- [228] G. Christensen, S. Joshi, and M. Miller, “Volumetric transformation of brain anatomy,” *IEEE Transactions on Medical Imaging*, vol. 16, pp. 864–877, Dec 1997.
- [229] M. Bro-Nielsen and C. Gramkow, “Fast fluid registration of medical images,” in *Visualization in Biomedical Computing* (K. Hhne and R. Kikinis, eds.), vol. 1131 of *Lecture Notes in Computer Science*, pp. 265–276, Springer Berlin Heidelberg, 1996.
- [230] J.-P. Thirion, “Image matching as a diffusion process: an analogy with maxwell’s demons,” *Medical Image Analysis*, vol. 2, no. 3, pp. 243 – 260, 1998.
- [231] A. Savi, M. Gilardi, G. Rizzo, M. Pepi, C. Landoni, C. Rossetti, G. Lucignani, A. Bartorelli, and F. Fazio, “Spatial registration of echocardiographic and positron emission

- tomographic heart studies,” *European Journal of Nuclear Medicine*, vol. 22, no. 3, pp. 243–247, 1995.
- [232] K. Arun, T. S. Huang, and S. D. Blostein, “Least-squares fitting of two 3-d point sets,” *IEEE Transactions on Pattern Analysis and Machine Intelligence*, no. 5, pp. 698–700, 1987.
- [233] P. Besl and N. D. McKay, “A method for registration of 3-D shapes,” *IEEE Transactions on Pattern Analysis and Machine Intelligence*, vol. 14, no. 2, pp. 239–256, 1992.
- [234] S. Klein, M. Staring, and J. P. W. Pluim, “Evaluation of optimization methods for non-rigid medical image registration using mutual information and b-splines,” *IEEE Transactions on Image Processing*, vol. 16, pp. 2879–2890, Dec 2007.
- [235] P. Thevenaz, U. E. Ruttimann, and M. Unser, “Iterative multi-scale registration without landmarks,” in *International Conference on Image Processing*, vol. 3, pp. 228–231 vol.3, Oct 1995.
- [236] C.-C. Ko, C.-W. Mao, and Y.-N. Sun, “Multiresolution registration of coronary artery image sequences,” *International Journal of Medical Informatics*, vol. 44, no. 2, pp. 93 – 104, 1997.
- [237] E. Meijering, W. Niessen, and M. Viergever, “Retrospective motion correction in digital subtraction angiography: a review,” *IEEE Transactions on Medical Imaging*, vol. 18, no. 1, pp. 2–21, 1999.
- [238] Y. Bentoutou, N. Taleb, M. C. E. Mezouar, M. Taleb, and L. Jetto, “An invariant approach for image registration in digital subtraction angiography,” *Pattern Recognition*, vol. 35, no. 12, pp. 2853 – 2865, 2002.
- [239] J. Yang, Y. Wang, S. Tang, S. Zhou, Y. Liu, and W. Chen, “Multiresolution elastic registration of x-ray angiography images using thin-plate spline,” *IEEE Transactions on Nuclear Science*, vol. 54, no. 1, pp. 152–166, 2007.
- [240] J. Amores and P. Radeva, “Registration and retrieval of highly elastic bodies using contextual information,” *Pattern Recogn. Lett.*, vol. 26, no. 11, pp. 1720–1731, 2005.
- [241] A. Hernández, P. Radeva, A. Tovar, and D. Gil, “Vessel structures alignment by spectral analysis of ivus sequences,” in *Proc. of CVII, MICCAI Workshop*, 2006.

- [242] G. Mariani, L. Bruselli, T. Kuwert, E. Kim, A. Flotats, O. Israel, M. Dondi, and N. Watanabe, "A review on the clinical uses of SPECT/CT," *European Journal of Nuclear Medicine and Molecular Imaging*, vol. 37, no. 10, pp. 1959–1985, 2010.
- [243] P. A. Kaufmann and M. F. D. Carli, "Hybrid SPECT/CT and PET/CT imaging: The next step in noninvasive cardiac imaging," *Seminars in Nuclear Medicine*, vol. 39, no. 5, pp. 341 – 347, 2009. Hybrid Imaging Anniversary Issue (Part II).
- [244] S. Rispler *et al.*, "Integrated single-photon emission computed tomography and computed tomography coronary angiography for the assessment of hemodynamically significant coronary artery lesions," *Journal of the American College of Cardiology*, vol. 49, no. 10, pp. 1059 – 1067, 2007.
- [245] M. Laban, J. A. Oomen, C. J. Slager, J. J. Wentzel, R. Krams, J. C. H. Schuurbiens, A. den Beer, C. Von Birgelen, P. Serruys, and P. J. De Feijter, "Angus: a new approach to three-dimensional reconstruction of coronary vessels by combined use of angiography and intravascular ultrasound," in *Computers in Cardiology 1995*, pp. 325–328, Sept 1995.
- [246] R. Shekhar, R. Cothren, D. Vince, and J. Cornhill, "Fusion of intravascular ultrasound and biplane angiography for three-dimensional reconstruction of coronary arteries," in *Computers in Cardiology, 1996*, pp. 5–8, Sept 1996.
- [247] C. Pellot, I. Bloch, A. Herment, and F. Sureda, "An attempt to 3d reconstruct vessel morphology from x-ray projections and intravascular ultrasounds modeling and fusion," *Computerized Medical Imaging and Graphics*, vol. 20, no. 3, pp. 141 – 151, 1996.
- [248] R. Cothren, R. Shekhar, E. Tuzcu, S. Nissen, J. Cornhill, and D. Vince, "Three-dimensional reconstruction of the coronary artery wall by image fusion of intravascular ultrasound and bi-plane angiography," *The International Journal of Cardiac Imaging*, vol. 16, no. 2, pp. 69–85, 2000.
- [249] C. V. Bourantas, I. C. Kourtis, M. E. Plissiti, D. I. Fotiadis, C. S. Katsouras, M. I. Papafaklis, and L. K. Michalis, "A method for 3d reconstruction of coronary arteries using biplane angiography and intravascular ultrasound images," *Computerized Medical Imaging and Graphics*, vol. 29, no. 8, pp. 597 – 606, 2005.

- [250] P. Wang, O. Ecabert, T. Chen, M. Wels, J. Rieber, M. Ostermeier, and D. Comaniciu, "Image-based co-registration of angiography and intravascular ultrasound images," *Medical Imaging, IEEE Transactions on*, vol. 32, pp. 2238–2249, Dec 2013.
- [251] S. Tu, N. Holm, G. Koning, Z. Huang, and J. Reiber, "Fusion of 3D QCA and IVUS/OCT," *The International Journal of Cardiovascular Imaging*, vol. 27, no. 2, pp. 197–207, 2011.
- [252] C. V. Bourantas, M. I. Papafaklis, K. K. Naka, V. D. Tsakanikas, D. N. Lysitsas, F. M. Alamgir, D. I. Fotiadis, and L. K. Michalis, "Fusion of optical coherence tomography and coronary angiography in vivo assessment of shear stress in plaque rupture," *International Journal of Cardiology*, vol. 155, no. 2, pp. e24 – e26, 2012.
- [253] G. Unal, S. Lankton, S. Carlier, G. Slabaugh, and Y. Chen, "Fusion of ivus and oct through semi-automatic registration," in *MICCAI CVII*, 2006.
- [254] O. Pauly, G. Unal, G. Slabaugh, S. Carlier, and T. Fang, "Semi-automatic matching of oct and ivus images for image fusion," vol. 6914, pp. 69142N–69142N–11, 2008.
- [255] A. Giessen *et al.*, "3d fusion of intravascular ultrasound and coronary computed tomography for in-vivo wall shear stress analysis: a feasibility study," *The International Journal of Cardiovascular Imaging*, vol. 26, no. 7, pp. 781–796, 2010.
- [256] Z. Qian, G. Vazquez, and S. Voros, "Intermodal registration of cta and ivus-vh, and its application on cta-based plaque composition analysis," in *Biomedical Imaging: From Nano to Macro, 2011 IEEE International Symposium on*, pp. 419–423, March 2011.
- [257] M. J. Boogers *et al.*, "Automated quantification of coronary plaque with computed tomography: comparison with intravascular ultrasound using a dedicated registration algorithm for fusion-based quantification," *European Heart Journal*, vol. 33, no. 8, pp. 1007–1016, 2012.
- [258] J.-W. Son, Q. Zhang, and Y. Choi, "Reconstruction of blood vessel model with adventitia from ct and ivus images for fsi analysis," *International Journal of Precision Engineering and Manufacturing*, vol. 14, no. 4, pp. 643–648, 2013.
- [259] R. L. D. Valois, D. G. Albrecht, and L. G. Thorell, "Spatial frequency selectivity of cells in macaque visual cortex," *Vision Research*, vol. 22, no. 5, pp. 545 – 559, 1982.

- [260] J. G. Daugman, "Uncertainty relation for resolution in space, spatial frequency, and orientation optimized by two-dimensional visual cortical filters," *J. Opt. Soc. Am. A*, vol. 2, pp. 1160–1169, Jul 1985.
- [261] D. Fields, "Relations between the statistics of natural images and the response properties of cortical cells," *Optical Society of America*, vol. 4, no. 12, pp. 2379–2394, 1987.
- [262] M. Mulet-Parada and A. Noble, "2D + T acoustic boundary detection in echocardiography," *Medical image analysis*, vol. 4, no. 1, pp. 21–30, 2000.
- [263] P. Kovesi, "Symmetry and asymmetry from local phase," in *Tenth Australian Joint Conference on Artificial Intelligence*, pp. 185–190, 1997.
- [264] L. Spreeuwens and M. Breeuwer, "Detection of left ventricular epi- and endocardial borders using coupled active contours," in *Computer Assisted Radiology and Surgery*, pp. 1147–1152, 2003.
- [265] D. MacDonald, N. Kabani, D. Avis, and A. Evans, "Automated 3-D extraction of inner and outer surfaces of cerebral cortex from MRI," in *NeuroImage*, vol. 12, pp. 340–356, 2000.
- [266] D. Freedman and T. Zhang, "Interactive graph cut based segmentation with shape priors," in *IEEE Conference on Computer Vision Pattern Recognition*, pp. 755–762, 2005.
- [267] J. Malcolm, Y. Rathi, and A. Tannenbaum, "Graph cut segmentation with nonlinear shape priors," in *IEEE Conference on Image Processing*, pp. 365–368, 2007.
- [268] N. Vu and B. S. Manjunath, "Shape prior segmentation of multiple objects with graph cuts," in *IEEE Conference on Computer Vision Pattern Recognition*, pp. 1–8, 2008.
- [269] E. Filho, Y. Saijo, A. Tanaka, and M. Yoshizawa, "Detection and quantification of calcifications in intravascular ultrasound images by automatic thresholding," *Ultrasound in Medicine and Biology*, vol. 34, no. 1, pp. 160–165, 2008.
- [270] C. Xu, J. M. Schmitt, T. Akasaka, T. Kubo, and K. Huang, "Automatic detection of stent struts with thick neointimal growth in intravascular optical coherence tomography image sequences," *Phys. Med. Biol.*, vol. 56, no. 20, pp. 6665–6675, 2011.

- 
- [271] T. Kubo, C. Xu, Z. Wang, N. S. van Ditzhuijzen, and H. G. Bezerra, "Plaque and thrombus evaluation by optical coherence tomography," *International Journal of Cardiovascular Imaging*, vol. 27, no. 2, pp. 289–298, 2011.
- [272] D. Rotger, P. Radeva, and N. Bruining, "Automatic detection of bioabsorbable coronary stents in ivus images using a cascade of classifiers," *IEEE Transactions on Information Technology in Biomedicine*, vol. 14, no. 2, pp. 535–537, 2010.
- [273] V. Lempitsky, M. Verhoek, J. Noble, and A. Blake, "Random forest classification for automatic delineation of myocardium in real-time 3d echocardiography," in *Functional Imaging and Modeling of the Heart* (N. Ayache, H. Delingette, and M. Sermesant, eds.), vol. 5528 of *Lecture Notes in Computer Science*, pp. 447–456, 2009.
- [274] A. Bosch, A. Zisserman, and X. Muoz, "Image classification using random forests and ferns," in *IEEE International Conference on Computer Vision*, pp. 1–8, 2007.
- [275] J. Weston and G. BakIr, "Fast binary and multi-output reduced set selection," Tech. Rep. TR-132, MPI, 2004.
- [276] X. Liang, "An effective method of pruning support vector machine classifiers," *IEEE Transactions on Neural Networks*, vol. 21, no. 1, pp. 26–38, 2010.
- [277] L. Breiman, "Random forests," *Machine Learning*, vol. 45, no. 1, pp. 5–32, 2001.
- [278] Q. Song, X. Wu, Y. Liu, M. Garvin, and M. Sonk, "Simultaneous searching of globally optimal interacting surfaces with shape priors," in *IEEE Conference on Computer Vision Pattern Recognition*, pp. 2879–2886, 2010.
- [279] T. Chan and W. Zhu, "Level set based shape prior segmentation," in *IEEE Conference on Computer Vision Pattern Recognition*, vol. 2, pp. 1164–1170 vol. 2, 2005.
- [280] E. Essa, X. Xie, I. Sazonov, P. Nithiarasu, and D. Smith, "Shape prior model for media-adventitia border segmentation in ivus using graph cut," in *Medical Computer Vision. Recognition Techniques and Applications in Medical Imaging* (B. Menze, G. Langs, L. Lu, A. Montillo, Z. Tu, and A. Criminisi, eds.), vol. 7766 of *Lecture Notes in Computer Science*, pp. 114–123, 2013.

- [281] S. Mansor and J. Noble, "Local wall motion classification of stress echocardiography using a hidden markov model approach," in *5th IEEE International Symposium on Biomedical Imaging: From Nano to Macro*, pp. 1295–1298, 2008.
- [282] D. Beymer and K. Konolige, "Real-time tracking of multiple people using continuous detection," in *International Conference on Computer Vision Frame-Rate Workshop*, 1999.
- [283] L. Xie, G. Zhu, Y. Wang, H. Xu, and Z. Zhang, "Real-time vehicles tracking based on kalman filter in a video-based ITS," in *International Conference on Communications, Circuits and Systems*, vol. 2, pp. 883–886, 2005.
- [284] P. Abolmaesumi, M. Sirouspour, and S. Salcudean, "Real-time extraction of carotid artery contours from ultrasound images," in *Proceedings. 13th IEEE Symposium on Computer-Based Medical Systems*, pp. 181–186, 2000.
- [285] J. Cheng, S. Foo, and S.-M. Krishnan, "Watershed-presegmented snake for boundary detection and tracking of left ventricle in echocardiographic images," *IEEE Transactions on Information Technology in Biomedicine*, vol. 10, no. 2, pp. 414–416, 2006.
- [286] C. Snyder, T. Bengtsson, P. Bickel, and J. Anderson, "Obstacles to high-dimensional particle filtering," *Monthly Weather Review*, vol. 136, no. 12, pp. 4629–4640, 2008.
- [287] D. Terzopoulos and R. Szeliski, "Active vision," ch. Tracking with Kalman snakes, pp. 3–20, MIT Press, 1993.
- [288] M. Isard and A. Blake, "Condensationconditional density propagation for visual tracking," *International Journal of Computer Vision*, vol. 29, no. 1, pp. 5–28, 1998.
- [289] N. Paragios and R. Deriche, "Geodesic active contours and level sets for the detection and tracking of moving objects," *IEEE Transactions on Pattern Analysis and Machine Intelligence*, vol. 22, no. 3, pp. 266–280, 2000.
- [290] Y. Rathi, N. Vaswani, A. Tannenbaum, and A. Yezzi, "Particle filtering for geometric active contours with application to tracking moving and deforming objects," in *IEEE Conference on Computer Vision Pattern Recognition*, vol. 2, pp. 2–9, 2005.

- 
- [291] Y. Rathi, N. Vaswani, A. Tannenbaum, and A. Yezzi, "Tracking deforming objects using particle filtering for geometric active contours," *IEEE Transactions on Pattern Analysis and Machine Intelligence*, vol. 29, no. 8, pp. 1470–1475, 2007.
- [292] L. Rabiner, "A tutorial on hidden markov models and selected applications in speech recognition," *Proceedings of the IEEE*, vol. 77, no. 2, pp. 257–286, 1989.
- [293] Y. Chen, Y. Rui, and T. Huang, "JPDAF based HMM for real-time contour tracking," in *IEEE Conference on Computer Vision Pattern Recognition*, vol. 1, pp. I–543–I–550, 2001.
- [294] Y. Chen, Y. Rui, and T. Huang, "Multicue HMM-UKF for real-time contour tracking," *IEEE Transactions on Pattern Analysis and Machine Intelligence*, vol. 28, no. 9, pp. 1525–1529, 2006.
- [295] M. Sargin, A. Altinok, B. Manjunath, and K. Rose, "Variable length open contour tracking using a deformable trellis," *IEEE Transactions on Image Processing*, vol. 20, no. 4, pp. 1023–1035, 2011.
- [296] H. Fei and I. Reid, "Joint bayes filter: A hybrid tracker for non-rigid hand motion recognition," in *Computer Vision - ECCV 2004* (T. Pajdla and J. Matas, eds.), vol. 3023 of *Lecture Notes in Computer Science*, pp. 497–508, 2004.
- [297] K. Toyama and A. Blake, "Probabilistic tracking with exemplars in a metric space," *Int. J. Comput. Vision*, vol. 48, no. 1, pp. 9–19, 2002.
- [298] H. Breit and G. Rigoll, "Improved person tracking using a combined pseudo-2D-HMM and kalman filter approach with automatic background state adaptation," in *International Conference on Image Processing*, vol. 2, pp. 53–56, 2001.
- [299] G. Turk and J. F. O'brien, "Modelling with implicit surfaces that interpolate," *ACM Trans. Graph.*, vol. 21, no. 4, pp. 855–873, 2002.
- [300] Y. Bar-Shalom, X. R. Li, and T. Kirubarajan, *Estimation with Applications to Tracking and Navigation*. Wiley-Interscience, 2001.
- [301] D. Simon, *Optimal State Estimation: Kalman, H Infinity, and Nonlinear Approaches*. Wiley, 2006.

- [302] C. D. Manning and H. Schütze, *Foundations of statistical natural language processing*. MIT Press, 1999.
- [303] Y. Chen, T. Huang, and Y. Rui, “Parametric contour tracking using unscented kalman filter,” in *International Conference on Image Processing*, vol. 3, pp. 613–616 vol.3, 2002.
- [304] A. Saffari, C. Leistner, J. Santner, M. Godec, and H. Bischof, “On-line random forests,” in *IEEE 12th International Conference on Computer Vision Workshops (ICCV Workshops)*, pp. 1393–1400, Sept 2009.
- [305] S. Balocco *et al.*, “Standardized evaluation methodology and reference database for evaluating IVUS image segmentation,” *Computerized Medical Imaging and Graphics*, vol. 38, no. 2, pp. 70 – 90, 2014.